Universidade de São Paulo
Instituto de Astronomia, Geofísica e Ciências Atmosféricas
Departamento de Astronomia

Inaiara Saraceni de Andrade

Tomografia PCA, Cinemática e *Outflow* de Gás no Núcleo da Galáxia NGC 6951

São Paulo
2014

Inaiara Saraceni de Andrade

Tomografia PCA, Cinemática e *Outflow* de Gás no Núcleo da Galáxia NGC 6951

Trabalho de Conclusão de Curso apresentado ao Departamento de Astronomia do Instituto de Astronomia, Geofísica e Ciências Atmosféricas da Universidade de São Paulo como requisito parcial para a obtenção do título de Bacharel em Astronomia.

Orientador: Prof. Dr. João Evangelista Steiner

São Paulo

2014

Dedico este trabalho aos meus pais
Adriano e Maria e à minha
irmã Tainá.

Agradecimentos

Foi uma longa e, não raras vezes, cansativa jornada até aqui, mas sei que nunca estive sozinha. Gostaria de agradecer a todos os que tiveram uma significativa participação nesta minha caminhada.

Primeiramente, agradeço à Deus, por todas as bençãos, graças e providências nos pequenos e nos grandes detalhes.

Agradeço à minha família, em especial meus pais Adriano e Maria e à minha irmã Tainá por todo apoio, todo o sacrifício de me manter em São Paulo, todas as orações e todo amor.

Ao meu orientador Prof. Dr. João Steiner por ter acreditado e investido em mim, pelo tempo dedicado, pelos ensinamentos e pela confiança depositada.

Um agradecimento todo especial ao meu tutor Dr. Tiago Ricci pela super paciência para explicar, corrigir, ajudar e fazer funcionar as coisas.

Agradeço ao meu namorado Tulio pela paciência de aguentar meus desesperos com provas, notas, prazos e por nã reclamar dos finais de semana dedicados aos estudos.

Aos meus super queridos amigos Louise e Jorge que caminharam comigo nesta jornada, me ensinando, ajudando, apoiando e incentivando, rindo e nos desesperando. Sou muito grata pela amizade construida.

Aos amados luquinhas do GOU Paulo Apóstolo, minha família em São Paulo. Obrigada pela acolhida, pelas partilhas e orações. Obrigada pelo 'sim' de cada um que me manteve firme na jornada.

À FAPESP, pelo apoio financeiro, sob o projeto n^o: 2011/20223-9

E ao Departamento de Astronomia do IAG pela acolhida, dedicação e presença constante durante estes anos de graduação.

"*Amai para entendê-las!*

Pois só quem ama pode ter ouvido

Capaz de ouvir e de entender estrelas."

Olavo Bilac

Resumo

Núcleo Ativo de Galáxia é uma região compacta no centro de uma galáxia ativa cuja "atividade" está relacionada a um buraco negro supermassivo em fase de acreção de massa. As galáxias hospedeiras podem ser divididas em vários tipos de acordo com suas características espectrais e fotométricas. O objeto de estudo deste trabalho foi a região nuclear da galáxia ativa NGC 6951, uma SAB(rs)bc, localizada a 24.1 Mpc de distância e que possui um AGN de baixa luminosidade. Estudar AGNs de baixa luminosidade é importante porque podemos estudá-los com boa resolução espacial, além de caracterizar grandezas de natureza estatística fornecendo uma melhor compreensão sobre a galáxia como um todo, pois eles têm importante ação sobre a evolução da galáxia e sua formação estelar por processos ainda não bem entendidos. Os dados utilizados foram obtidos com o IFU-GMOS no telescópio Gemini Norte, publicados por Storchi-Bergmann et al. (2007) e correspondem a três cubos de dados cobrindo a faixa de 5600A – 7000A (óptico) do núcleo da galáxia onde estão localizadas as linhas de [OI], [NII], Hα e [SII]. Também foram utilizadas imagens do HST para comparação. A metodologia empregada – Filtragem espacial e espectral de Butterworth, Deconvolução de Richardson-Lucy, Tomografia PCA, *STARLIGHT* e *pPXF* – foi escolhida de forma a minimizar o ruído e a maximizar o aproveitamento do grande volume de dados contidos em um cubo de dados o que permitiu uma melhor identificação da estrutura e cinemática de dois cones de ionização na região circumnuclear de NGC 6951. Com a Tomografia PCA identificou-se a cinemática dos cones de ionização, onde o cone superior e mais brilhante possui velocidade mais negativa, indicando um *outflow* de gás, que pode ser visto também com o aumento da dispersão de velocidades (FWHM) das linhas Hα + [NII]. Na análise da cinemática das linhas em emissão, pode-se ver que todas as linhas tem uma componente estreita (FWHM $\simeq$ 188 km/s) e uma componente inter-

mediária (FWHM $\simeq$ 436 km/s). A intensidade da componente larga de Hα com FWHM $\simeq$ 2000 km/s é muito fraca, sendo muito próxima da amplitude do ruído de forma que não se acredita haver uma BLR dado que ela não foi detectada pela Tomografia PCA, mostrando que NGC 6951 apresenta um AGN tipo Seyfert 2.

Abstract

Active Galactic Nucleus is a compact region at the center of an active galaxy whose activity is related to a supermassive black hole acreting mass. Host galaxies can be classified in many types according their spectral and photometric characteristics. This work's object of study was the nuclear region of the galaxy NGC 6951, SAB(rs)bc, at a distance of 24.1 Mpc that hold a low luminosity AGN. The study of nearby galaxies with low luminosity AGN is very important because it is possible to study them with high spatial resolution, besides characterizing several statistical characteristics providing a better understanding about the whole galaxy because they have an important action on the galaxy evolution and on its star formation by not well understood processes. The data were obtained with the IFU-GMOS at the Gemini North, published by Storchi-Bergmann et al. (2007), and consists of three data cubes covering the wavelength range 5600A – 7000A (optic) where de [OI], [NII], Hα e [SII] lines are situated. HST imagens were also used for comparison. The applied methodology – spatial and spectral Butterworth Filtering, Richardson-Lucy's deconvolution, PCA Tomography, *STARLIGHT*, and *pPXF* – was choosen to minimize the noise and to maximize the use of huge amounts of data, allowing us a better identification of the structure and kinematics of two ionization cones in the nuclear region os NGC 6951. Wiht PCA Tomography we identify the kinematics of the two ionization cones, where the upper and brighter cone has more negative velocity, indicating a gas outflow that also can be seen with the velocity dispersion increase (FWHM) of the Hα + [NII] lines. Analysing the emission lines kinematics, we can see that all the lines can be separated in a narrow component (FWHM $\simeq$ 188 km/s) and in an intermediate component (FWHM $\simeq$ 436 km/s). The broad component intensity of Hα, with FWHM $\simeq$ 2000 km/s, is too weak, being very close to the noise amplitude in a way that we don't believe there is a real

BLR since its was not detected on PCA Tomography, showing that NGC 6951 harbors a Seyfert 2 nucleus.

Lista de Figuras

Lista de Tabelas

Sumário

Capítulo 1

Introdução

1.1 Núcleos Ativos de Galáxias

Galáxia é o nome que recebe um aglomerado de estrelas, planetas, gás, poeira e matéria escura ligados gravitacionalmente. As galáxias diferem bastante entre si, entretanto conseguimos facilmente observar semelhanças quanto a forma em suas projeções contra o céu possibilitando uma primeira classificação dessas galáxias, como nos apresentou Hubble em seu livro *Realm of the Nebulae* (Hubble (1936)), que é utilizada até hoje. Porém, não é só pela forma que podemos classificar uma galáxia. Existe uma classe de galáxias que possuem uma emissão espectral que não pode ser explicada unicamente por suas estrelas, as chamadas galáxias ativas, nas quais esta "atividade" está relacionada à presença do chamado Núcleo Ativo de Galáxia (*Active Galactic Nucleus* – AGN).

O AGN é uma região compacta no centro de uma galáxia que está associada a um buraco negro supermassivo (daqui em diante chamado de BNS) em fase de acreção de massa, possuindo, assim, luminosidade comparável ou mesmo superior a de toda a galáxia hospedeira. A partir de suas características espectrais e fotométricas, podemos dividi-los em vários tipos, sendo os principais: quasares e QSOs, rádio-galáxias, Seyferts e LINERS.

A classe mais luminosa de AGNs são os quasares e os QSOs (*Quasi-Stellar Objects*). Esses objetos são superluminosos, estão situados a grandes distâncias e apresentam um aspecto estelar não resolvido, daí o nome de 'quase-estelar'. As rádio-galáxias são assim denominadas por sua grande emissão em rádio; embora os quasares também sejam grandes emissores em rádio, nas rádio-galáxias é possível observar a galáxia hospedeira com maior facilidade, sendo ela, em geral, uma gigante elíptica que apresenta jatos de rádio e dois lóbulos opostos. Galáxias de Seyfert são AGNs de mais baixa luminosidade, o que nos per-

mite observar a galáxia hospedeira com facilidade. Morfologicamente, elas se parecem com galáxias espirais comuns – vários estudos mostram que a maior parte das galáxias de Seyfert são espirais (Adams (1977)), mas com um núcleo brilhante que apresenta fortes linhas de emissão originadas de gás altamente ionizado. Estas galáxias podem ser classificadas em duas categorias: as Seyfert 1, que apresentam tanto linhas estreitas quanto linhas largas de emissão; e as Seyfert 2, que apresentam apenas linhas estreitas de emissão. As linhas largas são emitidas em uma região interna chamada de BLR (*Broad Line Region*) ao passo que as linhas estreitas são emitidas em uma região mais externa chamada NLR (*Narrow Line Region*). As galáxias do tipo LINER (*Low Ionization Nuclear Emission-Line Region*) são objetos de baixa luminosidade e que apresentam linhas de mais baixa ionização que a encontrada em quasares e galáxias de Seyfert.

1.2 O Modelo Unificado dos AGNs

Diante dos diversos tipos de AGNs, já brevemente discutidos, e de várias evidências observacionais, o Modelo Unificado propõe que as diferenças encontradas são devidas a uma combinação de diferenças reais, como luminosidade ou emissão em rádio, e de diferenças aparentes, causadas pela posição do observador.

A figura 1.1 esquematiza uma versão do Modelo Unificado no qual um AGN típico é composto por um BNS, disco de acreção, a região de linhas largas (BLR) externa ao disco de acreção, um toróide molecular (não necessariamente com bordas definidas, é mais provável que seja composto por nuvens) rico em poeira que circunda a BLR a cerca de 1 pc do BNS, e pela região de linhas estreitas (NLR), mais para fora e que pode atingir distâncias de centenas de pc.

Por este modelo, vemos que as Seyfert 1 e 2 são, na verdade, manifestações de um mesmo fenômeno: as galáxias Seyfert 1 são observadas através de uma linha de visada que não intercepta o toro de poeira enquanto que as Seyfert 2 são observadas através de uma linha de visada que intercepta o toro.

Além da orientação, há uma diferença real entre os AGNs, que é sua luminosidade, resultante da taxa de acreção. Assim, os LINERs são AGNs que acretam matéria a uma taxa muito mais baixa, e por isto são pouco luminosos, enquanto que os quasares são mais luminosos devido a uma maior taxa de acreção. As galáxias de Seyfert, neste caso, são

casos intermediários entre estes dois extremos.

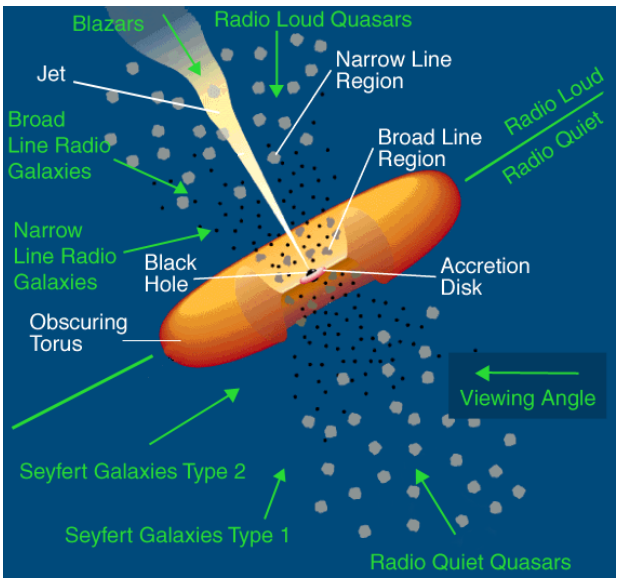

Figura 1.1: Modelo Unificado dos AGNs.

1.3 NGC 6951

A galáxia espiral NGC 6951 foi classificada por de Vaucouleurs et al. (1991) como sendo uma SAB(rs)bc, segundo a classificação de Hubble, uma irmã gêmea da Via Láctea localizada a 24.1 Mpc de distância (Tully e Fisher (1988)) onde 1" corresponde a 96 pc na galáxia.

A atividade nuclear de NGC 6951 já foi classificada anteriormente como LINER (Filippenko e Sargent (1985), Storchi-Bergmann et al. (2007)), intermediária entre LINER e Seyfert (Pérez et al. (2000)) e Seyfert 2 (Ho et al. (1995), Ho et al. (1997)). Esta galáxia possui um BNS em sua região central – localização típica dos BNS presentes na maioria das galáxias de grande massa –, uma barra em larga escala com extensão total de ~ 4 kpc, um anel de formação estelar a aproximadamente 5" do núcleo e um jato em rádio (Saikia et al. (2002)) com P.A. $= 156^o$. O campo IFU foi observado com um P.A. $= 140^o$, compatível com o eixo maior da galáxia que possui P.A. $= 138^o$ segundo Marquez e Moles (1993). O trabalho de Storchi-Bergmann et al. (2007) sobre NGC 6951, suportado por um trabalho anterior do mesmo grupo no caso específico da galáxia LINER/Seyfert 1 NGC 1097 (Fathi et al. (2006)), infere que braços espirais na região do núcleo são canais através

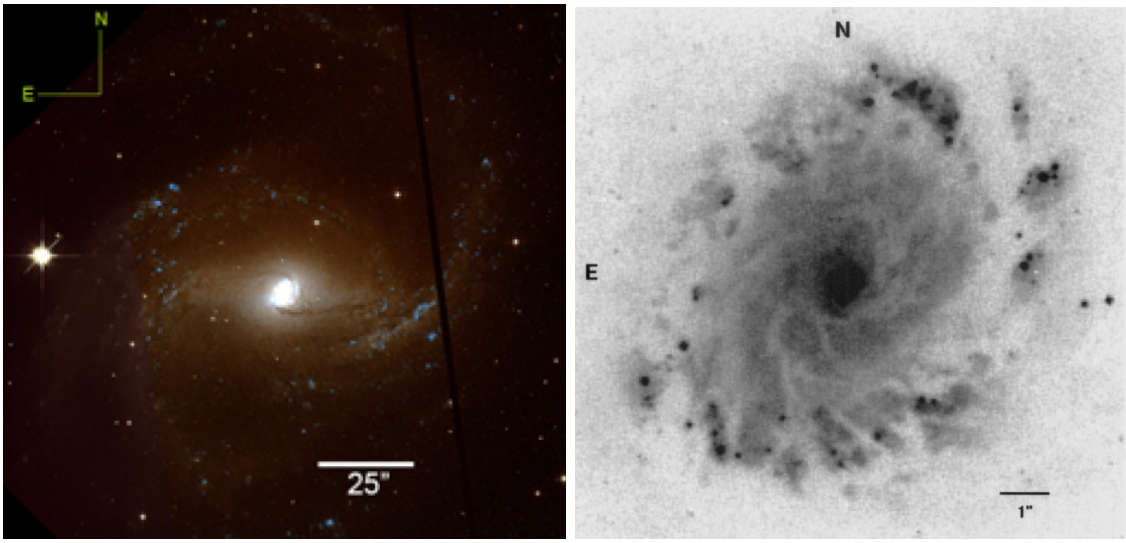

Figura 1.2: À esquerda: imagem de NGC 6951 - SAB(rs)bc pelo HST (D. May et al. - em preparação). À direita: imagem também feita pelo HST onde evidencia-se o anel de formação estelar e a região nuclear de NGC 6951 (Barth et al. (1995)).

dos quais massa é transferida das escalas galácticas para a região nuclear alimentando o BNS central.

NGC 6951 tem se mostrado um bom objeto de estudos detalhados sobre propriedades e mecanismos dos AGNs de mais baixa luminosidade.

1.4 Objetivos

Estudar a região central das galáxias é necessário para se compreender as galáxias como um todo, pois os AGNs têm importante ação sobre a evolução da galáxia e sua formação estelar por processos ainda não bem entendidos. O estudo de galáxias próximas e com núcleos de baixa luminosidade é de grande importância, pois podemos estudá-los com boa resolução espacial, além de caracterizar grandezas de natureza estatística (Ho (2008)).

O objetivo deste trabalho foi estudar a região nuclear da galáxia ativa NGC 6951 através de uma combinação específica de metodologias e remoção de ruídos a fim de melhorar o S/N dos dados e conseguir uma análise detalhada da estrutura – correlações e anticorrelações nos dados – e da cinemática do gás – através dos fluxos e razões de fluxos das linhas de emissão e do campo de velocidades.

Capítulo 2

Observações e Reduções de Dados

Os dados utilizados foram obtidos com o *Integral Field Unit* do *Gemini Multi-Object Spectrograph* (IFU-GMOS) no telescópio Gemini Norte e publicados por Storchi-Bergmann et al. (2007). As observações consistem em três campos IFU de $5'' \times 7''$ cada. Utilizamos apenas o campo central, sendo este composto por três cubos de dados correspondentes às observações de 500 s de exposição cobrindo a faixa de 5600Å – 7000Å (óptico) do núcleo da galáxia onde estão localizadas as linhas de [OI] $\lambda\lambda 6300.3, 6363.7$Å, $H\alpha$ $\lambda 6562.8$Å, [NII] $\lambda\lambda 6548.0, 6583.4$Å e [SII]$\lambda\lambda 6716.4, 6730.8$Å. Também foram utilizadas imagens do *Hubble Space Telescope* da galáxia NGC 6951 obtidas com o filtro F658N e do contínuo em I (HST proposal 9788; L. Ho).

As reduções dos cubos foram feitas utilizando *tasks* do *software* de redução de dados científicos IRAF e rotinas escritas em linguagem IDL desenvolvidas por Tiago Ricci e Roberto Menezes. O processo compreendeu:

– Subtração de *bias*;

– Correção de *flat-field*;

– Montagem dos três cubos de dados;

– Calibração em comprimento de onda;

– Correção de refração atmosférica diferencial;

– Calibração em fluxo e

– Combinação dos três cubos em um único cubo (minimizando ruído proveniente dos raios cósmicos).

Subtração de *bias*: o *bias* é o ruído eletrônico introduzido pelo CCD (*Charge Coupled Device*). Para minimizar seu efeito são feitas algumas exposições de tempo de integração 0 s, em cada observação, e, subtrai-se a média dessas exposições da imagem original. Este

processo foi feito utilizando o IRAF.

Correção de *flat-field*: o ruído introduzido pela diferença de resposta de cada fibra do CCD pode ser corrigido dividindo a imagem original por uma imagem feita ao apontar o telescópio para uma tela ilumidada por uma luz branca homogênea, chamada de imagem de *flat-field*. No caso dos cubos de dados do GMOS, por exemplo, a correção envolve também a obtenção de curvas de resposta a partir do ajuste de um polinômio ao espectro médio do cubo e dividir cada um dos espectros por este polinômio para, assim, se obter a variação pixel a pixel. Este processo também foi feito utilizando o IRAF.

Montagem dos três cubos de dados: um cubo de dados possui informações em três dimensões (x,y,λ), onde x, y correspondem às dimensões espaciais e λ ao comprimento de onda. A montagem dos cubos consiste em organizar os espectros obtidos em cada fibra do CCD na observação, formando, assim, o cubo de dados.

Calibração em comprimento de onda: os espectros obtidos na observação não possuem valores de comprimento de onda, então, a partir de um espectro conhecido, neste caso de uma lâmpada, atribuimos valores de λ conhecidos e aplicamos esta calibração aos espectros observados da galáxia.

Correção de refração atmosférica diferencial: ao atravessar a atmosfera, a luz sofre diferentes refrações para diferentes comprimentos de onda. Nos dados do cubo podemos notar um deslocamento da imagem da galáxias, assim, considerando as diferentes refrações conseguimos corrigir o deslocamento provocado.

Calibração em fluxo: os espectros observados possuem, até o momento, uma relação de contagens em função do comprimento de onda. Utilizando uma estrela de calibração, da qual sabemos a relação contagens $\times$ fluxo, podemos calibrar os espectros observados conseguindo uma relação de fluxo real $\times$ comprimento de onda.

Combinação dos três cubos de dados: Até aqui temos 3 cubos de dados do mesmo campo da galáxia, a região circumnuclear. Combinando-os pela mediana conseguimos a vantagem de minimizar o ruído introduzido pelos raios cósmicos, pois, provavelmente, eles aparecerão em apenas um dos três cubos.

A redução dos dados do HST foi feita utilizando *tasks* do IRAF específicas para imagens do HST.

Capítulo 3

Aspectos Metodológicos

A metodologia utilizada neste trabalho foi escolhida de forma a minimizar o ruído, aumentando, assim, a proporção sinal/ruído (S/N, do inglês *Signal/Noise*) dos dados e maximizar o aproveitamento do grande volume de dados contidos em um cubo de dados.

Como primeiro método de análise, fez-se a filtragem de Butterworth espacial e espectral (Seção 3.1) que consiste na aplicação de um filtro passa-baixa no espaço de frequências de Fourier para a redução dos ruídos de alta frequência espaciais e espectrais. No cubo filtrado, aplicou-se a Tomografia PCA (Seção 3.3) para remover o *fingerprint* instrumental (Seção 3.4) do cubo de dados, em geral caracterizado por estruturas provenientes de uma assinatura de baixa frequência espectral. A remoção foi feita ajustando-se uma função *spline* no Autoespectro 7 que apresentava o *fingerprint*. Para melhorar a nitidez, foi feita a deconvolução de Richardson-Lucy (Seção 3.2) que é um processo iterativo que visa melhorar a *Point Spread Function* (PSF) dos dados do cubo. O resultado da Tomografia PCA foi comparada com o mapa de estruturas (Seção 3.5) da imagem do HST.

Para estudar a cinemática do gás, retirou-se a componente estelar do cubo por meio de uma síntese espectral feita com o auxílio do *software* STARLIGHT (Seção 3.6). A síntese espectral é feita a partir de uma base de espectros (observados ou teóricos) de diferentes populações estelares gerando um cubo de dados estelar. Subtraindo do cubo original, tem-se um cubo de dados do gás cuja principal característica são as linhas de emissão do AGN com um bom S/N. Aplicou-se, então, a Tomografia PCA no cubo de gás. Com o ajuste gaussiano das linhas de emissão do cubo de gás (Seção 3.7) fez-se o estudo da cinemática dessas linhas e, com o *Penalized Pixel Fitting* – pPXF (Seção 3.8), obteve-se os campos de velocidade estelar e do gás.

3.1 Filtragem de Butterworth

Filtros de Butterworth são filtros passa-baixa, isto é, permitem a passagem de baixa frequência cortando as frequências acima de um valor pré-determinado. No tratamento de cubos de dados, essa filtragem pode ser utilizada para a redução dos ruídos de alta frequência espacial e espectral. O cubo de dados é, inicialmente, submetido à filtragem de Butterworth espacial e espectral no espaço de Fourier. Primeiramente é feita a transformada discreta de Fourier em duas dimensões:

$$I(u,v,\lambda) = \frac{1}{MN}\sum_{x=0}^{M-1}\sum_{y=0}^{N-1} I(x,y,\lambda).e^{-2\pi i(uxN/M+vy)} \tag{3.1}$$

para $u = 0, 1, 2, ..., M-1$. Onde (x, y) são as coordenadas espaciais e (u, v) as respectivas coordenadas em frequência. I é a intensidade no pixel (x, y, λ) e I sua transformada no pixel (u, v, λ). O filtro de Butterworth espacial é bidimensional e pode ser expresso como:

$$B(u,v) = \frac{1}{1+\left[\sqrt{\left(\frac{u}{a}\right)^2+\left(\frac{v}{b}\right)^2}\right]^{2n}} \tag{3.2}$$

Onde (a, b) são as frequências de corte nos eixos (u, v), respectivamente. O filtro de Butterworth espectral é o equivalente espacial em uma dimensão que pode ser expresso como:

$$B(u) = \frac{1}{1+\left[\frac{|u|}{a}\right]^{2n}} \tag{3.3}$$

A aplicação dos filtros de Butterworth aos cubos de dados foi feita por rotinas escritas em linguagem IDL desenvolvidas por Tiago V. Ricci.

3.2 Deconvolução de Richardson-Lucy

Em astronomia, o conceito de convolução é bastante importante, pois é sabido que a imagem observada de qualquer objeto astronômico a partir da superfície da Terra corresponde à imagem original desse objeto convoluída com uma *Point Spread Function* (PSF) devida à atmosfera terrestre e, próximo ao limite de difração, ao padrão de interferência introduzido. É essa convolução que faz com que a imagem de um objeto pontual (como

uma estrela, por exemplo) vista a partir da superfície da Terra apresente um diâmetro aparente, que é conhecido como *seeing*. Sendo $O(x, y)$ a imagem original do objeto observado e $P(x, y)$ a PSF da atmosfera terrestre, a imagem observada desse objeto pode ser dada por

$$I(x, y) = \int\int P(x - x_1, y - y_1) \cdot O(x_1, y_1) dx_1 dy_1 + N(x, y) \tag{3.4}$$

ou

$$I(x, y) = (P \otimes O)(x, y) + N(x, y) \tag{3.5}$$

onde $N(x, y)$ é um ruído aditivo introduzido, por exemplo, pelo instrumento de observação.

O procedimento da deconvolução é um processo iterativo que, como o próprio nome sugere, visa reverter o efeito de uma convolução. No caso astronômico, em geral, o problema da deconvolução é colocado da seguinte maneira: conhecendo-se a imagem observada $I(x, y)$ e a PSF, $P(x, y)$, deseja-se obter a imagem original $O(x, y)$, no caso ideal; porém, no caso real, o que se observa é uma melhora na qualidade da imagem, isto é, a PSF torna-se mais "nítida".

$$O^{n+1}(x, y) = \left[\frac{I(x, y)}{P \otimes O^n(x, y)} \otimes P^t(x, y)\right] O^n(x, y) \tag{3.6}$$

Onde O^n é o passo n da imagem e O^{n+1} é o passo $n + 1$. Normalmente fazemos de 6 a iterações, dependendo da confiança que se tem na PSF.

Neste caso, a PSF foi obtida através da largura a meia altura (*Full Width Half Maximum*, FWHM) da linha de [OI]$\sim$ 0,52 e fizemos n = 6 iterações. A deconvolução foi por rotinas escritas em linguagem IDL desenvolvidas por Tiago V. Ricci.

3.3 Tomografia PCA

O cubo de dados foi analisado com a metodologia da Tomografia PCA (*Principal Component Analysis*; Steiner et al. (2009)), que é um método de análise simultânea de imagens e espectros de cubos de dados.

Um cubo de dados obtido com IFU é caracterizado por três dimensões: (x, y, λ) e cada pixel é caracterizado por uma intensidade $Iij\lambda$, onde ij correspondem aos pixels espaciais

e λ ao comprimento de onda. Inicialmente transformamos o cubo em uma matriz $I\beta\lambda$ onde:

$$\beta = \mu(i-1) + j \tag{3.7}$$

Sobre essa matriz $I\beta\lambda$ é aplicada o PCA que é muito eficiente em identificar padrões e correlações nos dados que, de outra forma dificilmente seriam notados. Matematicamente o PCA é definido como uma transformação linear que transforma os dados (correlacionados) em uma novo sistema ortogonal de coordenadas, ordenados de tal forma que o primeiro autovetor explica a maior parte da variância (autovalor), seguido pelo segundo autovetor e assim por diante. A matriz de covariância dos dados originais é dada por:

$$C_{cov} = \frac{I_{\lambda\beta} \cdot [I_{\lambda\beta}]^T}{n-1} \tag{3.8}$$

que tem a propriedade de ser simétrica

$$C_{cov} = [C_{cov}]^T \tag{3.9}$$

A transformada que corresponde ao PCA é:

$$T_{k\beta} = E_{k\lambda} \cdot I_{\lambda\beta} \tag{3.10}$$

Onde $Tk\beta$ são os dados no novo sistema de coordenadas $Ek\lambda$ que são chamados de autovetores ou autoespectros. A transformação é obtida a partir da diagonalização da matriz de covariância. Obtêm-se, então, uma matriz diagonal, na nova base de autvetores:

$$D_{cov} = \frac{T_{k\beta} \cdot [T_{k\beta}]^T}{n-1} \tag{3.11}$$

Sendo que os elementos diagonais dessa matriz são os autovalores. A matriz $Tk\beta$ pode ser obtida de (3.10) que é a projeção dos dados sobre os autovetores; agora os elementos espaciais serão chamados de tomogramas, pois representam recortes dos dados no novo espaço dos autovetores.

A aplicação da Tomografia PCA foi feita por rotinas escritas em linguagem IDL desenvolvidas por Tiago V. Ricci e Roberto Menezes.

3.4 Remoção de *Fingerprint* Instrumental

A Tomografia PCA é um método bastante sensível em detectar sinal e, também, ruído. Em geral, ele detecta ruídos de natureza instrumental de baixa frequência espectral - chamado de *fingerprint* - que pode ser removido com o auxílio da Tomografia PCA.

Para tratar este tipo de ruído, foi necessário criar um cubo de dados apenas com as componentes estelares dos espectros, ou seja, foram removidas todas as linhas de emissão do AGN, as linhas de céu e os *gaps* gerados pela junção dos três CCDs. Foi feito um PCA nesse cubo e ajustou-se uma função *spline* (função de baixa frequência) no autoespectro 7 (E7) que continha o *fingerprint* e dividiu-se o E7 pela função encontrada. O autoespectro resultante foi substituído na reconstrução do cubo de dados, de modo a se eliminar a variância do *fingerprint*. Para remover o *fingerprint* do cubo original, subtraiu-se o cubo estelar com *fingerprint* do novo cubo estelar com o autovetor 7 corrigido resultando em um cubo de *fingerprint*. Por fim, do cubo original foi subtraído o cubo de *fingerprint*.

3.5 Mapa de Estruturas

Mapa de estruturas (Pogge e Martini (2002)) é um método de tratamento de imagens aplicado a imagens do HST que remove a maior parte da distribuição homogênea de luz realçando as estruturas finas na escala da PSF. Regiões escuras são poeira e as regiões claras são regiões de linhas de emissão compactas ou aglomerados de estrelas.

Matematicamente, o mapa de estruturas é obtido por:

$$S = \left[\frac{I}{I \otimes P}\right] \otimes P^t \tag{3.12}$$

onde I é a imagem original, P é o modelo da PSF obtido ao se adotar um modelo de espectro de uma galáxia elíptica e P^t é a transposta do modelo da PSF ($P^t(x, y) = P(-x, -y)$).

3.6 Stellar Syntesis Analysis – STARLIGHT

O *STARLIGHT* (Cid Fernandes et al. (2005)) é um *software* que realiza uma síntese espectral a partir de um conjunto de espectros de base – constituída por espectros de diferentes populações estelares – para ajustar um dado espectro.

O modelo obtido pode ser expresso como:

$$M_\lambda = \sum_{j=1}^{N*} x_j \gamma_{j,\lambda} \cdot 10^{-0.4 A_{V,j}(q_\lambda - q_{\lambda_0})} \tag{3.13}$$

onde x_j corresponde aproximadamente à fração de luz em λ_0 devida à população j e $A_{V,j}$: extinção sofrida pela população estelar j.

Para encontrar o modelo mais adequado para ajustar o espectro observado, o *STARLIGHT* utiliza métodos numéricos buscando determinar o menor valor de χ^2:

$$\chi^2 = \sum_\lambda [(O_\lambda - M_\lambda) w_\lambda]^2 \tag{3.14}$$

onde O_λ é o espectro observado e $w_\lambda = 1/e_\lambda$, sendo que e_λ corresponde aos erros associados ao espectro observado.

Para aplicar a síntese espectral no cubo de dados, foi feita uma correção da extinção galáctica em todos os espectros do cubo utilizando um programa escrito em linguagem IDL e uma correção em relação ao *redshift* (os espectros foram passados para um referencial de repouso).

A partir do resultado obtido foi possível subtrair do cubo de dados o cubo estelar restando o cubo de gás da galáxia NGC 6951.

3.7 Cinemática das Linhas de Emissão

O estudo das linhas de emissão foi feita através de ajustes gaussianos em linguagem R nas linhas de Hα λ6562.8Å, [NII] $\lambda\lambda 6548.0, 6583.4$Å, [OI] $\lambda\lambda 6300.3, 6363.7$Å e [SII] $\lambda\lambda 6716.4, 6730.8$Å do espectro extraído da região do núcleo da galáxia do cubo de gás que fornecem os fluxos, as velocidades e dispersões das linhas. O ajuste considera duas componentes estreitas e, no caso das linhas de Hα e [OI] λ6300.3Å, também uma componente larga.

Mapeando os fluxos das linhas em cada pixel do cubo, foi possível mapear e calcular as razões de linhas [NII]/Hα, [OI]/Hα e [SII]/Hα. Comparou-se os resultados obtidos com o mapa de estruturas da imagem de NGC 6951 no óptico feita pelo HST.

3.8 Penalized Pixel Fitting – pPXF

O estudo da cinemática estelar e do gás através de campos de velocidades foi feito com o *Penalized Pixel Fitting* (Capellari e Emsellem (2004)) que utiliza parametrizações de Gauss-Hermite para uma determinação precisa da distribuição de velocidades ao longo da linha de visada. Para obtermos esta distribuição de velocidades para a galáxia, cria-se um modelo para esse espectro através da convolução de um espectro *template* com uma função representativa da distribuição de velocidades na linha de visada (van der Marel & Franx 1993; Gerhard 1993). Os parâmetros mais adequados para a distribuição são determinados minimizando-se o χ^2, que mede a concordância entre o modelo criado e o espectro observado $G(x)$, ao longo dos N pixeis espectrais considerados no ajuste:

$$\chi^2 = \sum_{n=1}^{N} r_n^2 \tag{3.15}$$

onde

$$r_n = \frac{G_{mod}(x_n) - G(x_n)}{\Delta G(x_n)} \tag{3.16}$$

O processo metodológico do pPXF consiste na aplicação de um termo de penalização na expressão do χ^2, de modo que, em espectros com altas razões S/N, a solução do ajuste mantenha todos os detalhes da expansão de Gauss-Hermite, mas, em espectros com baixas razões S/N, a solução tenda a um formato gaussiano. Um formato genérico para o χ^2 penalizado pode ser dado por:

$$\chi_P^2 = \chi^2 + \alpha P \tag{3.17}$$

onde P é a função de penalização e $\alpha = \lambda^2 \chi^2$.

Aplicando aos cubos estelar e do gás, foi possível a construção dos mapas de velocidade.

Capítulo 4

Resultados

4.1 Tomografia PCA

4.1.1 Remoção de Fingerprint

Após a redução de dados e montagem do cubo de dados (Seção 2), aplicou-se a Tomografia PCA (Seção 3.3). No autoespectro 7 foi possível identificar, claramente, o que chamamos de *fingerprint* instrumental. Ao removê-lo (Seção 3.4), diminuímos sua variância no cubo de dados conseguindo observar efeitos de menor variância ofuscados por ele.

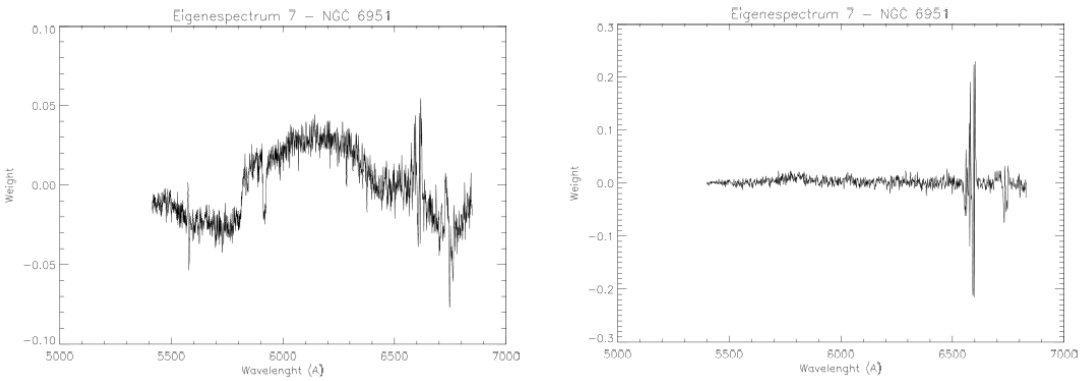

Figura 4.1: À esquerda: Autoespectro 7 resultante da Tomografia PCA que apresenta um ruído de baixa frequência no contínuo chamado de *fingerprint*. À direita: o mesmo autoespectro 7 após a remoção do *fingerprint*.

O tomograma correspondente também é afetado pelo *fingerprint* como mostra a figura 4.2, porém sua identificação é feita através do autoespectro.

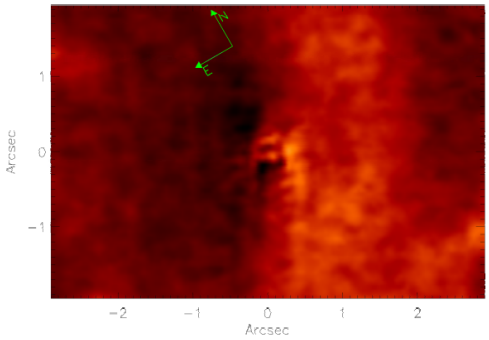

Figura 4.2: Tomograma 7 resultante da Tomografia PCA que apresenta *fingerprint* instrumental.

4.1.2 Cubo Filtrado e Deconvoluído

No cubo de dados sem *fingerprint*, aplicou-se a filtragem de Butterworth espacial e espectral (Seção 3.1) a fim de melhorar o S/N dos dados. Após a filtragem, fez-se a deconvolução dos dados (Seção 3.2) a partir do valor de PSF determinada pela FWHM da imagem da linha de [OI]. O valor encontrado para PSF foi 0,52". Aplicando a Tomografia PCA no cubo filtrado e deconvoluído temos para os 4 primeiros autovalores e autovetores:

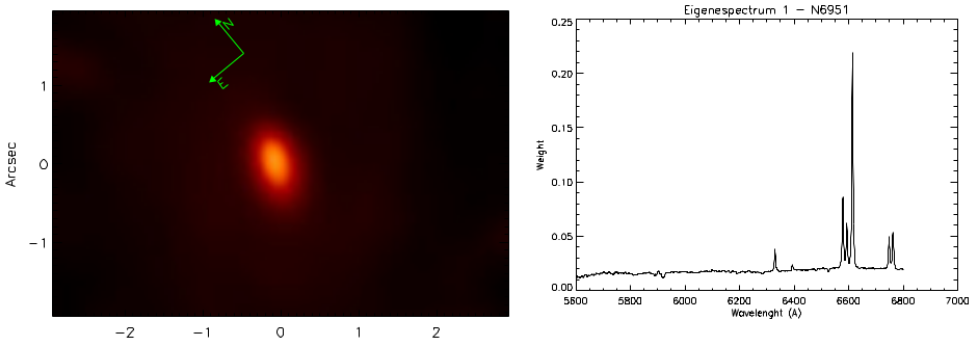

Figura 4.3: Tomograma e Autoespectro 1 resultantes da Tomografia PCA do cubo de dados deconvoluído. O autoespectro corresponde a uma variância de 85,2922%.

O Tomograma 1 e o Autoespectro 1 mostram, como era esperado, as características básicas do espectro e da imagem da galáxia – espectro com linhas de emissão, característico de um AGN, e, no tomograma, luminosidade concentrada no centro ga galáxia – uma vez que a redundância no cubo é muito grande (~85,3%). O Autoespectro 2 mostra duas emissões muito próximas com características espectrais de AGN semelhantes: claras emissões de Hα, [NII] e [SII], anticorrelacionadas com o contínuo azul, indicando onde está a principal emissão nebular e a principal emissão estelar (bojo). O Autoespectro 3 mostra

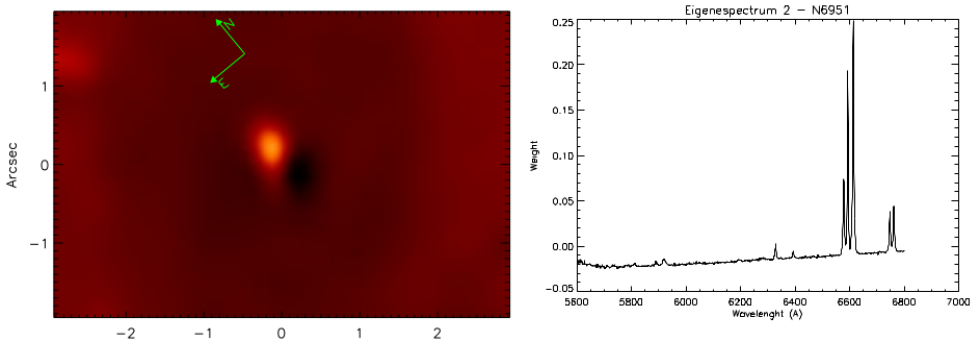

Figura 4.4: Tomograma e Autoespectro 2 resultantes da Tomografia PCA do cubo de dados deconvoluído. O autoespectro corresponde a uma variância de 10,1421%.

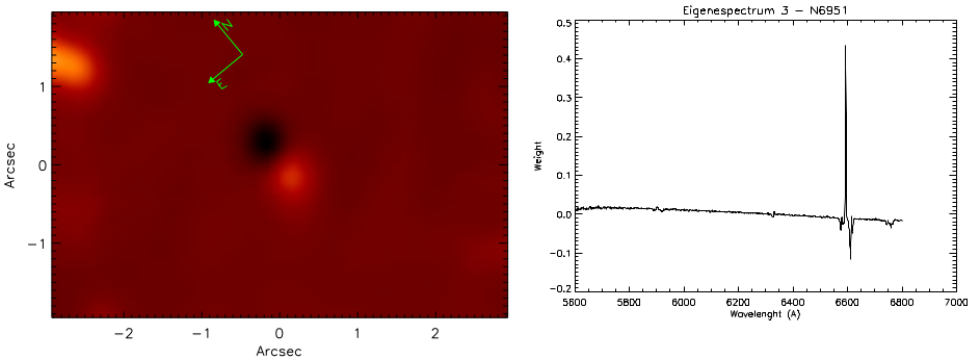

Figura 4.5: Tomograma e Autoespectro 3 resultantes da Tomografia PCA do cubo de dados deconvoluído. O autoespectro corresponde a uma variância de 2.3887%.

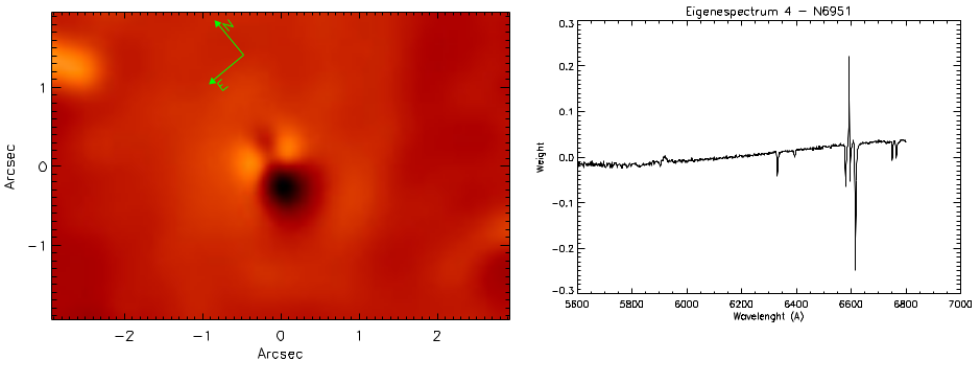

Figura 4.6: Tomograma e Autoespectro 4 resultantes da Tomografia PCA do cubo de dados deconvoluído. O autoespectro corresponde a uma variância de 1,2856%.

a cinemática de duas regiões localizadas acima e abaixo do centro, sendo que a região mais abaixo e mais brilhante tem velocidade mais negativa e a região acima, velocidade mais positiva. O Autoespectro 4 mostra uma anticorrelação entre a emissão de uma região H II e as duas emissões características de AGN.

A análise dos 4 primeiros autovalores se mostra suficiente para os objetivos deste trabalho, pois juntos correspondem a 99,1% da variância total do cubo, como mostra a tabela a seguir.

Tabela 4.1 - Fração das variâncias correspondentes aos autovetores (autoespectros, E) obtidos da Tomografia PCA do cubo de dados deconvoluído de NGC 6951.

Autoespectro	Fração da Variância (%)
E1	85,2922
E2	10,1421
E3	2,3887
E4	1,2856
E1+E2+E3+E4	99,1087

Em uma primeira análise do resultado da Tomografia PCA foi considerada a possível existência de dois AGNs na galáxia, porém levando em conta o Modelo Unificado (1.2) uma possível explicação para o fenômeno visto no Tomograma e Autoespectro 2 seria um cone de ionização. Como ilustrado na Fig. 1.1, uma galáxia que possui um toro ou um disco de poeira ao redor do AGN central, pode gerar um cone de ionização na direção perpendicular ao disco e, um observador cuja linha de visada cruza esse disco veria uma emissão muito fraca ou nem veria o AGN propriamente e observaria os cones de ionização que carregam as características espectrais do AGN ofuscado pelo disco de poeira.

4.1.3 Cubo de Gás

O STARLIGHT (Seção 3.6) é um software que realiza uma síntese espectral a partir de uma base de espectros observados ou teóricos, ou seja, ele gera um espectro que melhor explica o espectro dos dados a partir de um conjunto de espectros de diferentes populações estelares. Utilizamos o STARLIGHT com a base de espectros observados de Bruzual e Charlot (2003) para subtrair do cubo de dados filtrado e deconvoluído a componente estelar e poder analisar separadamente o cubo de gás e o cubo estelar.

O cubo de gás caracteriza o AGN da galáxia, pois, livre da absorção estelar, pode-se fazer uma análise mais completa da emissão do AGN tanto com a Tomografia PCA, como da cinemática das linhas, como será mostrado nas próximas seções.

Aplicando, então, a Tomografia PCA no cubo de gás, obteve-se para os 4 primeiros tomogramas e autoespectros:

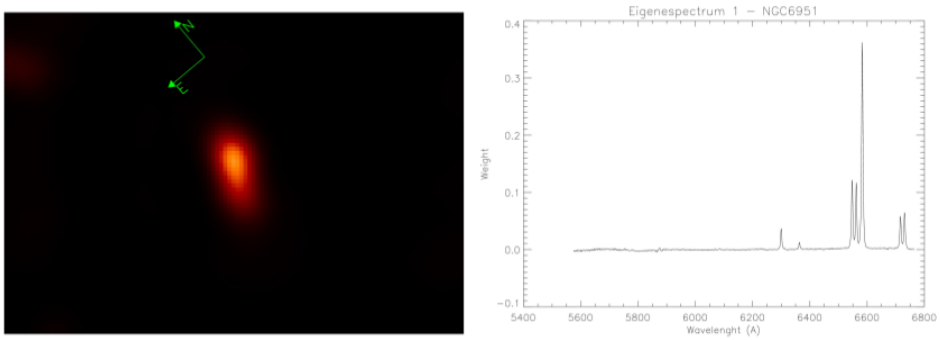

Figura 4.7: Tomograma e Autoespectro 1 resultantes da Tomografia PCA do cubo de dados contendo apenas a componente gasosa, ou seja, sem linhas de absorção. O autoespectro corresponde a uma variância de 88,3926%.

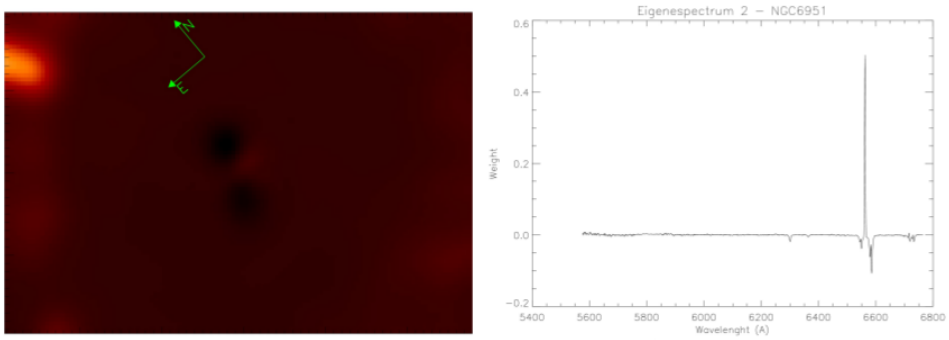

Figura 4.8: Tomograma e Autoespectro 2 resultantes da Tomografia PCA do cubo de dados contendo apenas a componente gasosa. O autoespectro corresponde a uma variância de 7,6478%.

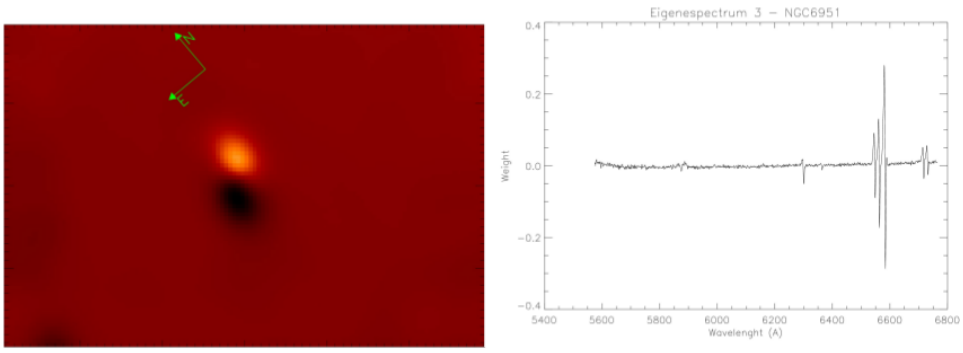

Figura 4.9: Tomograma e Autoespectro 3 resultantes da Tomografia PCA do cubo de dados contendo apenas a componente gasosa. O autoespectro corresponde a uma variância de 2,4502%.

Como era esperado, temos um cubo sem linhas de absorção estelar e com um ótimo S/N, de modo que o Tomograma e Autoespectro 1 mostram o espectro característico de

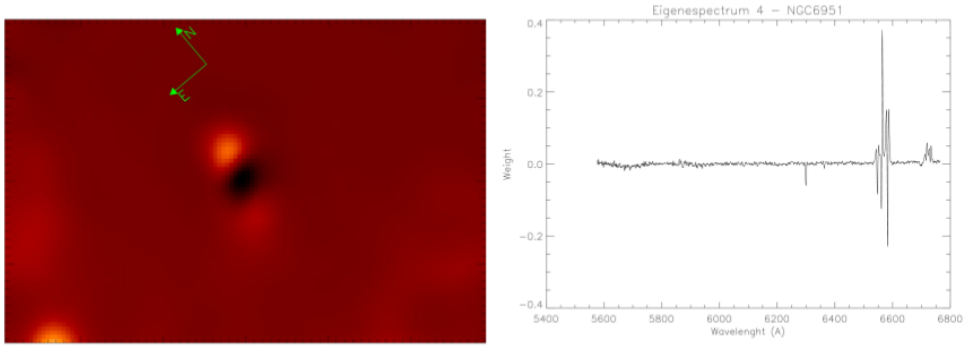

Figura 4.10: Tomograma e Autoespectro 4 resultantes da Tomografia PCA do cubo de dados contendo apenas a componente gasosa. O autoespectro corresponde a uma variância de 0,9941%.

um AGN. O Tomograma e Autoespectro 2 mostra a anticorrelação entre a emissão de Hα e a emissão do AGN. O Tomograma e Autoespectro 3 mostra a cinemática dos cones de ionização, onde o cone superior e mais brilhante possui velocidade mais negativa e o inferior, mais positiva. A orientação dos cones de ionização (PA = 144°) é compatível com a orientação do jato em rádio (PA = 156°). No Tomograma e Autoespectro 4 vemos a anticorrelação entre as velocidades de dispersão das asas largas (BLR) e os perfis estreitos das linhas (NLR). Este resultado é interpretado como efeito da diferença das FWHM das linhas. Nas regiões onde a velocidade de dispersão é maior temos em evidência o local onde o gás é mais turbulento. Tendo que o cone mais brilhante, portanto mais próximo, possui velocidade negativa, esta turbulência pode ser explicada por um *outflow* provocado pela interação do jato em rádio com o disco de poeira ao redor do AGN.

Tabela 4.2 - Fração das variâncias correspondentes aos autovetores (autoespectros, E) obtidos da Tomografia PCA do cubo de gás de NGC 6951, ou seja, sem a componente estelar.

Autoespectro	Fração da Variância (%)
E1	88,3926
E2	7,6478
E3	2,4502
E4	0,9941
E1+E2+E3+E4	99,4848

Os 4 primeiros tomogramas e autoespectros resultantes da Tomografia PCA do cubo de gás possuem juntos uma variância de 99.485% dos dados, as variâncias dos demais autoespectros está representada na Figura **??** na qual apresenta o *Scree Test* que é um

método estatístico pelo qual pode-se quantificar a relevância dos autovetores em uma análise de componentes principais. O ajuste representado mostra, essencialmente, o ruído e os valores acima representam o sinal.

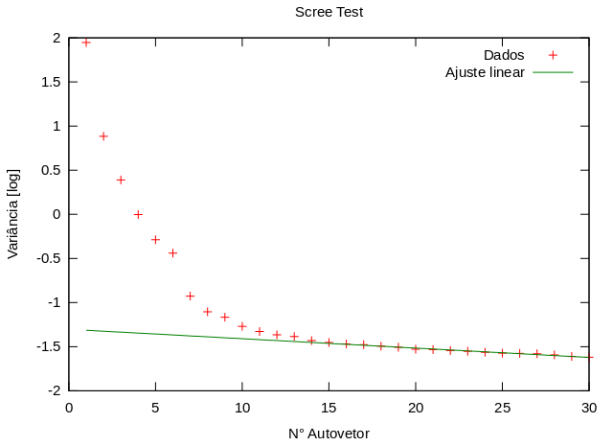

Figura 4.11: Gráfico da variância dos autoespectros resultantes da Tomografia PCA do cubo de gás.

4.2 Intensidades das Linhas (Gemini + HST)

A partir de ajustes gaussianos em cada um dos espectros do cubo de gás, foi possível mapear os fluxos das linhas de emissão. O fluxo de Hα, como esperado, é mais intenso na região nuclear e alongado segundo a orientação dos cones de ionização sendo bem fraco ($< 0.17 \times 10^{-17} erg.s^{-1}.cm^{-2}$) na região entre o núcleo e o anel de formação estelar e volta a aumentar nas proximidades do anel. Há também um pico de emissão em uma região HII conhecida de formação estelar. O fluxo de [NII] $\lambda\lambda 6548.0, 6583.4$ é bastante parecido com o de Hα, mudando a intensidade, com um pico de $\approx 3.6 \times 10^{-17} erg.s^{-1}.cm^{-2}$.

A largura equivalente da linha de Hα possui um pico na região HII contida no anel de formação estelar, valores mais baixos e de mesma amplitude no anel e na região nuclear. Para a linha de [NII] pode-se notar a presença de dois picos, sendo o superior de valor mais alto que o inferior.

O mapa de estruturas (Seção 3.5) – no qual é realçado as estruturas de alta frequência da imagem, permitindo a visualização de estruturas finas – feito a partir da imagem da região do núcleo da galáxia NGC 6951 obtida pelo HST no filtro F658N, revela, também, a presença de duas estruturas e um corpo compacto no centro. As duas estruturas estão

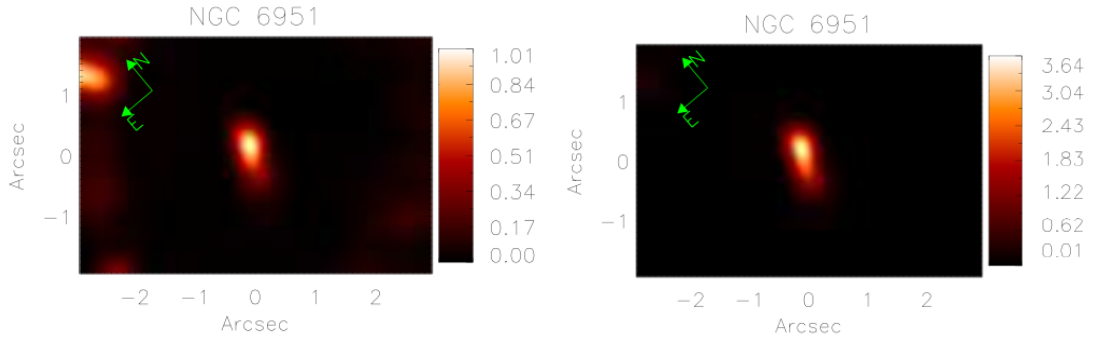

Figura 4.12: Fluxo das linhas de Hα e [NII] em $10^{-17} erg.s^{-1}.cm^{-2}$ na região circumnuclear de NGC 6951.

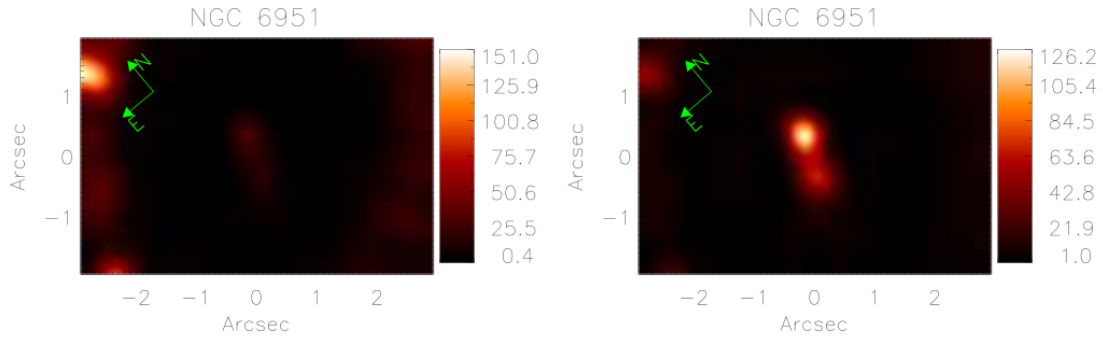

Figura 4.13: Largura equivalente das linhas de Hα e [NII] na região circumnuclear de NGC 6951.

alinhadas com a direção encontrada dos cones de ionização pelo PCA e pela emissão da linha de Hα. Devido à alta resolução do HST, conseguimos ver o objeto compacto no centro, que coincide com o pico de emissão do bojo estelar e, provavelmente, da localização do AGN (figura 4.14).

4.3 Razão [NII]/Hα

A razão do fluxo das linhas [NII]/Hα é apresentada na figura 4.15. A razão [NII]/Hα fornece o grau de ionização do gás. Esperava-se, poranto, um valor maior na região do núcleo da galáxia. O que se observa são duas estruturas com mais alta razão [NII]/Hα e uma baixa razão na região do AGN. A orientação das estruturas encontradas coincide com a orientação dos cones de ionização, e com a orientação do jato em rádio, encontrados pela Tomografia PCA e vistas também no mapa de estruturas da imagem no óptico do HST. A região central, provavelmente, está obscurecida por um disco de gás molecular, como já

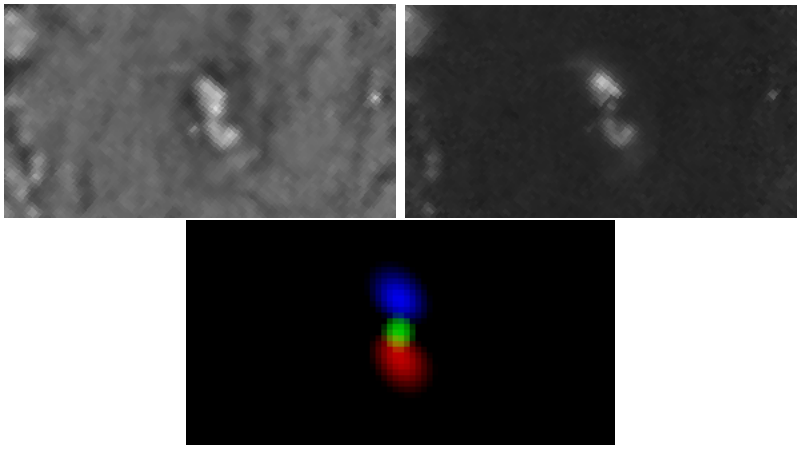

Figura 4.14: À esquerda: Mapa de estruturas da imagem da região do núcleo da galáxia NGC 6951 obtida pelo HST (filtro F658N). À direita: imagem de Hα+[NII]/I. Embaixo: uma composição RGB do Tomograma 3 da Tomografia PCA do cubo deconvoluído a partir dos picos de emissão da linha de Hα (vermelho e azul) e do bojo estelar (verde).

discutido anteriormente. Nota-se uma baixa razão [NII]/Hα na região central, o que pode ser explicado por um excesso de [NII] na direção dos cones de ionização. Esta ionização do [NII] se dá pelo aquecimento devido ao choque gerado pela turbulência nas extremidades dos cones de ionização, gerando uma maior quantidade de [NII] em relação ao Hα.

A FWHM da razão dos fluxos apresentada na Figura 14 é mais alta no cone superior (pico em velocidade de ≈ 195 km/s) que na inferior e há uma falta no núcleo. Este resultado é compatível com encontrado por Storchi-Bergmann, T. et al. 2007.

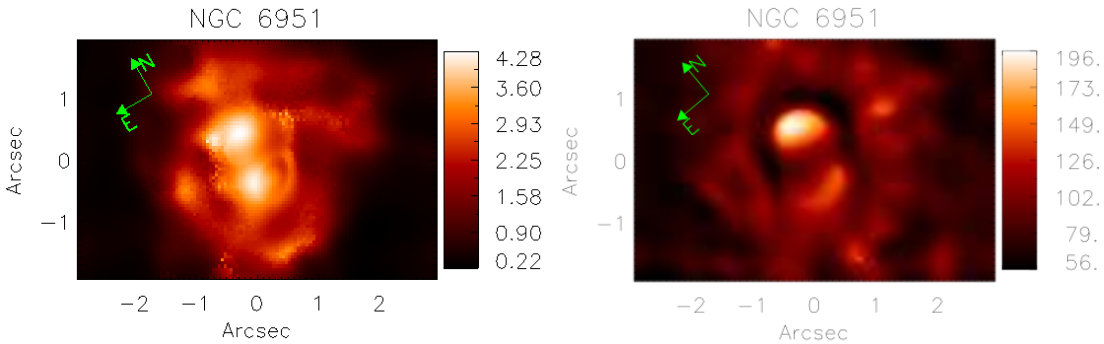

Figura 4.15: À esquerda: Razão dos fluxos das linhas de Hα e [NII] em $10^{-15} erg.s^{-1}.cm^{-2}$ na região circumnuclear de NGC 6951. À direita: Dispersão de velocidades σ da linha de [NII].

4.4 Cinemática das Linhas em Emissão

4.4.1 Decomposição em Gaussianas

A partir do espectro extraído do núcleo do AGN, pode-se fazer ajustes gaussianos nas linhas de emissão Hα λ6562.8Å, [NII] $\lambda\lambda$6548.0, 6583.4Å, [OI] $\lambda\lambda$6300.3, 6363.7Å e [SII] $\lambda\lambda$6716.4, 6730.8Å. A extração do espectro foi feita a partir do cubo de gás, do centroide do AGN e da FWHM - estas últimas calculadas a partir da linha de [OI]. Na Figura 15, são mostrados os ajustes gaussianos feitos, primeiramente, nas linhas de Hα e [NII], em seguida nas demais. Foram ajustadas duas gaussianas em cada linha - componente estreita e intermediária - e, nas linhas de Hα e [OI] também foi ajustada uma terceira componente larga.

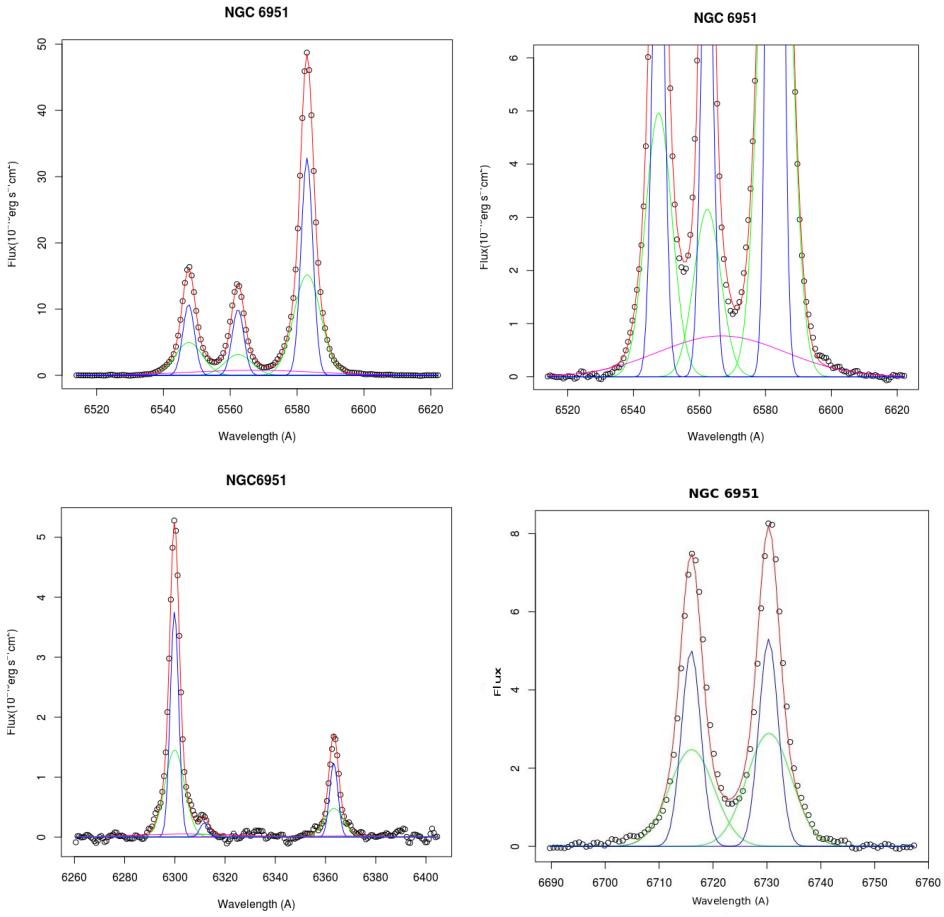

Figura 4.16: A partir de cima à esquerda em sentido horário: Ajustes gaussianos das linhas de Hα e [NII], ampliação do ajuste das linhas de Hα e [NII] mostrando a BLR, [OI] e [SIII] λ6312 e [SII] do espectro extraído da região circumnuclear de NGC 6951. Os fluxos estão em unidades de $10^{-15} erg.s^{-1}.cm^{-2}$

Nota-se que a metodologia utilizada, que busca reduzir ao máximo os ruídos presentes nos dados, possibilitou um ótimo S/N, sendo possível, portanto, o ajuste da linha de [SIII] λ6312.1Å. Também foram ajustadas as componentes largas de Hα e [OI]. Diferentemente da linha de [OI], na qual não encontramos *Broad Line Region* (BLR), o ajuste da linha de Hα mostrou a provável existência de uma fraca BLR ($1 \times 10^{-15} erg.s^{-1}.cm^{-2}$). Sua baixa intensidade pode explicar o fato de não termos detectado anteriormente com a Tomografia PCA.

4.4.2 Largura (FWHM) das Linhas em Emissão

Para as componentes estreitas e intermediárias encontramos velocidades radiais da ordem de -20 km/s e para a componente larga de Hα e [OI] 200 km/s. A largura das linhas encontrada difere em cada uma das componentes. Para a componente estreita encontramos FWHMn = 188(3) km/s, para a componente intermediária FWHMi = 436(8) km/s e para a componente larga FWHMb = 2067(127) km/s. A razão dos fluxos das linhas por Hα foi feita a partir da soma das duas componentes (estreita e intermediária) pela soma das componentes de Hα.

Tabela 4.3 - Ajustes gaussianos das linhas de emissão da região circumnuclear de NGC 6951. O fluxo é dado em $10^{-15} erg.s^{-1}.cm^{-2}$, vel. radial e FWHM em $km.s^{-1}$. n - estreita, i - intermediária e b - larga

Linha	Fluxo	Vel. Radial	FWHM	Fluxo linha/Hα_{n+i}
Hα (n)	32(2)	-20.5(6)	189(2)	-
Hα (i)	44(1)	-20.5(6)	436(8)	-
Hα (b)	37(5)	199(6)	2067(127)	0.48(5)
[NII] (n)	154(6)	-20.5(4)	187(2)	3.92(15)
[NII] (i)	144(3)	-20.5(4)	436(8)	3.92(15)
[OI] (n)	14.2(4)	-20.5(4)	189(2)	0.39(1)
[OI] (i)	15.9(3)	-18(2)	436(8)	0.39(1)
[OI] (b)	2.4(6)	200(5)	2067(127)	0.031(8)
[SIII] (n)	0.45(46)	-20.5(4)	188(3)	0.019(6)
[SIII] (i)	0.98(12)	-18(2)	435(9)	0.019(6)
[SII] (n)	25.8(2)	-20.5(5)	189(2)	0.63(3)
[SII] (i)	22.5(1)	-18(2)	436(8)	0.63(3)

4.4.3 Campos de Velocidades do Gás e Estelar

Por fim, calculou-se o campo de velocidades desta região, tanto do cubo de dados do gás quanto do cubo com a componente estelar. Para o gás, encontramos, o que era esperado: um gradiente de velocidades aproximadamente simétrico e centrado no núcleo da galáxia. As velocidades superiores são negativas (*blueshift*) e as inferiores, positivas (*redshift*). O resultado também está de acordo com o encontrado por Storchi-Bergmann, T. et al. 2007. No cubo estelar, encontramos um campo de velocidades bem homogêneo, mas ruidoso, portanto não foi possível uma análise mais detalhada.

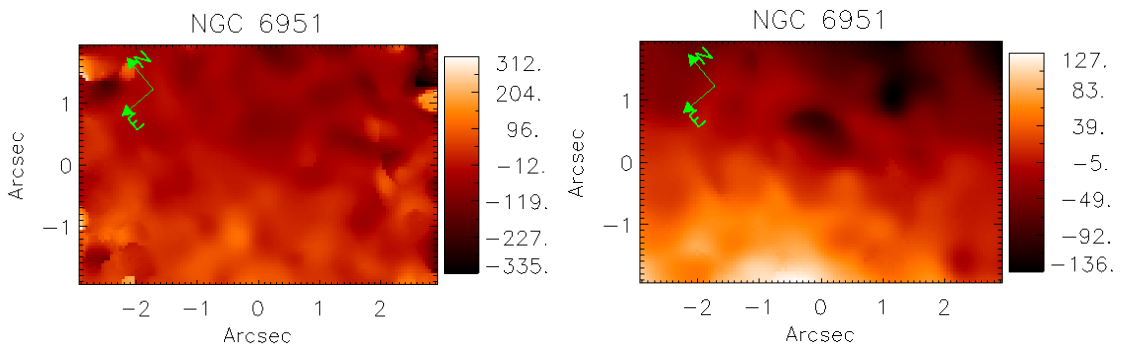

Figura 4.17: À esquerda: Campo de velocidades estelar e À direita: campo de velocidades do gás em $km.s^{-1}$ a partir das linhas de Hα e [NII] na região circumnuclear de NGC 6951.

Capítulo 5

Conclusões

A metodologia utilizada neste trabalho: Filtragem espacial e espectral de Butterworth, Deconvolução de Richardson-Lucy, Tomografia PCA, *STARLIGHT* e *pPXF*, permitiu uma melhor identificação da estrutura e cinemática dos dois cones de ionização na região circumnuclear de NGC 6951.

Com a Tomografia PCA identificou-se a cinemática dos cones de ionização, onde o cone superior e mais brilhante possui velocidade mais negativa, indicando um *outflow* de gás, que pode ser visto também com o aumento da dispersão de velocidades (FWHM) das linhas Hα + [NII]. No núcleo não foi observado uma falta de linhas de emissão, o que era esperado, a hipótese sugerida é a existência de um disco de poeira ao redor do AGN que obscurece o BNS devido a posição da linha de visada. Esta hipótese foi confirmada e aprimorada por D.May et al. - em preparação (segue anexo) em uma posterior observação no infravermelho próximo com o NIFS - Gemini Norte desta mesma galáxia. Essas hipóteses foram suportadas pela análise das imagens do HST, que possuem ótima resolução, e mostram claramente a existência de duas estruturas na região nuclear na mesma orientação dos cones de ionização identificados pela Tomografia PCA, bem como revela um objeto compacto no centro.

Na análise da cinemática das linhas em emissão, fez-se a decomposição dos perfis em componentes gaussianas. Pode-se ver que todas as linhas tem uma componente estreita (FWHM $\simeq$ 188 km/s) e uma componente intermediária (FWHM $\simeq$ 436 km/s). A intensidade da componente larga de Hα com FWHM $\simeq$ 2000 km/s é muito fraca, sendo muito próxima da amplitude do ruído de forma que não se acredita haver uma BLR dado que ela não foi detectada pela Tomografia PCA, uma metodologia que tem se mostrado muito sensível em detectar estas correlações, mostrando que NGC 6951 apresenta um AGN tipo

Seyfert 2; porém considerando-se que não há certeza quanto a presença real ou não da BLR, podemos classificar a galáxia, segundo a notação de Ho (2008), como uma Seyfert 1.9:?. O mapa de velocidade radial do gás indica uma estrutura de velocidade semelhante ao mapa da velocidade das estrelas, não indicando, assim, discrepâncias entre a cinemática do gás e das estrelas. No caso de haver um *inflow* seria esperado um desvio das velocidades do gás, porém, os dados estão no limite do ruído e não sendo possível aceitar ou descartar a possibilidade de *inflow*.

As observações no infravermelho próximo de NGC 6951 mostraram que o *outflow* encontrado está desalinhado e colide com um disco de H_2 molecular (D.May et al. 2014 - em preparação). A figura 5.1 é uma composição entre os dados no óptico (GMOS e HST) e no infravermelho (NIFS) e a linha branca representa P.A. do jato em rádio que é de 156°.

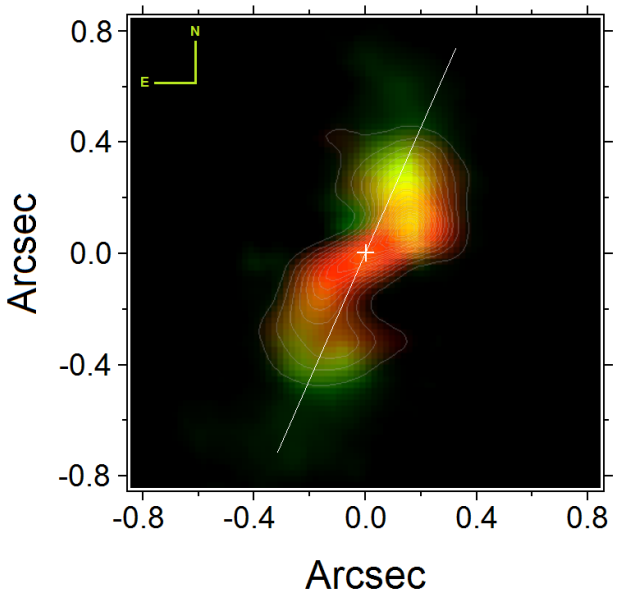

Figura 5.1: Imagem do cubo de gás médio mostrando a emissão de H_2 (vermelho) sobreposto com contornos em escala *square root* e a imagem de Hα + [N II] divida pelo contínuo em I do HST (verde) - D.May et al. 2014 - em preparação.

Referências Bibliográficas

Adams T. F., A Survey of the Seyfert Galaxies Based on Large-Scale Image-Tube Plates, ApJS, 1977, vol. 33, p. 19

Barth A. J., Ho L. C., Filippenko A. V., Sargent W. L., Hubble Space Telescope Observations of Circumnuclear Star-Forming Rings in NGC 1097 and NGC 6951, AJ, 1995, vol. 110, p. 1009

Bruzual G., Charlot S., Stellar population synthesis at the resolution of 2003, MNRAS, 2003, vol. 344, p. 1000

Capellari M., Emsellem E., Parametric Recovery of Line-of-Sight Velocity Distributions from Absortion-Line Spectra of Galaxies via Penalized Likelihood, Publications of the Astronomical Society of the Pacific, 2004, vol. 116, p. 138

Cid Fernandes R., Mateus A., Sodré L., Stasinska G., Gomes J. M., Semi-empirical analysis of Sloan Digital Sky Survey galaxies - I. Spectral synthesis method, Monthly Notices of the Royal Astronomical Society, 2005, vol. 358, p. 363

de Vaucouleurs G., de Vaucouleurs A., Corwin Jr. H. G., Buta R. J., Paturel G., Fouqué P., Third Reference Catalogue of Bright Galaxies. Volume I: Explanations and references. Volume II: Data for galaxies between 0^h and 12^h. Volume III: Data for galaxies between 12^h and 24^h., 1991

Fathi K., Storchi-Bergmann T., Axon D. J., Robinson A., Feeding the Supermassive Black Hole in NGC1097. In American Astronomical Society Meeting Abstracts 207 , vol. 207 of American Astronomical Society Meeting Abstracts, 2006, p. 06.11

Filippenko A. V., Sargent W. L. W., A search for 'dwarf' Seyfert 1 nuclei. I - The initial data and results, ApJS, 1985, vol. 57, p. 503

Ho L. C., Nuclear Activity in Nearby Galaxies, ARA&A, 2008, vol. 46, p. 475

Ho L. C., Filippenko A. V., Sargent W. L., A search for 'dwarf' Seyfert nuclei. 2: an optical spectral atlas of the nuclei of nearby galaxies, ApJS, 1995, vol. 98, p. 477

Ho L. C., Filippenko A. V., Sargent W. L. W., A Search for "Dwarf" Seyfert Nuclei. III. Spectroscopic Parameters and Properties of the Host Galaxies, ApJS, 1997, vol. 112, p. 315

Hubble E. P., Realm of the Nebulae, 1936

Marquez I., Moles M., The stellar content, star formation, and mass of the active galaxy NGC 6951, AJ, 1993, vol. 105, p. 2090

Pérez E., Márquez I., Marrero I., Durret F., González Delgado R. M., Masegosa J., Maza J., Moles M., Circumnuclear structure and kinematics in the active galaxy NGC 6951, A&A, 2000, vol. 353, p. 893

Pogge R. W., Martini P., Hubble Space Telescope Imaging of the Circumnuclear Environments of the CfA Seyfert Galaxies: Nuclear Spirals and Fueling, ApJ, 2002, vol. 569, p. 624

Saikia D. J., Phookun B., Pedlar A., Kohno K., Radio observations of the circumnuclear ring in NGC 6951, A&A, 2002, vol. 383, p. 98

Steiner J. E., Menezes R. B., Ricci T. V., Oliveira A. S., PCA Tomography: how to extract information from data cubes., Monthly Notices of the Royal Astronomical Society, 2009, vol. 395, p. 64

Storchi-Bergmann T., Dors Jr. O. L., Riffel R. A., Fathi K., Axon D. J., Robinson A., Marconi A., Östlin G., Nuclear Spirals as Feeding Channels to the Supermassive Black Hole: The Case of the Galaxy NGC 6951, ApJ, 2007, vol. 670, p. 959

Tully R. B., Fisher J. R., Catalog of Nearby Galaxies, 1988

Anexo

Mon. Not. R. Astron. Soc. **000**, 1–25 (2014) Printed 20 November 2014 (MN LaTeX style file v2.2)

Digging process in NGC 6951: the inclined molecular disc bumped by the outflow

D. May [1⋆], J.E. Steiner[1], T.V. Ricci[1], R.B. Menezes[1], I.S. Andrade[1]
[1] *Instituto de Astronomia Geofísica e Ciências Atmosféricas, Universidade de São Paulo*
Rua do Matão 1226, Cidade Universitária, São Paulo, SP CEP 05508-090, Brazil

Draft for internal use only

ABSTRACT
We present a study of the central 200 pc of the galaxy NGC 6951, SAB(rs)bc - twin of the Milky Way, at a distance of 24 Mpc. The analyzed region comprises the internal part of a starburst ring, located at ∼580 pc from the centre. This galaxy has been classified as a Seyfert 2 and has an inclination i=46°. Its nucleus was observed in the optical with the GMOS, showing an colimmated outflow, and with the HST/ACS, revealing three nuclear components of ionized gas: one central source and two extended structures, suggesting this region could be highly obscured. To probe this region in the NIR, we used the NIFS spectrograph on the Gemini North Telescope. Here we present the detection of a compact structure of molecular gas, seen in H_2, interpreted as a nearly edge-on disc with diameter of ∼47 pc, PA=124° and velocity range from -40 to +40 km s^{-1}. This disc, probably the source of the gas feeding the AGN, has a PA with only 32° of difference with respect to the radio emission which has a PA=156°. The position angle of the radio jet is consistent with that of the ionization cones, with PA=153°±1°, seen in the Hα+[NII] HST image. The Hα+[NII] emission is also seen in the GMOS data cube; the brightest side is seen in blueshift, revealing that the ionized structures are seen in outflow. There are two regions of turbulent gas, seen both in molecular and ionized phases, that are connected to the edges of the molecular disc. These two turbulent spots have a position angle similar to the radio jet and the ionized cones. The line connecting these two turbulent spots coincides with high ratio of [NII]/Hα=5, suggesting that this region is shock exited, partially ionized or both. We explain the structures as a consequence of a //digging process// that the jet inflicts on the disk, ejecting some of the molecular gas and, being exposed to the ionization cones, ionizing it partially. Because of this interaction, the excavated molecular and ionized gas phases are both turbulent. This seems to be the most evident feedback activity in this object. The velocity curve along the molecular disk suggests that the mass within 17 pc is $8.7 \times 10^6 M_\odot$, giving an upper limit to the central black hole mass.

Key words: galaxies – individual (NGC 6951), galaxies – kinematics and dynamics, galaxies – nuclei, techniques – spectroscopic

1 INTRODUCTION

Active Galactic Nuclei (AGNs) comprise some typical components: a supermassive central black hole (SMBH), with a range of mass between 10^{6-10} $M_\odot$; an accretion disk; a dusty and thick torus, responsible for the obscuration in some AGNs, with the internal radius determined by the sublimation radius of the dust, and, not always observable, a radio jet. This jet is, supposedly, launched from the internal parts of the disk, where the highest energy densities are located. The orientation of the jet is given by the structure of the inner accretion disc (McKinney, Tchekhovskoy & Blandford 2013) which, in turn, may not be aligned with the outer observable gas disc, the source of fuel for the AGN (Pringle 2003).

The AGNs can be classified as type 1, where the permitted lines are significantly broader than the forbidden lines, and type 2, where these lines present similar widths. This difference between types 1 and 2 is attributed to the geometrical distribution of the torus with respect to the line of sight (see the Unified Model by Antonucci 1993). According to this model, when the torus is seen edge-on, the Broad

⋆ E-mail: dmay@usp.br

Line Region (BLR) is obscured and only the Narrow Line Region (NLR) is visible. However, intrinsic differences have been found between these two types, as the absence of broad emission lines in the spectra of polarized light of Seyfert 2 galaxies (Gu & Huang 2002). Galaxies with Seyfert nuclei, with higher luminosity, present high ionization spectra, while Low Ionization Nuclear Emission-Line Regions (LINERS) (Heckman 1980), which cannot be easily explained by the unified model, are common among low luminosity AGNs (LLAGNs) (Ho 2008).

There is little doubt about the main points of the Unified Model scheme, but the exact nature of the torus is still matter of discussion. It is extremely difficult to maintain a cold rotating structure in a geometrically thick state. Some processes have been evoked to sustain these observations, as supernova heating (Wada & Norman 2002), outflowing winds (Elitzur & Shlosman 2006) and warped discs (Lawrence 2007). It is important to emphasize that the torus is different from the ~ 30 pc scale distribution of the observable thick discs, which has a small covering factor $\sim 1\%$. It must be closer to the nucleus to account for the required obscuration (Hicks et al. 2009).

The orientation of the narrow line region, defined by the the torus, and the galaxy disk, are essentially uncorrelated (Fischer et al. 2013). The same lack of correlation, seen between the jet and the torus, must tell us something about the dynamics of the innermost region close to the SMBH and about the fueling process itself. The reasons given to explain why this misalignment exists could be due: minor mergers of gas rich dwarf galaxies; the alignment of the jet with the BH spin, which leads to the conclusion that the spins of the central BHs are uncorrelated with the rotation of the circumnuclear discs; or that on scales of 10 pc the turbulent movement of clumps can fuel the AGN in discrete events with randomly oriented orbits. The last option provides a different view of how we can explain the fractions of type 1 and type 2 AGNs in the role of obscuration by inner tilted discs (Lawrence & Elvis 2010), with type 2 AGNs having a larger misalignment.

Within the central hundreds of parsecs of galaxies, most of the gas is in the molecular phase and its morphology and dynamics have been studied mainly through the 2-1 and 1-0 lines of ^{12}CO with resolution $< 1''$, which corresponds to $< 10 - 50$ pc (see the NUGA project by García-Burillo et al. 2003a), and with the H_2 ro-vibrational transitions, that traces the warm gas (T$\approx 700 - 2000$ K), with similar resolution. Close to the nucleus, 90% of the AGNs show H_2 molecular emission (Rodríguez-Ardila et al. 2004) distributed in disc-like structures, and down to a radius < 25 pc the ratio between for the rotational velocity and velocity dispersion $V_{rot}/\sigma = 0.8 \pm 0.3$ (Müller-Sánchez et al. 2013), which means that in this region the gas kinematics is dominated by turbulent motions in a thick disc.

The nuclear morphologies of the gas include lopsided and warped discs, bars, spirals and rings, whose overall asymmetry is responsible for gravitational torques that may drive gas inwards to scales of 100 to 25 pc (Haan et al. 2009). In order to analyze if these structures may influence AGN activity, Erwin et al. (2008) studied the morphology of a sample of 38 S0-Sa galaxies and found that 40% have double bars with the second bar up to 400 pc in length, but no correlation was detected between these galaxies and galaxies with AGNs. They also found that 20% of the sample have internal gas discs with an average radius of 470 pc, and that 29% of the sample have rings, with an average radius of 410 pc and with a higher incidence of discs and rings in Sa galaxies. Previous works show that the presence of nuclear spiral arms are not statistically relevant for active galaxies (Martini et al. 2003), neither for the presence of compact molecular components (García-Burillo et al. 2003a). The results of the NUGA survey (García-Burillo et al. 2003b) show that only one third of the 25 LLAGNs have negative torques, which are an indicative of inflow. This suggests that the interplay between the parsec and hundreds of parsecs scales may be notably different. Since the SMBH feeding process is related to the presence of molecular gas in the nucleus, this could suggest some delay until the accretion takes place or the exhaustion of fuel during the AGN phase.

It happens that it has been very difficult to see evidences of inflowing material into the nucleus (García-Burillo et al. 2005; Costagliola et al. 2013; Storchi-Bergmann 2014). This material, settled as the central gas supply, must come from regions far away from the gravitational influence of the SMBH. How the angular momentum of the gas is lost, is still a matter of discussion. This could be due to gravitational torques, caused by large scale asymmetries, or galaxy-galaxy interactions, which is more efficient than viscosity torques or shocks in the interstellar medium (ISM).

NGC 6951 is a barred spiral galaxy SAB(rs)bc (de Vaucouleurs et al. 1991) (Fig. 1) and hosts a Seyfert 2 AGN (Ho, Filippenko & Sargent 1995, 1997). It is at a distance of 24.1 Mpc (Tully & Fisher 1988) ($1'' = 117$ pc) and has a disc inclination of $i = 46.2°$ (Haan et al. 2009). This galaxy harbours a starburst ring connected to an outer bar, having spiral dust lanes going down to the nucleus with a typical collimated outflow.

Haan et al. (2009) noted the absence of neighbour galaxies within a projected distance of 1 Mpc and redshift differences lower than 500 km s^{-1}, suggesting there was none external gravitational influence for the last $\sim 10^9$ years. These authors also showed that the nucleus of NGC 6951 is HI deficient, implying that its ISM is dominated by the molecular phase. Krips et al. (2007) reported that the nuclear gas of NGC 6951 has similar properties as the Seyfert galaxies NGC 1068 or M51. Both objects have high central HCN-to-CO ratios, suggesting that NGC 6951 could hold the same scenario where the molecular gas chemistry is dominated by X-ray radiation (NGC 1068: Usero et al. 2004; M51: Matsushita et al. 1998).

A radio compact nuclear component was reported with VLA observations by Saikia et al. (2002), with an angular size of $\sim 0''.7 \times \sim 0''.2$, corresponding to $\sim 80 \times 20$ pc^2 in the galaxy, and with a position angle of 156°. The existence of jets in LLAGNs was studied by Mezcua & Prieto (2014), who analyzed sub-arcsec archival data from the VLA and VLBA of eight nearby LLAGNs. They found that all these galaxies have pc-scale or larger radio jets. The non-detection of large-scale jet in this sample of galaxies suggests that the this component is confined to a small region either because of its large misalignment with some internal disc or due to interaction with the ISM.

In this work we will analyze data from the Gemini North Telescope obtained with the Near-Infrared Integral Field Spectrograph (NIFS), in the K band, allowing the study of

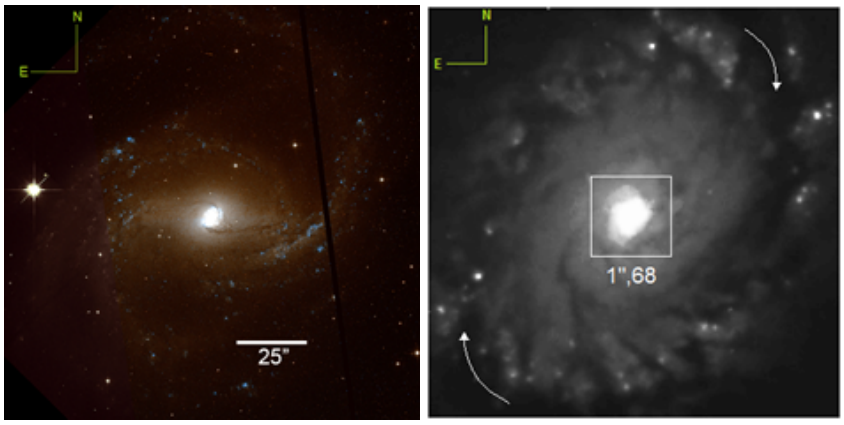

Figure 1. Left: HST image of NGC 6951 in the optical. Right: HST image in the I filter with 9 arcsec^2. The white square denotes the FOV of $1''.68 \times 1''.68$, the same dimensions that will be used in all images in this paper, centred in the bulge (identified by a cross) and with North on top. The arrows show where the large scale bar connects with the stellar ring.

the warm molecular gas through the H_2 lines. This analysis is complemented with data taken with the GMOS spectrograph and with HST images, allowing the study of ionized gas.

The structure of this work is as follows. Sect 2 presents the reduction and treatment of the NIFS and GMOS data cubes. Sect 3 discusses the properties of the emission lines for the molecular gas, its spatial distribution, the kinematics and the estimation of the temperature. Sect 4 presents the same results for the ionized gas. We continue in Sect 5 presenting the stellar content and its kinematics. Then in Sect 6 we discuss the results and finally in Sect 7 we draw our conclusions.

2 OBSERVATIONS, REDUCTIONS AND DATA TREATMENT

2.1 Near infrared data - NIFS

The data presented here were obtained during the night of 2012 September 2, using the adaptive-optics-assisted instrument NIFS on the Gemini North Telescope, under the programme GN-2012B-Q-44. The pixel size of the instrument is $0''.103 \times 0''.043$ in x and y directions, respectively, with a FOV of $\sim 3'' \times 3''$. The observations were taken in the K band ($1.99-2.40$ μm) in 8 individual exposures alternated in on-source and sky observations of 750 s each. However, only 4 of them which presented the lower seeing, of $\sim 0''.35$, were used. The full width at half maximum (FWHM) of one of the lines of the calibration lamp spectra taken in this night is 3Å.

The data were reduced using tasks of the NIFS package in IRAF environment. The procedure included trimming of the images, flat-fielding, sky subtraction, correcting for spatial distortions and wavelength calibration. We performed the removal of telluric bands and the flux calibration using the A0V star HIP 107555. This standard star was chosen because it has a sharper point spread function (PSF) than the other available one, but it introduced a small lack of flux on the blue part of the spectra. Since we are not interested in doing the stellar population synthesis, because of the short wavelength interval of the fit, we simply removed this defect by fitting a spline to the continuum, together with the stellar absorption bands, and subtracting the fit from the original spectra, keeping only the emission lines. At the end of the data reduction process, the IFU data cubes are generated by the task `nifcube`, which re-sampled them to spaxels of $\sim 0''.05 \times 0''.05$. It is important to mention that, after this procedure, the fluxes were not the same as they were in the previous data format (29 slices), and we performed the correction by multiplying the data cubes by a factor of 0.54.

After the reduction, we performed a data treatment procedure, which is described in more detail in Menezes, Steiner & Ricci (2014). We correct the Differential Atmospheric Refraction (DAR) empirically, fitting third degree polynomials through the spatial location of the centroids along the data cube, one for each spatial dimension, in order to maintain them at the same position for each wavelength. Although the DAR is small in the infrared, the high spatial resolution of NIFS observations, with adaptive optics (AO), can account up to 3 spaxels of displacement due this effect. At the end of the correction, all the centroids, measured from the peak in the image of the stellar continuum, remain the same with a precision of $0''.01$. This practical approach is the most precise to remove this effect since the theoretical curves do not reproduce properly the spatial displacements along the spectral axis. This is crucial to combine the data cubes.

The next step consisted of the spatial re-sampling of the data, which improves the visualization of the contours of the structures without changing the spatial resolution. But, when followed by the deconvolution process, leads to better resolutions. The new images, with reduced size of the spaxels and preserved fluxes, are submitted to an interpolation. The new sampling is $0''.021 \times 0''.021$, because it obeys the Nyquist criterion to re-sampling data for the smallest pixel size, corresponding to a half of the sampling-frequency of the image in the y direction. Its worth noticing that this procedure introduces high spatial frequency components, which can be seen in the Fourier transform of the images. These components can be removed by the Butterworth spatial filtering in the frequency domain.

We combined the 4 data cubes, with 4 points of dithering in both spatial dimensions, through a median. It was

necessary to multiply them by a numerical factor because of the flux difference between the observations, in order to apply the median. The median process eliminates the cosmic rays as well as defects in the CCD. The total FOV was cut to comprise only the region inside the stellar ring of 200 pc^2 ($\sim 1''.68 \times 1''.68$) and the final spectral range is from 2.12 to 2.42μm.

2.1.1 Butterworth spatial and spectral filtering

This process consists of a filtering performed in the frequency domain, calculating the Fourier transform of the images or spectra in the data cube. The next step is the multiplication of the Fourier transform by the image corresponding to the Butterwoth filter and the calculation of the inverse Fourier transform of this product. The idea is to remove the high frequencies applying a low-pass filter and return with the new filtered image/spectrum doing the inverse Fourier transform.

In the case of the spatial filtering for the NIFS, the most adequate filter to be applied is the product of a filter with an elliptical shape by one with rectangular shape (see the mathematical definition in Menezes, Steiner & Ricci 2014), and the reason for that is mainly due the asymmetric shape of the pixels on the CCD. The best cut-off frequency found in the case of NGC 6951 was 0.35 Ny for the x axis and 0.4 Ny for the y axis in both filters. There is also an exponential factor n, where the higher the value, more steeper is the cut-off. Here we used n=2. We checked the final data cube, in order to determine how much of the flux of the central region, in a aperture of $\sim 0''.2$, changed after the filtering and we found a variation of 2%, which means that the PSF was practically not affected, if we consider the amount of noise removed from the data.

In a similar way, the filtering can be applied in one dimension, to each spectrum, with just one cut-off frequency. The chosen filtering parameters were f=0.52 Ny and n=6. We verified the flux with the H_2 λ21218 Å emission line for the same aperture and the difference between the filtered and non-filtered fluxes of this line is less than 3 %. Fig. 2 shows that in the filtered spectrum, it is possible to see the He I λ20585 Å line not detected before due to the high level of noise. In the bottom of Fig. 2, we plotted the filtered noise and the correspondent average image. The data cube with spectral filtering was not used to extract the kinematics of the emission lines or CO bands, but only for the Principal Component Analysis (PCA) tomography (Steiner et al. 2009) and for the construction of the He I images.

2.1.2 Richardson-Lucy deconvolution

When one characterize the PSF, in general it can be well described by a Gaussian or a Moffat function. However, for AO corrected images, this approach is not valid anymore because of the complex shape of the PSF. For observations with AO, one expects a PSF with two components: a central diffraction spike, given by the Airy function, and a surrounding halo, given by the Lorentzian function; but with the available spatial resolution, it is not possible to resolve the Airy function and this component is well described by a Gaussian function. Nevertheless, we can not assume such a

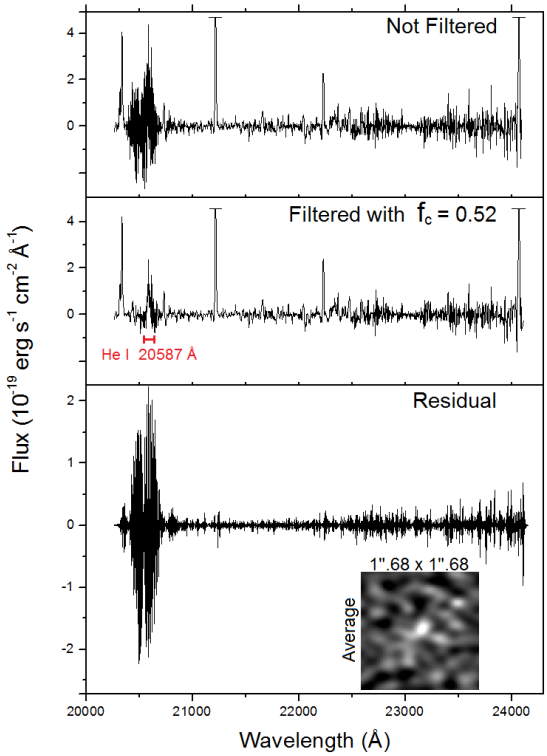

Figure 2. Top: average spectrum with an aperture of $\sim 0''.2$. Middle: filtered spectrum with cut-off frequency of 0.52 Ny, with the detection of the He I line. Bottom: the noise filtered and the average image of the data cube of noise.

simple scenario in the case of NIFS data cubes, because the AO correction introduces complex profiles in the PSF that are not well fitted by any combination of the functions mentioned above. Since there is no observable point-like source in the data cubes of NGC 6951, the alternative solution is to estimate the PSF from the standard star data cube used in the data reduction, taking a small interval over the continuum centred at 2.2 μm. We used only the standard star with the best seeing, of $0''.44$, and therefore no dithering. Because the spaxels in the NIFS are not symmetric, after the reduction process and data treatment we noted the PSF was not symmetric in the FOV, so we opted to symmetrizing the PSF before apply the Richardson-Lucy deconvolution.

One should worn about the possibility that this may or not represent a good approach for the PSF. In any case, a deconvolution may be attempted; an inadequate PSF will not produce gains in the process. Fig. 3 shows the PSF profiles with normalized flux, along the x and y directions. We applied 6 iteractions, 4 less iteractions than we apply when the PSF is extracted from the data, that has proved to be the best choice in this case. Based on the improvement of the FWHM after the AO correction (measured after the reduction and treatment of the standart star) and after the deconvolution (measured as the percentage of FWHM decreased in the continuum), the final spatial resolution is estimated to be $\sim 0''.09$, which corresponds to $\sim$5 pc in the galaxy. In Fig. 4 the spatial structure for the H_2 λ 21218 Å line is shown in 3 different stages of the data treatment, and, at the end of the process, we can clearly see new structures not detected before the data treatment.

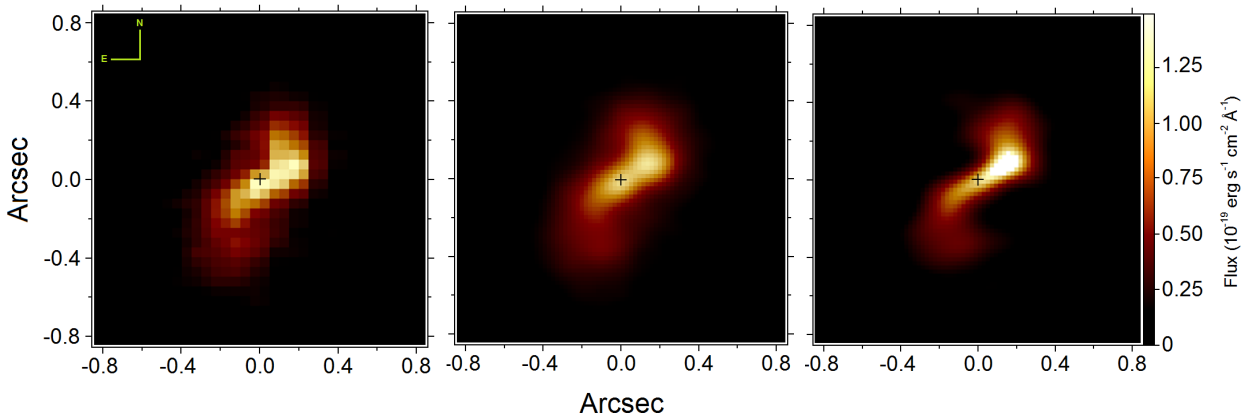

Figure 4. Average images of the molecular gas data cube, with the data cube after the reduction process with pixel scale of 0″.05 (left); after the re-sampling to 0″.021 × 0″.021 and Butterworth filtering (middle); and after the Richardson-Lucy de-convolution process (right).

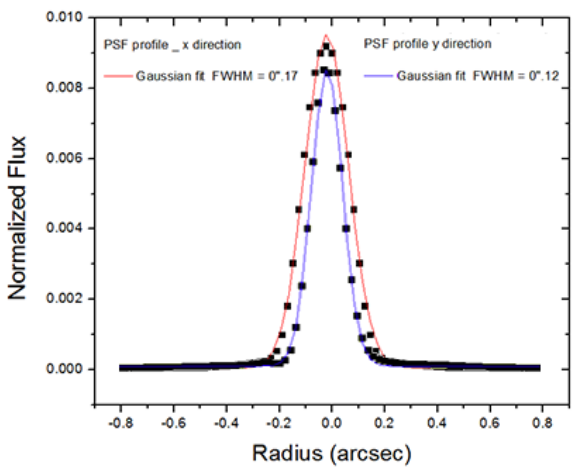

Figure 3. PSF profiles along the x and y directions, with the respective Gaussian fit (red and blue curves).

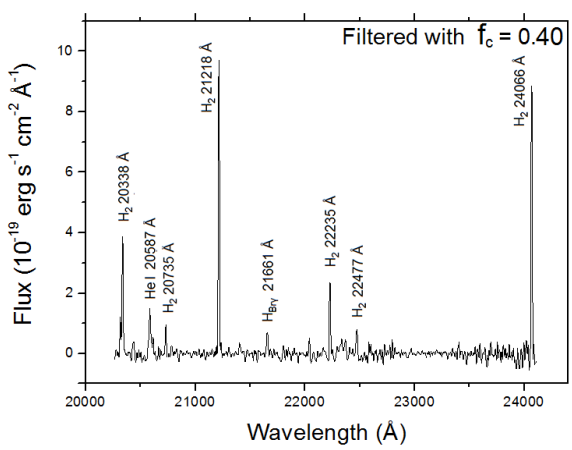

Figure 5. Average spectrum of the data cube of NGC 6951, after the continuum subtraction, within an aperture of 0″.4.

2.2 Optical data - GMOS

The observations obtained with the Integral Field Unit of Gemini Multi-Object Spectrograph (GMOS IFU) on the Gemini North telescope, on the nights of 2006 August 31 and 2006 September 1, were already analyzed and published by Storchi-Bergmann et al. (2007). Here we re-analyze the same data, but only three of the nine data cubes which are centered on the AGN of NGC 6951. The exposures of 500 s have a FOV of 5″ × 7″ with a seeing of ∼ 0″.5 during the night, corresponding to a spatial resolution of ∼ 40 pc in the galaxy. The wavelength range was 5600-7000 Å, with a spectral resolution of $R \approx 2300$, or ≈ 130 km s^{-1}.

The data reduction was made in IRAF environment, which used the `gemini.gmos` package. The steps comprised bias subtraction, flat-fielding, correction of spatial distortions and wavelength calibration, at the end of the process, 3 data cubes were obtained with spatial pixels of 0″.1 × 0″.1. Then, we applied a data treatment very similar to the one apllied to the NIFS data cubes, including the following steps: DAF correction, median of the cubes, Butterworth spatial filtering and, finally, Richardson-Lucy deconvolution, with the FHWM of the constructed PSF having the same value of the weak Hα broad component found in the center. This is a better approach, since it comes from the data.

3 ANALYSIS AND RESULTS FOR THE EMISSION LINES: THE MOLECULAR GAS

3.1 The H_2 lines

In Fig. 5 we show the average spectrum of NGC 6951 in the K band, after the subtraction of the continuum, within an aperture of 0″.4, centered on the bulge. In this spectrum we can identify 6 H_2 ro-vibrational transitions, the Brγ λ21661 Å and HeI λ20585 Å lines. The continuum was subtracted by simply performing a spline function fitting, masking the emission lines regions, and later subtracting it from the original spectra. There are some reasons why we do not use a stellar population synthesis to perform this subtraction. Namely, because of the inaccurate fits given for such a short wavelength interval and the poor spectral resolution compared with the data.

In Fig. 4 (right panel), one can see that the image of the molecular gas presents a flat structure, possibly an edge-on disc, with PA=124°, with its extremities extending ap-

proximately perpendicularly to the flat structure, in opposite directions. Table 1 presents the measured fluxes for the H_2 emission lines of the spectra extracted from four circular regions, with radii of 0.1", at the positions identified in Fig. 6 (left panel), and also the total flux of the spectrum of a circular region, with a radius of 0.5", centred on the bulge. Due to the large calibration uncertainties, the errors in the absolute fluxes are of ∼30% or even higher, as pointed out by the multiplication factors applied before performing the median between the 4 data cubes.

As indicated in Fig. 6 (left), regions 1 and 2 fall along the PA=124°, while 3 and 4 represent the faint emission at the elongated ends. According to Storchi-Bergmann et al. (2007), the near side of the galaxy is to the southwest and the far side to the northeast, but it is interesting to note that, when comparing the relative intensities of the lines between regions 3 and 4, they are only slightly different, suggesting that there is no appreciable difference in dust extinction. In Fig. 6 (right panel), we show the same image in order to show the noise level and, thus, the region from where we can safely extract the molecular properties and make reliable fits.

3.2 H_2 kinematics

Fig. 7 shows RB composite images of the red and blue wings of the six H_2 lines, excluding two central spectral pixels, near the rest frame, for better visualization. The velocity range goes from -226 to -60 km s^{-1} for the blue wings and from +60 to +226 km s^{-1} for the red wings. Despite differences mainly due to the signal to noise ratio, they have all consistent kinematics.

In order to visualize the complete spatial distribution of the red and blue wings, Fig. 8 shows the sum of all images with normalized flux (left), and the image of the H_2 λ21218 Å line with velocities $v < -140$ km s^{-1} and $v > 140$ km s^{-1} (right), with the contours of the total distribution of the flux of this line. The six different regions denoted by letters correspond to the locations where we extracted the spectra of circular regions with radii of 0″.2, in order to determinate the H_2 λ21218 Å line profiles. They are all represented in Fig. 9, with the upper section showing the FWHM of the blueshifted line profiles increasing to more distant regions from the centre, with similar behaviour for the lines in the bottom section. Regions *b* and *e* have clearly asymmetric profiles and may represent the transition between two velocity regimes, one more turbulent and dominated by velocity dispersion and the other seen in the narrow line profiles located in the disc.

The narrow line profiles of regions 1 and 2 in Fig. 6 (left) represent the emission of a disc, with PA=124°, and with a thickness that is slightly above our resolution, giving a superior limit of ∼10 pc. This disc is connected to the turbulent gas associated with regions 3 and 4. These two velocity regimes behaviour can be originated by some interaction of the disk with a nuclear outflow, since outflows are characterized by high velocity dispersion, both for the cold and hot molecular gas (Martin 2006; Davies et al. 2014). This is strengthened by the orientation of the radio emission position angle, which agrees with the position angle of the turbulent gas (Fig. 7 right).

The velocity profiles shown in Fig. 10 were extracted

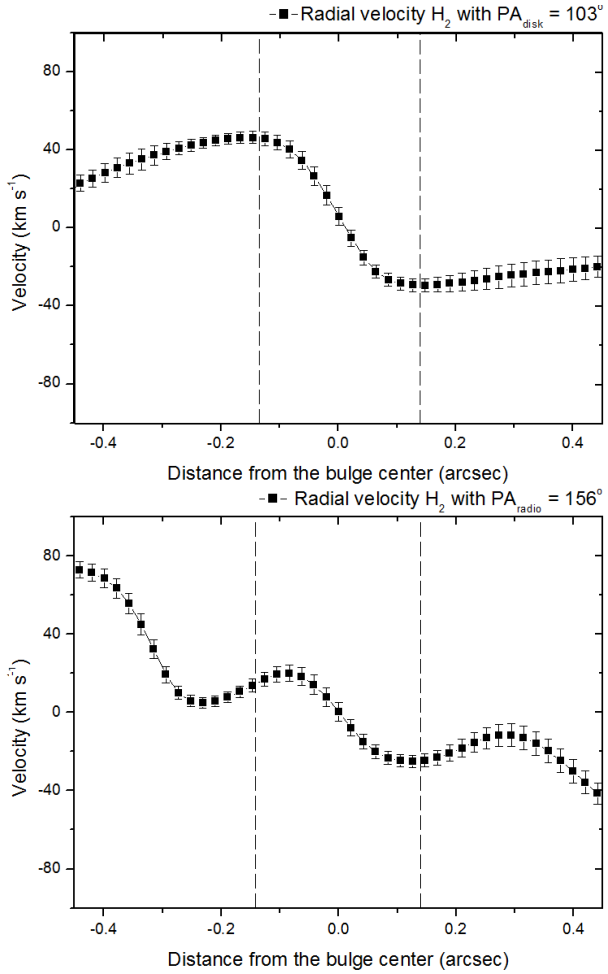

Figure 10. Radial velocity profile for the H_2 λ21218 Å line, taken along the position angles of (top) 103° and representing the molecular disk, and (bottom) 156°, the orientation of the radio emission. The vertical dashed lines denote the FWHM of the PSF.

from two different orientations, corresponding to the disc and the radio emission position angles, respectively, with a pseudo-slit equivalent to 0″.1 of width. The kinematic position angle for the disc, along the flat structure, is 103°±3°, and was inferred from the Gaussian fit of the H_2 λ21218 Å line, which is slightly different from what we measured in the structure of the flux map, which is 124°±6°. This difference means that the maximum velocity does not coincide with the maximum flux. The first radial velocity profile has, indeed, the characteristic curve of a disc, which does not decrease so steeply for large distances. The velocity range in the disc spans from +40 to -40 km s^{-1} and has an average velocity dispersion, corrected for the instrumental broadening, of 36 ±4 km s^{-1}, which is of the order of the radial velocity. The velocity profile along the orientation of the radio emission reaches ∼70 km s^{-1} in the turbulent regions, and have a higher velocity dispersion, of 69 ±2 km s^{-1} in region 1 (Fig. 6 left), and 70 ±2 km s^{-1} in region 2. Considering that the disc is seen close to edge-on, its measured velocities are probably close to the real values, but not the de-projected velocities coming from the turbulent regions along the jet orientation. Assuming an inclination of 90°for

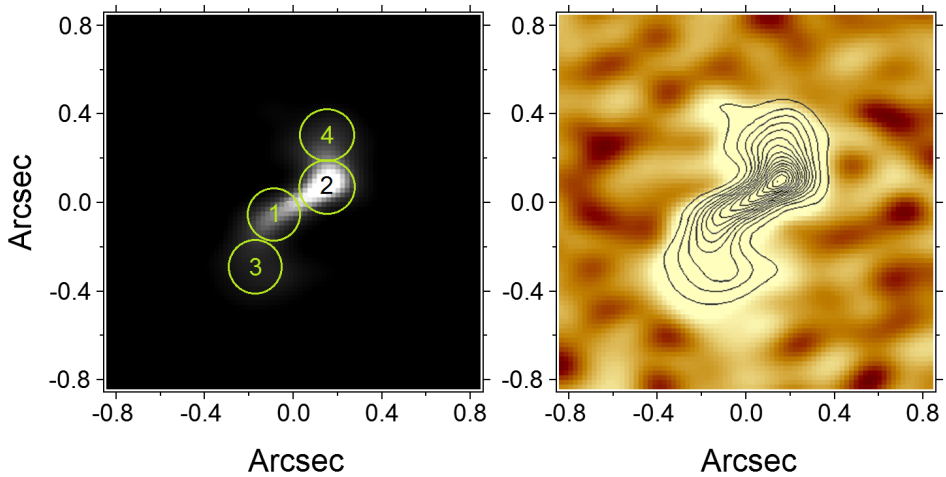

Figure 6. Left: average image of the H_2 lines, with the four regions with radii of $0''.2$, from which the line fluxes were extracted. Right: The same image, with contours, scaled to show the noise fluctuation, and the area of significant H_2 emission. The contour corresponding to the faintest emission has 1/8 of the flux peak.

Table 1. Measured H_2 emission line fluxes for the four circular regions marked in Fig. 6, with radii of $0''.2$ and the total emission within $1''$, including Brγ and He I lines. All values are in units of 10^{-16} erg s^{-1} cm^{-2}. The errors do not exceed the typical 30% of uncertainty in the flux calibration.

λ_{vac} (Å)	ID	1	2	3	4	Total
20 338	H_2 1-0 S(2)	2.94 ± 0.19	2.39 ± 0.22	1.43 ± 0.12	1.80 ± 0.09	12.72 ± 0.44
20 585	HeI	–	–	–	–	5.48 ± 0.51
20 735	H_2 2-1 S(3)	0.78 ± 0.09	0.67 ± 0.04	0.34 ± 0.03	0.46 ± 0.09	3.91 ± 0.58
21 218	H_2 1-0 S(1)	6.15 ± 0.15	6.40 ± 0.14	3.93 ± 0.24	4.24 ± 0.12	51.81 ± 1.89
21 661	Brγ	–	–	–	–	4.04 ± 0.76
22 235	H_2 1-0 S(0)	1.66 ± 0.17	1.84 ± 0.12	1.04 ± 0.14	1.33 ± 0.13	11.20 ± 1.26
22 477	H_2 2-1 S(1)	0.65 ± 0.13	0.50 ± 0.14	0.50 ± 0.10	0.42 ± 0.06	4.78 ± 1.57
24 066	H_2 1-0 Q(1)	5.78 ± 0.76	6.86 ± 0.42	3.58 ± 0.13	3.94 ± 0.35	43.39 ± 5.13

the H_2 disc, it is inclined with respect the main disc of the galaxy by $\sim 44°$.

Beyond $0''.45$, the extended H_2 emission has not enough signal-to-noise ratio to give a reliable fit (see the right panel of Fig. 6) and, in the turbulent regions, where the line profiles seem to have more than one Gaussian component, we may not have the best fits when the disc and the turbulent regions overlap.

3.3 PCA tomography of the molecular gas data cube

PCA is a statistical technique used to extract information from a large amount of data, calculating the correlations between its variables. It is defined as an orthogonal linear transformation which brings the data to a new uncorrelated coordinate system arranged such that the first of these coordinates (eigenvector E1) explains the highest fraction of the data variance, the second eigenvector explains the second highest fraction and so on. PCA Tomography (Steiner et al. 2009) is a method that consists of applying PCA to data cubes, where the variables are the spectral pixels and the observables correspond to the spaxels of the data cube. Since eigenvectors are obtained as a function of the wavelength, their correlations have a shape similar to the spectra; therefore they are called eigenspectra. On the other hand, the projections of the observables on the eigenvectors are also images, indicating where the correlations take place on the spatial coordinates. In order to interpret the results it is necessary to do the simultaneous analysis of eigenspectra and tomograms. For some applications see Ricci, Steiner & Menezes (2011), Schnorr Müller et al. (2011), Menezes, Steiner & Ricci (2013) and Ricci, Steiner & Menezes (2014).

In order to derive only the correlations between the molecular lines, we masked the Brγ λ21661 Å and HeI λ20585 Å recombination lines and applied the PCA Tomography to the masked data cube. The most significant eigenvctors obtained with this procedure are shown in Fig. 11.

One can see that the first eigenspectrum and the respective tomogram are quite similar, respectively, to the average spectrum and to the image of the H_2 λ21218 Å line. This is expected because eigenvector 1 explains most of the data variance (61.15%), although the NW side of the structure appears to be more prominent here because the tomogram has a higher weight where there is more emission in the data cube, comparing to the calculus of average emission. This structure has the same PA=$124° \pm 7°$of the average emission and the elongated extremities are almost perpendicular.

In eigenspectrum 2 (9,78% of the data variance), there are correlations between wavelengths corresponding to the

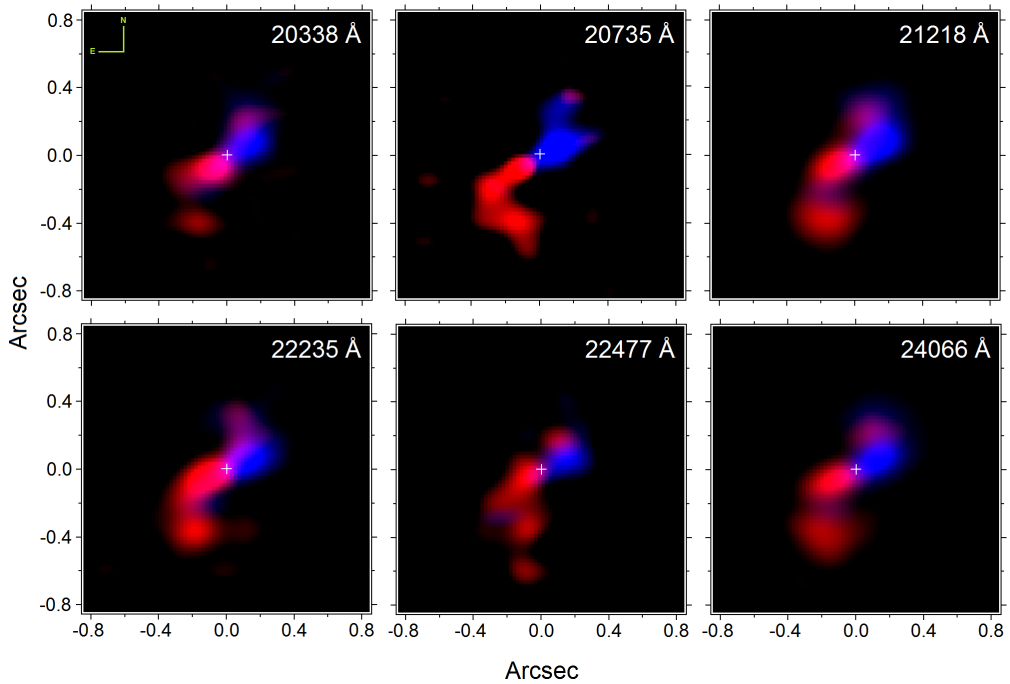

Figure 7. Images of the red and blue wings for the six H_2 line profiles, with a velocity range of ± 226 km s^{-1}. The white cross denotes the bulge centre.

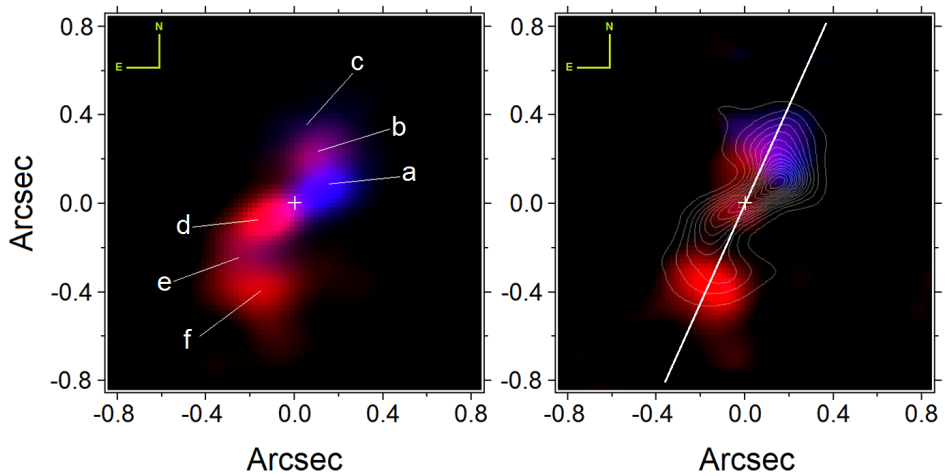

Figure 8. Left: sum of the images of Fig. 7 with normalized flux. The six regions mark the positions of the circular regions, with radii of $0''.2$, from which the H_2 λ 21218 $\AA$ line profiles were extracted. Right: the image of the same line with velocities $v < -140$ km s^{-1} and $v > 140$ km s^{-1} (that is, the blue and the red wings only), the white line shows the $PA_{radio} = 156°$, and the contours are the average emission of the H_2 lines.

red wings of all H_2 lines, which are anti-correlated to the wavelengths corresponding to the blue wings of these lines, indicating a kinematic phenomenon of the molecular gas. An analysis of the morphology of tomogram 2 reveals taht the blueshifted part of the line is in the NW part of the structure and the redshifted one in the SE part, with the bulge center exactly in the middle. Looking at the tomogram, there is also a kinematics associated with the turbulent region. The colors in Fig. 11 (middle) should be taken as the blueshift and redshift velocities with respect to the line of sight.

In eigenspectrum 3 (2,07% of the variance), the broad wings of the lines are correlated and have a weak anti-correlation to the narrow part of the central peaks. Our interpretation is that the bright areas of the tomogram correspond to the regions where the FHWM of the emission lines are broader and, therefore, where the higher values for the velocity dispersion are found. The spatial location for this correlations agrees with the previous image of the red and blue wings for the H_2 λ21218 Å line (top right of Fig. 8).

We can compare how the kinematic information of the tomograms is spatially related to the molecular structure, represented by the average data cube of the molecular gas. Fig. 12 shows tomograms 2 and 3 overlaid with the molecular structure (left and middle panels, respectively) and also

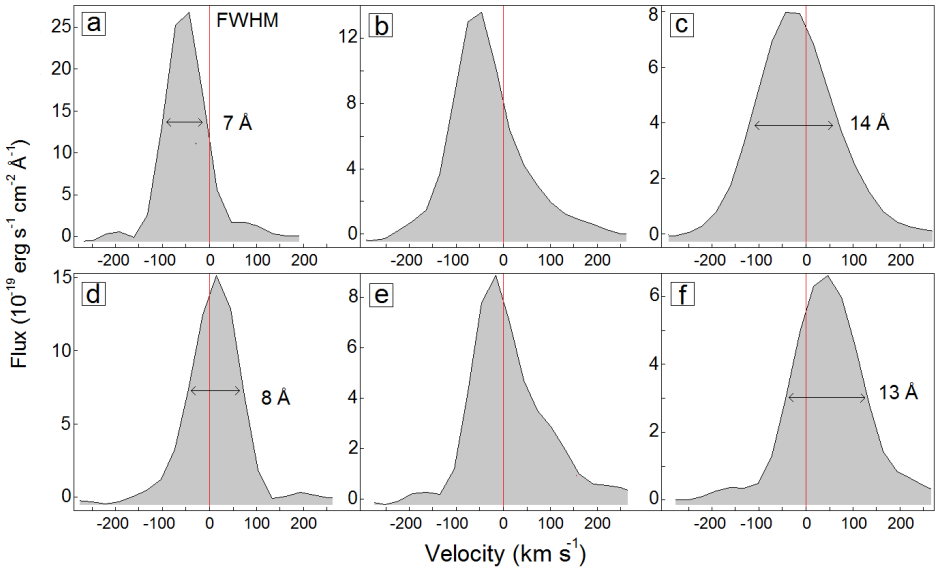

Figure 9. The H_2 λ 21218 $\AA$ line profiles for the six marked regions in Fig. 8. The vertical red line denotes the rest frame wavelength, with zero velocity.

tomogram 2 together with tomogram 3 (rifgt panel). The kinematics of the tomogram 1 is both associated with the disk (rotation) and the turbulent regions (outflow). Since the PCA analysis produces new uncorrelated eigenvectors, the tomograms interpreted as the gas kinematics are quite sensitive in representing the structures in different regimes of velocity, because the spectra resolution do not allow to properly select the wavelengths intervals in order to discriminate well between the displacement of the narrow line profile and the increase of the FWHM in the same direction.

3.4 Physical conditions of the molecular gas

The H_2 emission comes from rotational and vibrational transitions with $\Delta J = -2, 0, +2$, where odd rotational states are with parallel spins (*ortho*-H_2) and even J states with anti-parallel spins (*para*-H_2). For non-thermal excitation, followed by radioactive decay, the ratio between lines from *ortho* molecules are constant (0,5-0,6 for the ratio of the 2-1S(1)/1-0S(1) lines), but not for the *ortho-para* ratio. However, for thermal excitation, the *ortho-para* ratio is expected to be constant and ~ 3 for the 1-0S(0)/1-0S(1) ratio.

These lines can be excited in two ways: non-thermal process, through fluorescence by UV photons(Black & van Dishoeck 1987) and thermal process, produced either by X-ray (Maloney, Hollenbach & Tielens 1996) or by shock heating (Hollenbach, Chernoff & McKee 1989). The temperature range is from 514 K, for the first pure translational transition J(2-1), to $\sim$ 4000 K, when the molecule begins to be quickly destroyed by energetic collisions. The typical thermal value, where the excitation temperature is the same as the kinetic temperature, is $\sim$ 2000 K and with critical densities of about 10^{5-6} cm^{-3}.

In Table 1 we show the fluxes, non-corrected of extinction, for the detected emission lines. They were measured for four different regions (Fig. 6 left). Some useful line ratios are showed in Table 2. In Fig. 13 we present the line-ratio diagnostic diagram for the four regions over-plotted on a diagram extracted from Mouri (1994), comparing different excitation models.

In order to remove the effect of *ortho/para* ratio, the plot uses the intensity ratios of 2-1 S(1)/1-0 S(1) (which occur for *ortho* molecules) and 1-0 S(2)/1-0 S(0) (for *para* molecules), where non-thermal values are expected to be constant. The points for NGC 6951 lie closer to the thermal process area, right in the region compatible for shock excitation, where the temperature is too high for UV excitation and is still well discriminated from the X-ray excitation. Despite the error bars, the plot suggests that regions 3 and 4 lie closest to the theoretical point for shock heating process, making a possible distinction from regions 1 and 2, representing the disc.

3.4.1 H_2 Population Diagram

For the high density gas, which the collisional excitation and de-excitation are dominant, the relative populations of the ro-vibrational levels $n_{\nu J}$ are described by the Boltzmann distribution. Given the relative level of the H_2 transitions one may calculate the ratio of different population densities, which are proportional to the observed column densities, versus the energy of the upper level, in what is called a population diagram. For a thermally excited gas, all the transition values lie on a straight line and the corresponding slope is inversely proportional to the gas temperature. The column densities can be derived with the formula

$$N(\nu, J) = \frac{f}{A(\nu J, \nu' J')} \times \frac{\lambda}{hc} \times \frac{4\pi}{\Omega_{aper}} \qquad (1)$$

where f is the measured flux, $A(\nu J, \nu' J')$ is the transition probability from the (νJ) to the $(\nu' J')$ state (taken from Wolniewicz, Simbotin & Dalgarno (1998)), λ is the rest frame wavelength, h is the Planck constant, c is the speed of light and Ω_{aper} is the aperture with diameter of $0''.4$. By taking the logarithm of the ratio for two Boltzmann popu-

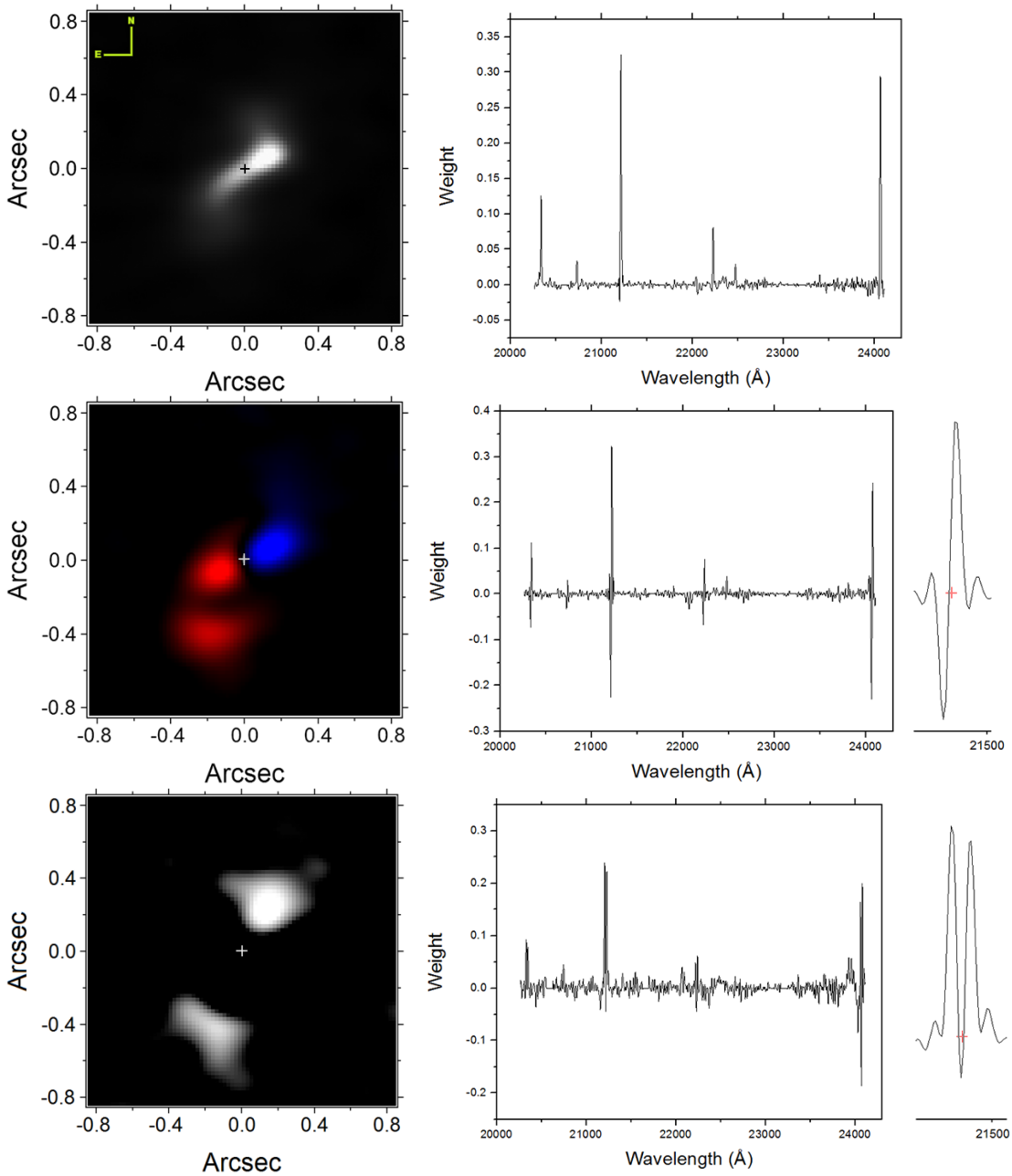

Figure 11. The first three tomograms and eigenspectra obtained with PCA Tomography of NGC 6951, from the NIFS data cube for the molecular gas. For better visualization, there is a zoom in the H_2 λ21218 Å wavelength. The cross denotes the bulge centre.

lations as function of the column density, normalized by the transition $(\nu J) = (1,3)$ (corresponding to the 1-0 S(1) line), we have the following equation

$$ln\frac{N(\nu J)/g_J}{N(1,3)/g_3} = \frac{-E(\nu J)/k}{T} + Constant \qquad (2)$$

The constant is independent of the transition. In Fig. 14 the H_2 population diagram for the four regions (shown in Fig. 6 left) is presented, showing the column densities normalized by the (1,3) transition, versus the energy of the upper level, in units of Kelvin.

The most remarkable feature of this analysis is the low ratio of the 1-0 S(0)/1-0 S(1) lines, which gives a large scatter around the derived value for the temperature of 2271 ±364 K (solid line). A second fit was performed excluding these data points and we found a more consistent value for the equilibrium temperature of 1988 ±68 K. Given the small errors bars, we conclude that this lack of emission in the 1-0 S(0) line is a real feature that must be explained by some physical process of the H_2 excitation. We calculated what would be the expected average flux for this line such as its derived temperature still was 1988 K (dashed line), and we found a deficit of 38% ±6%.

Supernova remnants have a typical value of ∼0.22 for this ratio (excitation by shocks Mouri 1994), closer to the value of ∼0.29 measured for NGC 6951. We argue that, taking into account the geometry of the molecular structure,

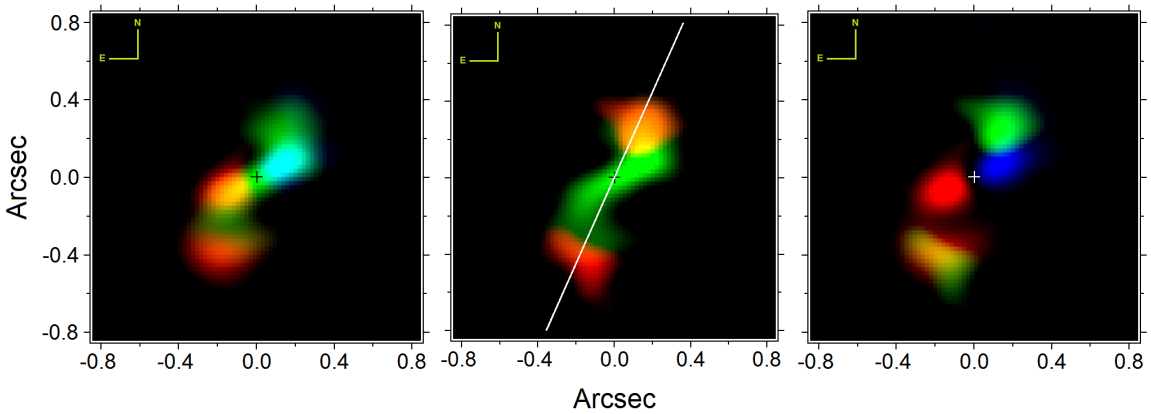

Figure 12. Left: the average data cube of the molecular emission lines (green) and tomogram 2, showing the blueshif and redshift velocities. Middle: the same for tomogram 3 (red), showing where the velocity dispersion is higher. The white line denotes the PA_{radio} = 156°. Right: tomogram 2 in blueshift and redshift, overlaid with tomogram 3 (green).

it is very unlikely that this is due supernova remnants but, instead, still be due shock events, directed by other source of energy. Similar ratios were found for several galaxies in the literature, which are attributed to shock excitation or present in very disturbed systems, like 0.28±0.05 for NGC 520, a merging system (Kotilainen et al. 2001), 0.29 for NGC 660, with two inclined dust lanes (Schinnerer & Scoville 2002), 0.24±0.01 for NGC 1266, probably exited by C-shocks (Pellegrini et al. 2013), 0.27±0.01 for NGC 1275, compatible with shock-excitation and turbulent heating (Scharwächter et al. 2013), 0.3±0.1 for NGC 5929 (Bower et al. 1993) and 0.18 for the galaxy Arp102B (Stauffer, Schild & Keel 1983), where the last two have a strong cloud-jet interaction.

This intrinsic low emission to the fundamental level of the molecule can be caused by the constant injection of energy in the molecular gas, such as the pre-shock region, which is supposed to be populated with lower transitions. In NGC 6951, we could not have the pre-shock region. The alternative for the supernova is the presence of a jet, where the free electrons continuously hit the molecular gas. In fact, the nucleus of NGC 6951 have been detected in the radio but just with a slightly eccentric emission, suggesting that the radio jet could be stopped by the dense distribution of gas.

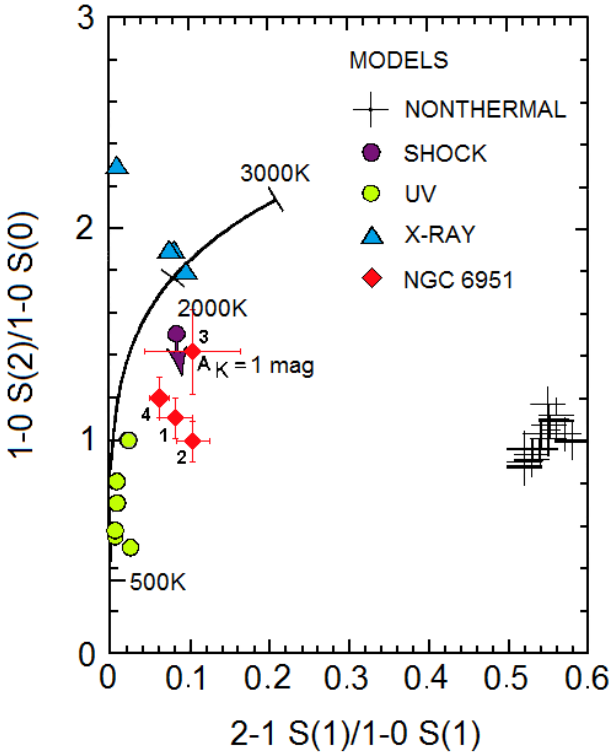

Figure 13. Plot of 2-1 S(1)/1-0 S(1) vs. 1-0 S(2)/1-0 S(0) from the diagram extracted from (Mouri 1994). Curves represent the thermal emission at 500-3000 K. Theoretical predictions were plotted for UV non-thermal values from models of (Black & van Dishoeck 1987) (crosses), for X-ray heating models by (Lepp & McCray 1983) (blue triangles), for thermal UV excitation models of (Sternberg & Dalgarno 1989) (green circles) and for the shock heating model of (Brand et al. 1989) (purple circle), with an arrow showing how the shock spectra are modified by the dust screen of A_K = 1 mag. We plotted the corresponding ratios for the four regions (marked in Fig. 6 left) of NGC 6951 (red diamonds).

4 ANALYSIS AND RESULTS FOR THE EMISSION LINES: THE IONIZED GAS

4.1 HST images: the ionization cone and the interstellar extinction

We analyzed images obtained with the Hubble Space Telescope (HST), taken from the HST archive, in the filters *F814W* (I band) and *F658N* (Hα + [N II]) from the instrument ACS WFC1, with scale of 0″.05 per pixel and in the *F547M* (V band) filter, taken with the WFPC2/PC with scale of 0″.046 per pixel. In Fig. 15 we show the Hα + [N II] image divided by the image in the I band, in order to highlight the structure for the ionized gas, the image of (V-I) with the contours of the previous image and another (V-I) image with the contours of the H_2 λ21218 Å line image. The bright regions in the (V-I) images correspond to higher extinctions.

The first image (representing the Hα + [N II] emission) shows a double structure, symmetric with respect to a weak central point-like emission. We interpret this double structure as two ionization cones, the NW component being

Table 2. Measured H_2 line ratios for the four circular regions marked in Fig. 6, with radii of $0''.2$ and the ratio for the total emission, within an aperture of $1''$. The ratio 1-0 S(1)/Brγ is also shown.

Line ratio	1	2	3	4	Total
$\frac{2-1S(1)}{1-0S(1)}$	0.10 ± 0.02	0.08 ± 0.02	0.13 ± 0.03	0.10 ± 0.02	0.09 ± 0.03
$\frac{1-0S(0)}{1-0S(1)}$	0.27 ± 0.03	0.29 ± 0.03	0.27 ± 0.05	0.31 ± 0.04	0.30 ± 0.04
$\frac{1-0S(2)}{1-0S(0)}$	1.77 ± 0.29	1.30 ± 0.19	1.37 ± 0.18	1.37 ± 0.27	1.14 ± 0.20
$\frac{1-0S(1)}{Br\gamma}$	9.38 ± 1.15	9.52 ± 1.89	–	–	12.82 ± 2.89

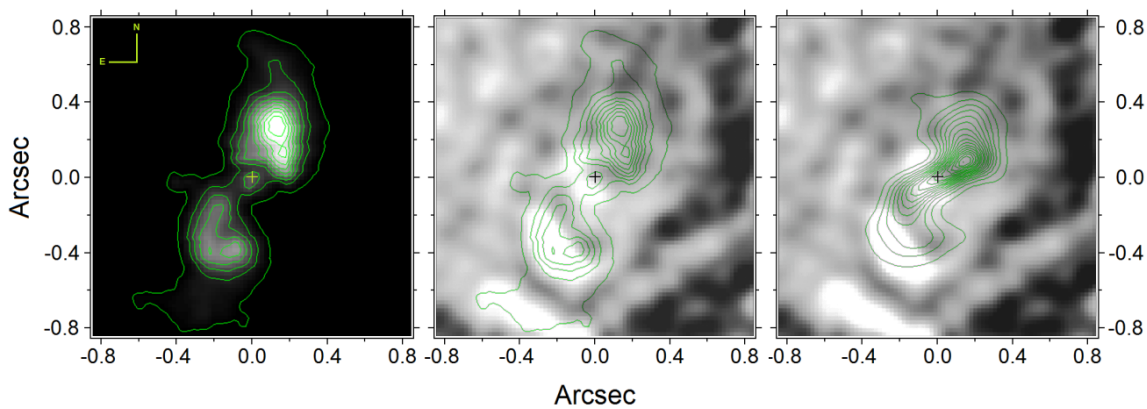

Figure 15. Left: Hα + [N II] image divided by the image in the I band. Middle: (V-I) image with the contours of the previous image. Right: (V-I) with the contours of the H_2 λ21218 Å line image. The dark regions correspond to higher extinctions.

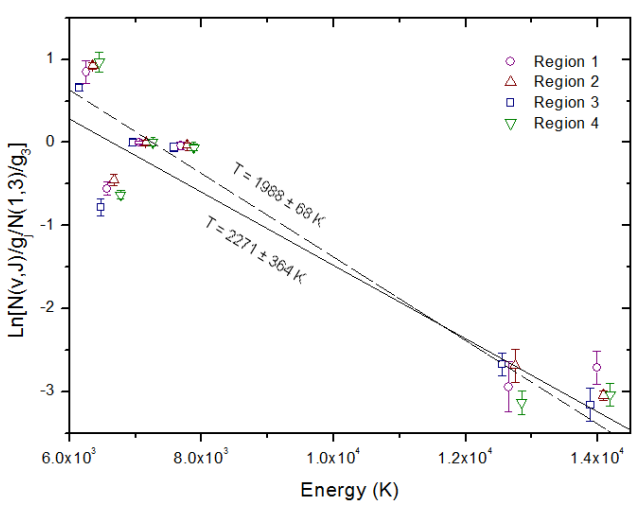

Figure 14. H_2 level population diagram relative to 1-0 S(1) for the four regions (marked in Fig. 6 left) of NGC 6951. The data points are spread by 100 K in x-direction to better visualization. The straight line is the linear fit with the slope consistent with an isothermal population at 2271 ±364 K and the dotted straight line is the linear fit without the 2-1 S(3) transition, giving a temperature of 1988 ±68 K.

twice as intense when compared to the SE component, which presents an arc shape. The central point-like weak emission coincides with the peak of the stellar bulge emission, seen in the I band. Hereafter we assume both the bulges, in the I and K band, having the same centre, which defines the AGN position. It is worth noticing there is only a weak emission in the vicinity around the AGN. The (V-I) image indicates where the extinction is higher (bright regions), which we attribute to the presence of dust. If we compare this image with the structure of the ionized gas, they do not seem to be correlated, i.e., there is no obscuration of the AGN by dust between the two ionization cones.

The last image in Fig. 15 also shows no correlation between the denser dust distribution and the molecular gas. This may appear contradictory, since the H2 molecules are formed on the surface of dust grains, but once formed, the gas could be heated up to temperatures above the sublimation temperature of the grains, of $\sim$ 1500 K. We calculated this temperature in the previous section as being $\sim$ 2000 K and, in fact, this can be the case. Therefore, the dust may be only associated with the distribution of the cold molecular gas. We also noticed there is no clear evidence of any structure that can indicate spiral arms on these scales.

Overlapping the image for the ionized gas from the HST with the average image of the molecular lines (Fig. 16 left), we see that the outflow is misaligned with the molecular gas in such a way that the ionization cones coincide mainly with the H_2 emission that is not distributed along the disc, suggesting some kind of interaction. The same can be said about the orientation of the radio emission, which coincides with that of the cones. The right image shows again the outflow and tomogram 3, which we interpret as representing

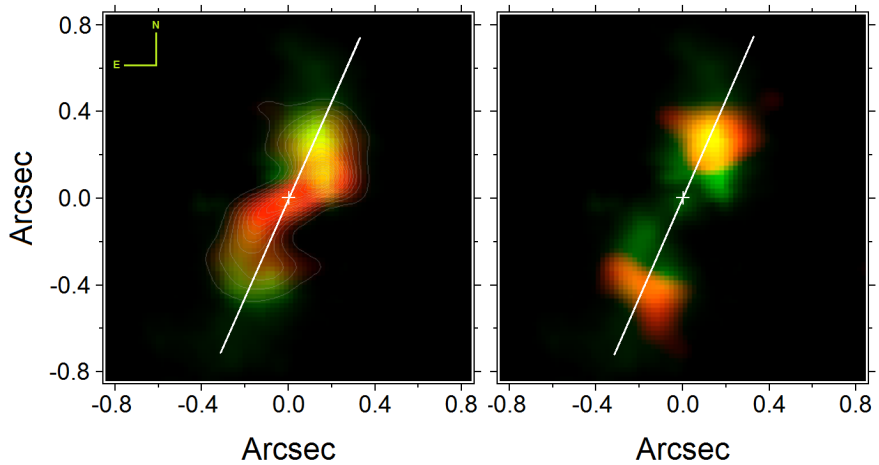

Figure 16. Left: average image of the molecular gas data cube (red with contours) and the Hα + [N II] image divided by the image in the I band (green). Right: the same image in green and tomogram 3 (red) obtained with PCA Tomography of the molecular gas data cube, indicating where the velocity dispersion is higher. The white line is the PA$_{Radio}$=156°.

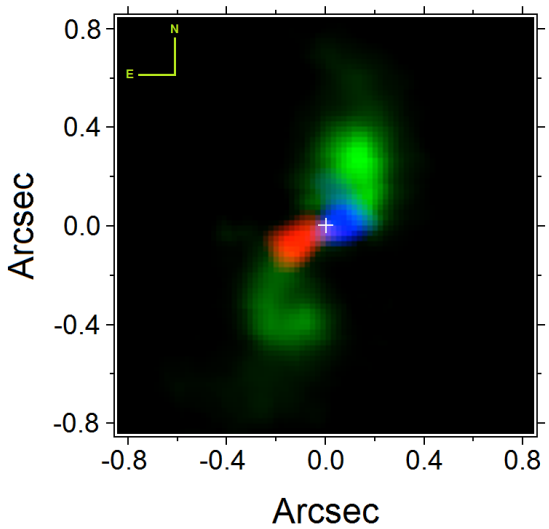

Figure 17. Image of the blue and red wings of the Brγ emission line with the Hα + [N II] image divided by the image in the I band (green).

the regions where the gas is more turbulent, and they are co-spatial with the extremities of the ionized gas and the radio jet.

4.2 The Brγ and He I emission

We detected a weak emission of Brγ, distributed in a similar PA of the molecular gas, extending from the centre until connecting with the structure of the Hα + [N II] image, with kinematics consistent with that found for the H_2 lines (Fig. 17).

This emission seems to fill the gap between the nucleus and the elongated ionization cones. This suggests that the emission seen in the HST image comes mostly from [N II], which is confirmed by Storchi-Bergmann et al. (2007), who found [N II]/H$\alpha = 4-5$ for the nucleus. In the next section we resume this discussion.

Taking the image from the blue and red wings of the line profile, we see that the kinematic centre the Brγ also agrees well with the adopted centre for the AGN, as the centre of the bulge in the K band. This kinematics can be compatible to that of the disc or to that of the ionization cones, but at this point we can not confirm from which it is referred. If this kinematics comes from the molecular disc, the hypothesis that its origin could come from the internal part of a torus can be ruled out since the physical scale for the internal radius of the torus (< 1 pc) is not resolved in our data. We measured the radial velocity, fitting one Gaussian to the Brγ emission line in the spectra of regions 1 and 2 (showed in the left panel of Fig. 6), and found a range from -40 km s^{-1} to 40 km s^{-1}, the same extracted from the molecular gas. For the velocity dispersion, we measured an average of 81 ±9 km s^{-1}, within an aperture of 1″. If the Brγ kinematics is related to the outflow, however, this implies an acceleration mechanism from the center to the regions where we measured the radial velocities for the turbulent gas, twice as large.

The high value of ∼13 for the H_2 λ 21218 Å/Brγ ratio, shown in Table 2, is well above the values found in literature, and far from the typical values $\lesssim$0.6 for starburst galaxies (Mazzalay et al. (2013), Rodríguez-Ardila et al. (2004), Rodríguez-Ardila, Riffel & Pastoriza (2005)). In fact, this galaxy has no indication of any expressive star formation occurring at its nucleus (van der Laan et al. 2013). As argued in Sect 3.4.1, for the molecular gas, it is again unlikely that the Brγ emission comes from supernova remnants, due its distribution and kinematics. We attribute the excitation mechanism of this line as due to shock process, driven by the jet.

In Fig. 18 we show the image of the integrated flux of the He I emission, which is asymmetric compared to the distribution of the molecular gas and with respect to the most intense Brγ emission. Thus, we have a larger flux for the He I line in the SE part of the nucleus and the opposite case for the Brγ emission. We emphasize that the He I line is located in a very noisy interval of the spectrum and even filtering the high frequency noise, the remained line profile may be affected by atmospheric absorption features.

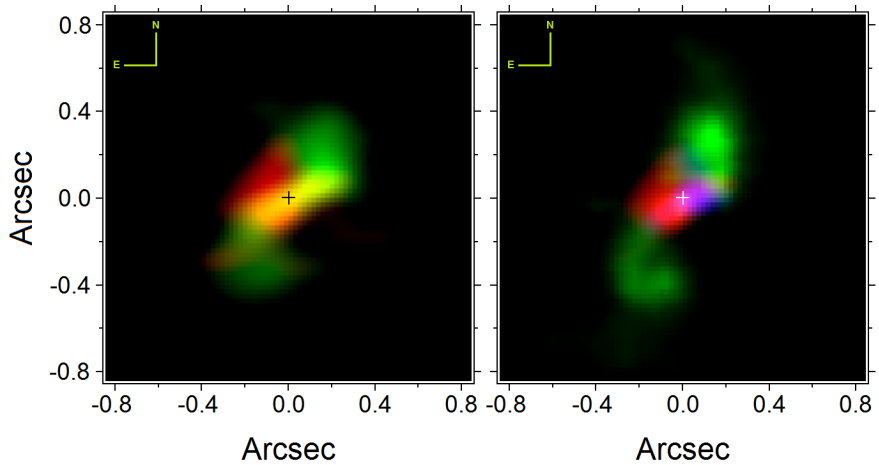

Figure 18. Left: average image of the molecular gas (green) and the He I image (red). Right: He I (red), Brγ (blue) and (Hα + [N II])/I (green)

4.3 The GMOS data cube

In order to analyze the gas in the optical part of the spectrum, we took only the region inside the ring, corresponding to the same FOV and orientation used to analyze the NIFS data, and again subtracted of the stellar emission. However, in ths case, we performed a stellar population synthesis in each spectrum of the data cube, with the STARLIGHT Software (Cid Fernandes et al. 2005) and the observed base of Bruzual & Charlot (2003). The stellar synthesis provides synthetic stellar spectra, from which the stellar data cube is generated. The stellar data cube is then used to subtract the stellar contribution from the total emission in the original data cube, as well the dust and featureless continuum contribution, to obtain the data cube of the emission lines.

Fig. 19 is shown the average image of the subtracted data cube, which comprises only the emission lines, with the spectrum centred in the bulge. The bulge centre in the optical is marked with a cross and we see that the distribution of the ionized gas is clearly asymmetric with respect to the centre of the bulge. One possible explanation that the displaced distribution of the integrated flux for the ionized gas with respect to the bulge centre, comes from the asymmetric distribution of dust in the nucleus. This is confirmed by Fig. 15 (middle panel), where the right side of the image is more susceptible to dust extinction, an effect that can be pronounced when the resolution is 10 times inferior. In this case, the centre of the bulge in the optical will be shifted to the left. From the HST image (whose centre was compared to the bulge in the I band), we see that the emission from the ionized gas do not suffer the same effect.

4.4 PCA Tomography of the GMOS data cube for the emission lines

The first three eigenspectra and tomograms obtained with PCA Tomography of the subtracted data cube are presented in Fig. 20. The first eigenspectra and tomograms gives basically the same information given by the average image and spectrum shown in Fig. 19, as it corresponds to 88.39% of the total variance. The second eigenspectrum (7.65% of the variance) shows an anti-correlation between the blue and red wings of all emission lines, which indicates a kinematic phenomenon of the gas. Since we defined the structure showed by the HST image as two ionization cones, with a similar orientation to this second tomogram, we interpret this tomogram as being the kinematics of the these two ionization cones seen nearly edge-on, with PA=144°±3°. The NW cone is the near side and is above the galactic plane. Eigenspectrum 3 shows similar correlations between the broad wings of the emission lines and anti-correlations between the narrow profile of the same lines, also seen in eigenspectrum 3 obtained with PCA Tomography of the molecular gas data cube. Again we interpret this result as being due the differences in the FWHM of the lines in regions where the velocity dispersion is higher, highlighting the spatial location where the gas is more turbulent.

In Fig. 21 (left) we show tomogram 2, spatially coincident with the image of the ionized gas from the HST; although the resolution here is $\sim$ 6 times lower than that of the HST image. This tomogram gives information of which side of the cone is approaching and moving away from us.

It is important to emphasize that tomograms 2 and 3 obtained with PCA Tomography applied to both GMOS and NIFS data cubes, respectively, reveal features that were detected only with this technique. In Fig. 21 (right), we compare the third tomogram of each PCA Tomography, which shows the corresponding regions for higher velocity dispersion, and we see they have a similar morphologies and the observed structures are located close to the edge of the ionization cone, along the position angle of the radio jet. It is interesting to note that, in this turbulent region, the molecules and the ionized gas survive at the same location, clearly with different temperatures (to be calculated in the next session).

The morphology of the turbulent molecular gas is better shown by tomogram 3 than by the simple image of the line profile for higher velocities. Such morphology reveals real features possibly originated by the gas being shocked by the outflow in this projected view. For the turbulent ionized gas, there is a small offset from the radio PA. This may be due the presence of a wind originated in the spots where the jet collides with the disk or/and the expanding gas into regions with lower densities. The contours of the HST image for the Hα + [N II] emission have a curvature that follows this

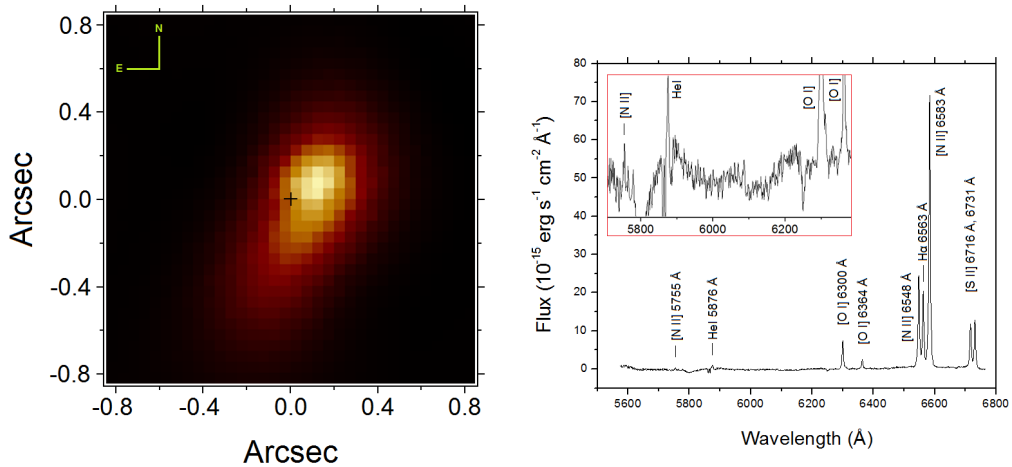

Figure 19. Average data cube of the emission lines in the optical, from the GMOS data, and corresponding average spectrum, within an aperture of 0″.4, with a zoom in the left side.

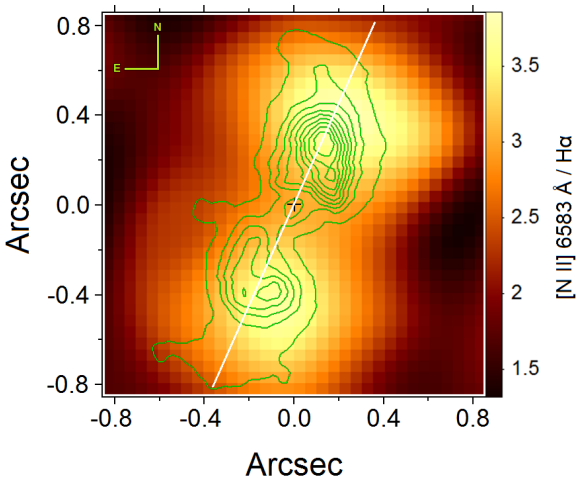

Figure 22. Image of the [N II]/Hα ratio with the contours of the HST image of the same lines. The white line gives the PA_{radio}=156°.

offset and show more intense emission where the dispersion is higher for the H_2 molecules.

4.5 The optical line ratios and the physical conditions

Another useful line ratio to investigate the excitation mechanism is the [N II]/Hα ratio, which can be calculated for each spaxel in the entire FOV, comprising the regions of the nucleus and of the outflow. Fig. 22 shows this result for the GMOS data, together with the contours of the HST *F658N* image. Both show a bipolar structure, centred on the AGN, with similar position angles. But it is important to notice that the maximum [N II]/Hα ratio does not coincide with the maximum emission of the ionization cone (the contours in Fig. 22).The ratios are in the range of [N II]/Hα∼ 1-3.8 and have a typical value of ∼2.5, with maximum of ∼3.8 at 53 pc in the NW and SE direction from the nucleus. The position angle connecting the two areas with the highest values of [N II]/Hα is PA∼160°, consistent with the PA of the radio emission. In contrast, the regions of star formation in the stellar ring have values between [N II]/Hα = 0.3 − 0.4 (Storchi-Bergmann et al. 2007), typical of H II regions. This values compare well with M51 (∼3.8), another galaxy with high [N II]/Hα, which have a strong jet-cloud interaction in the region with the high HCN/CO ratio (Kuno & Nakai 1996).

In order to infer the temperature of the ionized gas, we used the `NEBULAR` package under the `IRAF` environment (Shaw & Dufour 1995), with the calculations proposed by (De Robertis, Dufour & Hunt 1987). We computed the [S II] λ6716/[S II] λ6731 and the [N II] λ5755/[N II] λ6583 ratios in order to find a value for the electronic density n_e and temperature which converge for the measured ratios, and we obtained T = 6220 $\pm^{236}_{190}$ K.

4.6 Kinematics of the Hα and [N II] lines

The radial velocity and velocity dispersion maps of the Hα and [N II] lines were obtained with the same program used to extract the H_2 kinematics, which fits just one Gaussian component to each emission line. We show the results in Fig. 23 for the radial velocity and in Fig. 24 for the velocity dispersion. The Hα velocity range is of 85 km s^{-1} to -95 km s^{-1} along the kinematic PA=121°±2°. The [N II] kinematics have consistent values of 75 km s^{-1} to -85 km s^{-1}, with PA=121°±2°. The position angles were calculated by the method described in Appendix C of Krajnović et al. (2006), using an *IDL* program implemented by Michele Cappellari. The Hα radial velocity is clearly not circular and we argue that it is disturbed by the outflow, since the deviations are in a similar PA as that of the ionization cone.

The velocity dispersion maps show, for both lines, a double peak symmetrically located along the same direction of the ionization cone, reaching a maximum of ∼184 km s^{-1}. However, the peak for the [N II] line is displaced from the Hα peak by 26.3 pc and -7.0 pc along the x and y directions respectively, and is closer to the PA of the radio emission. Both peaks do not coincide with the peaks of the Hα+[N II] emission seen in the HST image but, instead, they are located right after its extremities (which can be seen in the

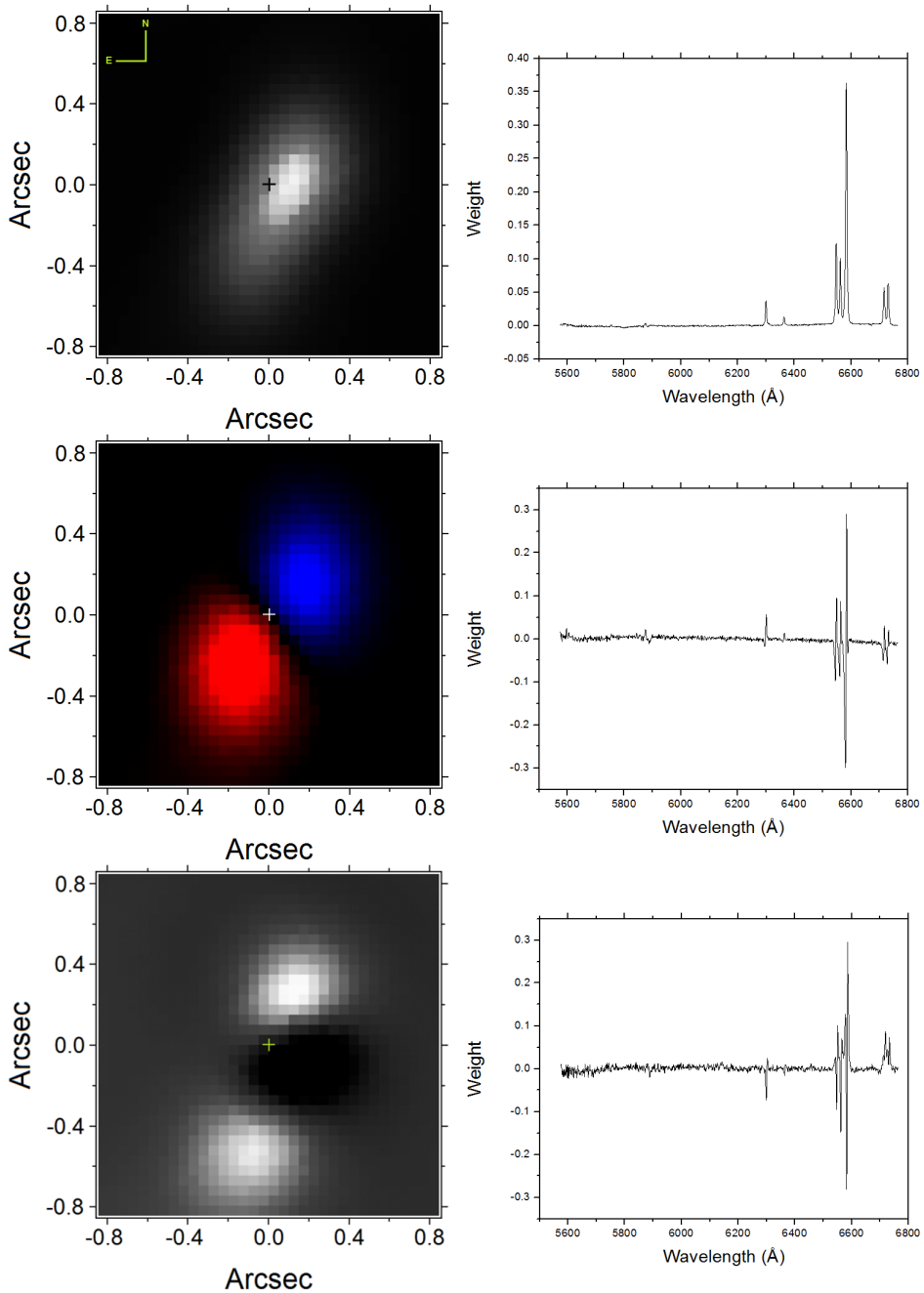

Figure 20. The first three tomograms and eigenspectra obtained with PCA Tomography of NGC 6951, from the GMOS data cube for the ionized gas.

velocity dispersion measurements along the radio PA, in the graphics of Fig. 23), suggesting where the ionized gas accumulates in the pos-shock region. At the edge of the maps, there is not enough signal to noise ratio to draw any conclusions. This distribution confirms that the outflow is being collimated by a nearly edge-on structure.

The distribution for the [N II]/Hα ratio, shown in Fig. 22, also shows a bipolar structure, similar to the velocity dispersion, and, in Fig. 25, we can see a strong correlation between their structures, more in the NW direction than in the SE. This suggests that the excitation of the gas could be partly due its kinematics, given firstly by the interaction of the jet with the molecular gas and then in the extended regions of the shocked gas.

The H_2 gas shows broader line profiles at the same direction of the ionized outflow, but with the turbulent region of the molecular gas spatially less extended. The H_2 molecule is destroyed by shocks faster than $\sim$25 km s^{-1}, but here we have values up to 100 km s^{-1}, which suggests that the molecular gas is being rapidly swept in form of small clumps, together with the ionized gas, and it survives until these clumps are disrupted.

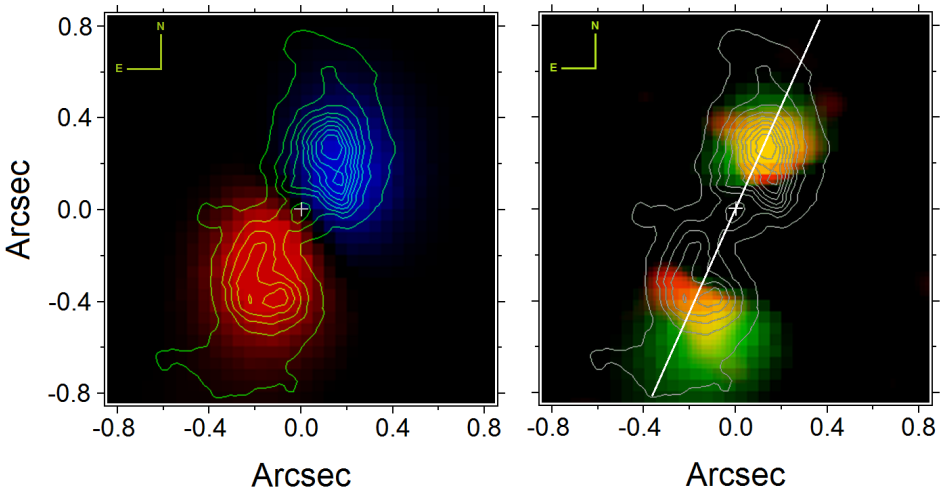

Figure 21. Left: Tomogram 2 obtained with PCA Tomography of the GMOS data cube, with the regions corresponding to positive and negative velocities shown in red and blue, respectively Right: tomograms 3 for the GMOS (green) and NIFS (red). The white line gives the PA_{Radio}=156°. The contours of the *F658N* image are superposed to both images

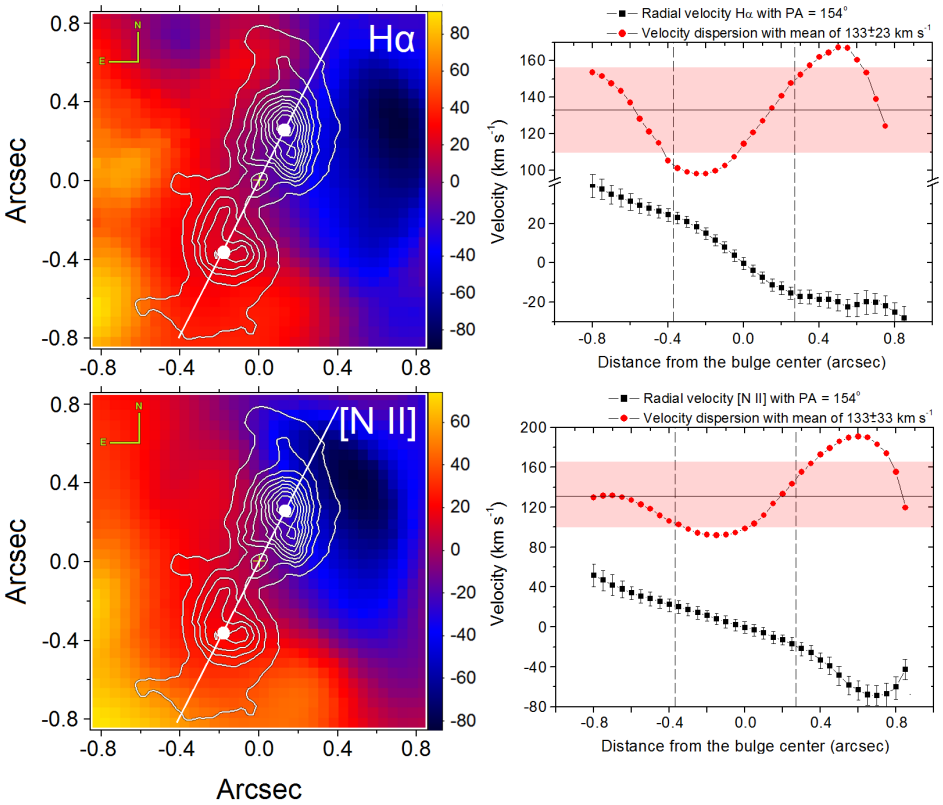

Figure 23. Top left: Hα velocity map. Superposed to this image are the contours of the HST image of the ionized gas. The filled circles correspond to the regions of the bi-cone with highest intensity. The white line represents the PA_{cone}=154°±1°. Top right: radial velocity and velocity dispersion profiles (black squares and red circles, respectively) along the same PA. Bottom: the same for the [N II] line. The vertical black lines on both graphics denote the angular distance from the centre to the maximum of intensity and the red filled area is the 1 σ interval of the mean velocity dispersion.

5 THE STELLAR COMPONENT

5.1 The Sersic index

In order to investigate if the galaxy bulge, defined within the stellar ring, is classified as a classic bulge or pseudo-bulge, we fitted a Sersic profile both in the K band of NIFS and in the I band of the HST. We obtained indexes of 1.8 ±0.2, and 2.1 ±0.1, respectively (measured within the same FOV of $3'' \times 3''$). The Sersic index is a good discriminant between classical and pseudo-bulges. Most of the pseudo-bulges have $n < 2$ while classical bulges $n > 2$ (Fisher & Drory (2008)

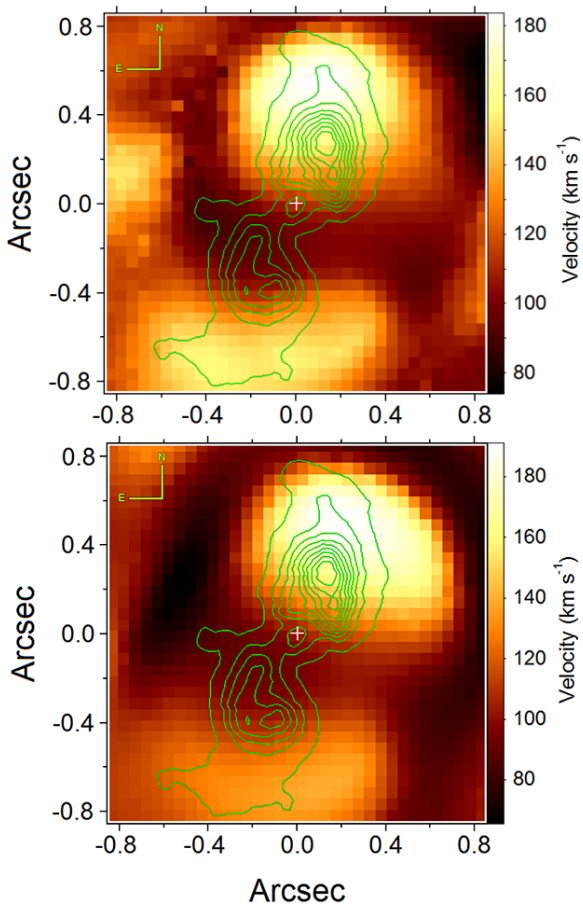

Figure 24. Top: Hα velocity dispersion map. Bottom: velocity dispersion map of the [N II] line. The contours are from the HST *F658N* image.

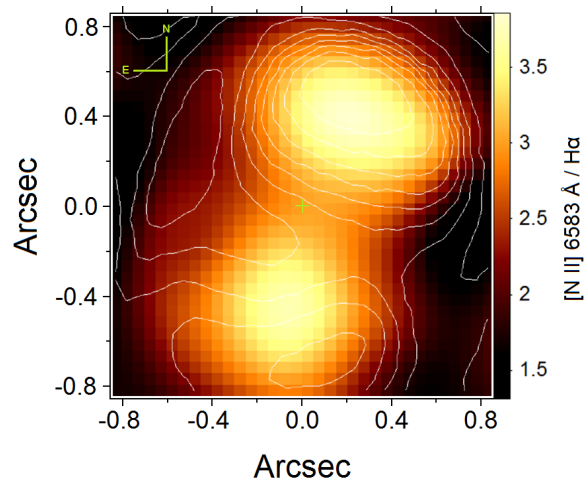

Figure 25. [N II]/Hα ratio and the contours of the velocity dispersion map of the [N II] line.

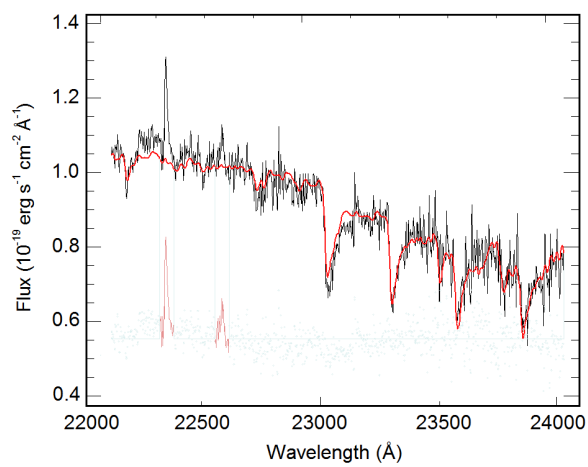

Figure 26. Example of fit of the nuclear stellar kinematics using pPXF, masking the emission lines. The observed spectrum is shown in black and the resulting fit in red, for one single spaxel

Kormendy & Kennicutt (2004)). We found consistent indexes in the K and I bands of ∼2. Together with the fact that NGC 6951 hosts a large scale bar, which is connected to a prominent stellar ring and nuclear spiral dust structures, such morphological signatures lead to the conclusion that this galaxy has, indeed, a pseudo-bulge.

The models suggest that the way the SMBH grows in pseudo-bulges does not affect galaxy formation (Greene, Ho & Barth 2008) and Kormendy, Bender & Cornell (2011) found that the current feeding process, which is not well known, leads to a little or no co-evolution of BHs with any component of the host galaxy.

This large scale bar connects to a nuclear ring of star formation but, within this ring, no young stellar population was found, only a bulge-like profile of old stars, with age > 3 Gyr (van der Laan et al. 2013). Together with this old component, the optical images from the HST reveal spiral structures of gas that are not forming new stars. Since they are an old population and with a pseudo-bulge profile, this suggests they also were formed through secular evolution. We performed a subtraction between the image of the bulge and the image of the exponential model with this index, for the K and I bands, to check if any stellar substructure would appear, but no one was identified.

5.2 The stellar kinematics

To extract the stellar line-of-sight velocity distribution (LOSVD) we used the ^{12}CO and ^{13}CO stellar absorption bands to fit the best combination of a stellar template spectra (Winge, Riffel & Storchi-Bergmann 2009), convolved with a Gauss-Hermite series. This is done for each spaxel in the data cube, after we mask all the emission lines before the fitting procedure. The best-fitting parameters are computed by the *Penalized Pixel Fitting* (pPXF) method, implemented by Cappellari & Emsellem (2004), and at the end of the process each individual spaxel has a correspondent value for the velocity. In Fig. 26 we show one fit (in red) of the spectrum of the nuclear region and the Fig. 27 shows the velocity map for the stellar field, which gives a kinematic PA=143°±2°.

The redshift provided by the NED is $z = 0.00475$ and, assuming circular orbits, we found a difference of 33 km s^{-1} for the velocity in the centre of the bulge, with the spectra corrected for this redshift. This value was corrected to be fixed as zero velocity, subtracting the same velocity from the

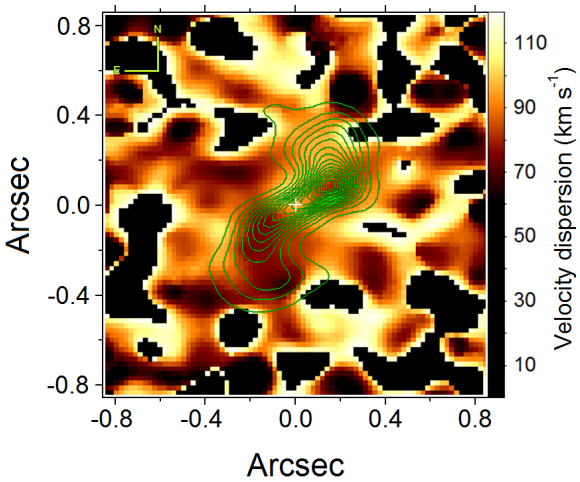

Figure 28. Velocity dispersion map of the stars with the contours of the molecular structure. The regions with low S/N are masked in black.

pixels of the FOV, resulting in a new redshift of $z = 0.00486$. This is of the order of the spectral resolution (~ 45 km s^{-1}). The projected velocity range within $\sim 0''.3$, the region with higher signal to noise ratio, is from -35 to +35 km s^{-1}.

For the velocity dispersion (Fig. 28), we have a mean of $\sim$97 km s^{-1}, within $\sim 0''.4$, weighted by intensity. The relation between the velocity dispersion of the ionized gas and of the stars is $\sim$1 (Chen, Hao & Wang 2008), but here the dynamics of the hot gas is clearly affected by the outflow, having an average velocity dispersion of $\sim$130 km s^{-1} for the Hα line. In the same figure, together with the velocity dispersion map, we show the contours of the molecular structure and we do not see any clear evidence that the values are lower in the region of the disc. Regarding there is no hint of a stellar substructure and that the stellar kinematic position angle is 19°higher than the measured value for the molecular gas, we conclude that the stellar dynamics is not correlated with the gas dynamics. This would be important to infer the presence of stellar nuclear bar, which we do not see.

In Fig. 27, in the right of the velocity map, we plotted the radial velocity profile along the kinematic position angle of 143°, with the velocity dispersion for the same position angle. A mean velocity dispersion of 87 $\pm$8 km s^{-1} was found. In addition, we detected a curious feature: the velocity dispersion is lower and nearly constant for the redshifted velocities (79 $\pm$4 km s^{-1}) and rise for blueshifted velocities (94 $\pm$2 km s^{-1}), 15 $\pm$ 6 km s^{-1} higher.

6 DISCUSSION

The two most important large scale phenomena associated with AGNs, which are the inflow and outflow of gas, are supposed to be always present at the same time Martini & Pogge 1999; Storchi-Bergmann 2010; Davies et al. 2014, although not always both are observable or well discriminated. In fact, the AGN feedback is easily traced by the emission lines of the ionized gas, while the evidences of gas inflowing are much more difficult to detect, because the radial inflow rate could not be reliably measured up to date, despite the indirect evidences of nuclear spirals and bars being able to drive the gas to the central region of galaxies (Haan et al. 2009). The inflow is necessary to feed the SMBH and accounts for the observed energy generated and transferred to the ISM, which in turn is heated and blown away in the form of winds or jets.

In the case of NGC 6951, there is a claim of evidence of inflow seen in the Hα kinematics (Storchi-Bergmann et al. 2007) and at least the indirect evidence due to the presence of the central molecular gas. However, there is no kinematic evidence that can lead to how it happened in the past. On the other hand, for the outflow we, see evidences of an ionization cone in the HST image as well as in the ionized gas emission of the NIFS and GMOS data cubes.

6.1 The molecular disc as inflated by the jet

We have mentioned in Sec. 1 some possibilities of how the misalignment of the jet, defined by the inner disc plane, with the torus/galactic disk could occur. We can now ask what happens if this misalignment is large enough for the jet to collide with the outer molecular disk, which seems to be the case of NGC 6951.

This hypothesis was explored by Zou & Gong (2012), in a model where a large misalignment is produced by a warped inner disc, and the scheme proposed in their work was adapted (see Fig. 29) to match the orientation of our data. These authors proposed that the collision is given by the interaction of the free electrons from the jet, with relativistic velocities, and the slow barions in the disc, ejecting the gas out of the disc, increasing the turbulence and heating the molecules. The scheme in the left of Fig. 29 shows, instead of an edge-on disc, a slightly tilted disc, in order to see the proposed orientation of the jet.

In the right of Fig. 29, we compare the model with our real data: the jet direction given by the hypothetical inclined inner accretion disc (warped or not), not seen in our data, interacting with the inner walls of the molecular disc. It is worth mentioning that the ionization cone, not shown in the model, follows a similar orientation of the jet. In other words, the cone is not collimated by the detected molecular disk. The kinematics of the cones was revealed by PCA tomography and in Fig. 23, with the approaching side corresponding to the NW region from the nucleus, and so, the near side of the jet, where we found the most intense average emission in the molecular lines. The orientation of the ionization cones are consistent with three more features: the position angle of the radio jet and the larger velocity dispersions in the H_2 and ionized lines (Fig. 21, right). The larger velocity dispersion is likely associated with turbulence, possibly induced by the radio jet. The turbulent gas is heated either by the high velocity electrons or shock heating due the turbulence. This may be the reason of why the [N II]/Hα ratio is also higher at this position. The high velocity dispersion regions likely consist of partially ionized gas; here the X-ray emission from the AGN may also play a role in heating the gas (Halpern & Steiner 1983).

The scenario where a jet hits the disc and ejects some of the gas in form of a turbulent outflow seems to be consistent with our observations, although we can not infer how the connection between the visible molecular disk with the hypothetical accretion disk, is given.

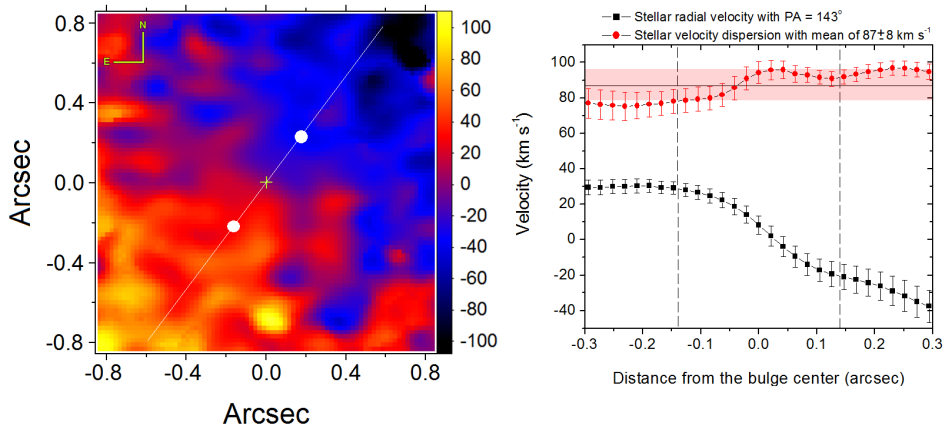

Figure 27. Left: Stellar velocity map obtained from the pPXF fit. The corresponding kinematic axis has a PA=143°. Right: velocity profile (black squares) and velocity dispersion (red squares) along the kinematic axis. The white filled circles in the image denote the range of the plot, in the graphic the dashed vertical lines are the PSF FWHM and the upper line is the mean velocity dispersion within 1 σ interval.

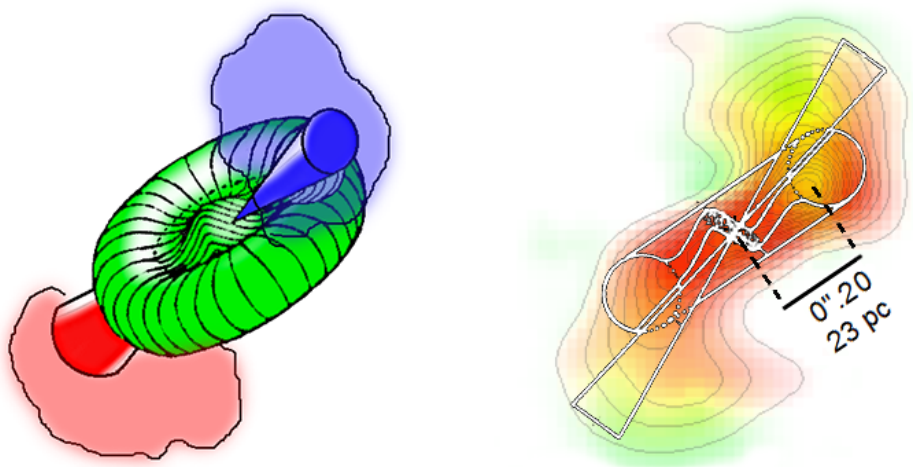

Figure 29. Left: adaptation of the scheme presented by (Zou & Gong 2012), showing the interaction of the jet with the outer disc. Right: edge-on view of the model overlayed with the real data for the molecular (red) and ionized gas (green) (right).

The existence of internal warped accretion discs, as seen by maser emission, is well documented (like in Circinus (Greenhill et al. 2003), NGC 4258 (Herrnstein et al. 2005) and four out of seven galaxies analyzed in Kuo et al. (2011). Although evidence for precession can be only seen in extended radio jets, there is also the possibility of a precessing jet (Carrara et al. (1993), Abraham & Romero (1999)). In this case, the origin of the warp of the inner disc can be related to the misalignment between the SMBH spin and the rotation direction of the disc, such as the warp can propagate in the disc through viscosity (Pringle 1992), what is called of Bardeen-Petterson effect (Bardeen & Petterson 1975). However, this effect accounts only for small scales, of the order of the accretion disc. The misalignment between the outer disc and the galaxy disc should be explained by other mechanism or have a distinct origin. This does not change our jet-disc interaction scenario.

6.2 Nature of the H_2 disc

NGC 6951 is an active twin of the Milky Way, both sharing the same morphology type of a SAB(rs)bc galaxy(de Vaucouleurs & Pence 1978). This can bring a valuable comparison between their nuclei, once we are able to draw the central architecture of our galaxy with a spatial scale of subparsec (see the work of Ferrière 2012) for an overview of the studies of molecular clouds in the Galactic centre).

Among a distribution of clouds spanning a wide range of sizes and shapes, we draw attention to the molecular ring (also known as CND - Circumnuclear disc) surrounding the mini spiral around Sgr A*, detected in molecular emission, like HCN, and very close to the nucleus (Guesten et al. 1987; Jackson, Heyer & Paglione 1993; Genzel, Eisenhauer & Gillessen 2010). The ring has an inner and outer radius are of ∼1-4 pc, respectively, with a thickness of ∼1 pc. This ring is tilted of ∼20° from the Galactic disc and its kinematics agrees reasonably well with that expected for rotation of a tilted ring, with de-projected velocity of ∼110 km s^{-1} and velocity dispersion ∼55 km s^{-1} near the inner edge (Guesten

et al. 1987). Jackson, Heyer & Paglione (1993) interpreted the kinematics of this ring as separated streamers, with indications that the inner part is connected with the ionized streamers filling the central cavity (Montero-Castaño, Herrnstein & Ho 2009; Zhao et al. 2010). There are also observations from the HST/NICMOS of a hot H_2 gas associated with the HCN emission within the ring (Yusef-Zadeh et al. 2001), probably heated in the dissipation of the random motion of molecular clumps in the ring. The neutral gas clouds are probably loosing angular momentum by collisions within this turbulent environment. This molecular ring is the closest structure to the Sgr A* source that we could call a torus in the Galactic centre, which in turn would not be connected to an eventual formation of an accretion disc.

The molecular ring in the Milky Way is not aligned with the Galactic disc, which is also the case of NGC 6951, suggesting that the nucleus can host, on these scales, multiple structures with different dimensions and alignments. The molecular structure in NGC 6951 has an outer radius, measured at $0''.4$, of 47 pc, and have superior limit for the thickness of $\sim$10 pc, roughly 10 times the dimensions found for the circumnuclear ring of the Milky Way.

The radius of influence of the BH in the Milky Way is $\sim$ 3 pc, which comprises most of its molecular ring. The mass of the SMBH in NGC 6951 is at most 2 times that of the Milky Way (to be calculated in 6.4). This results in a similar radius of influence, such that the outer radius of the molecular disc in NGC 6951 turns out to be larger than the sphere of influence of the central BH. Therefore we have a scenario where the BH in the Milky Way describes the orbital motion of the molecular gas (Zhao et al. 2010), but not in NGC 6951. Seen in H_2, NGC 6951 has a different kinematic behaviour than that of the Milky Way, in the sense that the velocity dispersion is of the same order of the rotation velocity (of 40 km s^{-1}), a clear scenario where the turbulent motions play an important role in the nuclear dynamics.

Our ability to describe the origin of the H_2 disc in NGC 6951 is the same of trying to explain the origin of the several nuclear gas components in the Milky Way, which is very unclear. We remind that the molecular structure here is bigger, more massive and organized than the ring in the Milky Way. This amount of gas, with specific angular momentum, could be, in principle, the consequence of two processes: a misaligned minor merger or, eventually, a hypothetical bar. Minor mergers are generally inferred by counter-rotation of gas or stars and tidal-tails, which are not seen in our data. The hypothesis of a bar, which may have been dissolved by dynamical processes (Pérez et al. 2000), could lead to the formation of a rotating disc perpendicular to a inner bar major axis (Tohline & Durisen 1982). However, this bar should have formed in the same orientation of the galaxy ring (8°of difference from the galaxy disc) which still makes $\sim$40°with the molecular disc, so the drained gas would hardly be with such inclination, in the case the disc survives longer than the bar. In addition, we do not see any evidence of a bar in the stellar emission.

6.3 The molecular mass outflow rate

We can estimate the mass of the hot H_2 gas in the outflow, represented by regions 3 and 4 in Fig. 6, which in principle is the real amount of gas being ejected, without any fraction of cold gas. Following the calculations performed by Scoville et al. (1982) and Riffel et al. (2008):

$$M_{H_2} = \frac{2m_p F_{H_2\lambda 2.1218} 4\pi D^2}{f_{\nu=1,J=3} A_{S(1)} h\nu}$$
$$= 5.0776 \times 10^{13} \left(\frac{F_{H_2\lambda 2.1218}}{ergs^{-1}cm^{-2}}\right)\left(\frac{D}{Mpc}\right)^2$$

where m_p is the proton mass, $F_{H_2\lambda 2.1218}$ is the line flux (here not corrected from extinction and assumed it has a small effect - see 4), D is the galaxy distance and $f_{\nu=1,J=3}$ is the fraction of hot H_2 in the $\nu = 1$, $J = 3$ level, with M_{H_2} given in solar masses. The linear dependence of the H_2 emissivity on density is made under the assumption of a thermalized gas, at 2000 K and with $n_{H_2} > 10^{4.5}$ cm^{-3}. This implies a population fraction of 1.22×10^{-2} with a transition probability $A_{S(1)} = 3.47 \times 10^{-7}$ s^{-1}. Using Table. 1, for the NW outflow region, number 4, we have $F_{H_2\lambda 2.1218} = 4.24 \pm 0.12\times10^{-16} erg\ s^{-1}cm^{-2}$ within an aperture of $\sim 0''.2$, so we obtain that $M_{H_2} \sim 12M_\odot$. Performing the same calculation to region 3, we obtain again $M_{H_2} \sim 12M_\odot$, resulting in $\sim 24M_\odot$ of hot gas removed from the molecular disc. We can calculate the hot H_2 mass in the disc, corresponding to regions 1 and 2, which gives a total of $M_{H_2} \sim 37M_\odot$. Considering the ratio of the cold to the hot component to be constant between the 4 regions of the structure (which is about 10^{5-7} Dale et al. 2005), only 40% of the emitting gas is in the outflow.

On the other hand, one can estimate the mass outflow rate using the characteristic outflow speed as $V \sim \sqrt{v^2+\sigma^2}/\langle\sin\rangle$, with $\langle\sin\rangle = 0.7$, since we do not know the orientation for the outflowing H_2 (see Davies et al. 2014), which gives $V \sim 135$ km s^{-1}. Taking the average distance of 25 pc from the AGN and the total mass of the hot molecular gas of $24M_\odot$ for the outflow, we obtain the molecular mass outflow rate of $\sim 10^{-4} M_\odot\ yr^{-1}$. Giving the highly misalignment between the disc and the outflow, if we assume that all the outflowed gas is coming from the disc, and is not part of the ISM, we can set this value as the minimum inflow rate required to maintain the molecular structure, in terms of the hot H_2 mass. This fact leads to the interesting conclusion that if the mass inflow rate is smaller than this, the molecular disc, and thus the torus, will eventually disappear.

6.4 The molecular gas dynamics within the stellar ring

Most of the previous results come from the IRAM PdBI and the 30 m telescope observations of the faint CO(2-1) and HCN(1-0) emission in the central $0''.5$, which are part of the PdBI NU(clei of)GA(laxies) project (García-Burillo et al. (2003a); see also Haan et al. (2009); Krips et al. (2007); van der Laan et al. (2011)). Fig. 30 shows two adapted figures from van der Laan et al. (2011) (left panel) and Krips et al. (2007) (middle panel) for the CO and HCN molecular gas respectively, and in the right panel we show again the H_2 λ2.1218 image of the red and blue wings of the line profile to compare with the extended molecular emission. On the left they fitted a second Gaussian component to the CO(2-1)

emission in the flux map, besides that of the large-scale bar model, and found what they call a ″CO bridge″, interpreted as gas inflow within the disc, with a PA∼23°. This detection is the only hint, so far, of molecular gas inflowing inside the stellar ring, with a defined velocity. This CO component does not reach the centre, but is connected with the HCN emission with a similar velocity range of ±70 km s^{-1} and PA of 160°±20°(middle panel). This PA is significantly different from the major axis of the galaxy (PA= 135°). This non-alignment might be caused by a different inclination of the central gas disc, by non-circular velocities or even a warp, since the kinematics for the HCN and the CO bridge seems to behave as if they were in the disc.

The HCN flux map has a resolution ∼ 10 times inferior when compared to our data. It is also a compact structure with nearly the same extension of the H_2 emission, but with structure we detected unresolved in this case. Its kinematic axis has a PA closer to the radio emission than the H_2 disc, indicating a different distribution for the extended HCN gas. Krips et al. (2007) claimed that it could be the torus, which is not incompatible with our results, but we see with better resolution an edge-on H_2 disc with a superior limit for the scale height of about 10 pc.

There is too low emission outside the detected molecular structure, preventing a reliable link between the extended H_2 kinematics at the border of our FOV and the CO and HCN kinematics. However, it is clear that the kinematics of the warm H_2 disc is uncoupled from the mapped CO and HCN gas, inclined with respect the galaxy disc by ∼ 44°(considering $i_{H_2} = 90°$ and $i_{Gal} \sim 46°$). Even if the ring potential can drive gas to the centre, the H_2 emission reveals a different history on how this inflow takes place in the central 50 pc.

Since the H_2 disc has a very high inclination, assumed to be 90°, and a radial velocity curve typical of discs (Fig. 10), we can estimate a superior limit for the BH mass within the radius where the velocity curve has its peak. The dynamical effect of the velocity dispersion is not included on the calculus because the regions where we have an increase in dispersion are at a different position angle and we assumed the molecular gas in the disc, which is in thermal equilibrium, presents only local turbulence. Using the radius of ∼ 0″.15, which corresponds to ∼ 17 pc in the galaxy, and a velocity of 40 km s^{-1}, we obtain a dynamical mass of $8.7 \times 10^6 M_\odot$. This value is about 2 times the mass measured for the Milky Way (of ∼ $4.4 \times 10^6 M_\odot$ Genzel, Eisenhauer & Gillessen 2010), but still comprises the BH mass with a significant mass from the stars within this radius (the total mass of gas was found to be less than 3% of the stellar mass in the nuclei of a sample of 6 galaxies in Mazzalay et al. (2013). The mass estimated by Krips et al. (2007), in the central ∼ 0″.5 of HCN emission, was $2 \times 10^8 M_\odot$ for an inclination of 40°, which is about one order of magnitude above our result, for a radius ∼ 3× larger. We remember that the HCN kinematic position angle is very similar to the radio position angle, which accounts only for the kinematics of the outflow in our data. Even if the HCN is in a disc with similar inclination of the galaxy, it is possible that both circular motions and the outflow kinematics are superposed at their measured velocities. This would overestimate the BH mass.

As pointed out by Kormendy & Ho (2013), galaxies with pseudo-bulges do not follow the $\sigma - M_{BH}$ relationship, as is the case of NGC 6951 (Sec. 5.1). Pseudo-bulges have smaller BH mass at a given σ than galaxies with classical bulges. For this reason, despite the good measurement of the stellar velocity dispersion, we do not include it in the calculus of the BH mass.

Our interpretation of the velocity dispersion for the molecular gas, in the region of the shocks, is that it comes from the collision of the jet with the molecules in the disc. This is responsible to increase the gas turbulence and to decrease the rotation velocity, leading to a thicker disc, and to remove some of the angular momentum, favoring the accretion flow. This may affect the structure of the shocked material, eventually stopping the rotation pattern of the disc or even cause its ″evaporation″ if the inflow rate is not enough for the gas supply.

These misalignments between outflows and discs were found to be common, measured by the inclination of the NLR with respect the disc (Fischer et al. 2013). More than 50% of a sample of active galaxies were their kinematics well fitted by models in which the outflow intercepts the disc, implying that some gas there is also being removed, although this is not sufficient to impact the large scale properties of the host galaxies (Davies et al. 2014). This leads to the possibility that the infalling gas, in fact, has no correlation with the orientation of the galactic disc, since it could be the byproduct of feedbacks occurred in the past. Maybe some major event was necessary to pull out the angular momentum of the gas in the past, when viscous torques played an important role, and this favored small episodes of accretion nowadays. This hypothesis could be the consequence of the insufficient outflow velocity of the gas to escape from its host galaxy (Davies et al. 2014), falling back as a new material supply to feed the BH.

7 CONCLUSIONS

We have presented and analyzed the high resolution NIR data cube of NGC 6951 obtained with the NIFS spectrograph on the Gemini North Telescope. We also re-analyzed publicly available archives both from the HST (images) and Gemini North GMOS (data cubes) of the same galaxy. We focused on the central 200 pc of the galaxy. Our results are based both on the molecular an ionized gas phases and the main conclusions are the following:

- We detected a compact structure of molecular gas seen in H_2, interpreted as a nearly edge-on disc with diameter of ∼47 pc, PA=124°and velocity range from -40 to +40 km s^{-1}. This disc, probably the source of gas feeding the AGN, is misaligned with respect to the radio emission that has a PA=156°.

- The position angle of the radio jet is consistent with that of the ionization cones, with PA=153°±1°, seen in the Hα+[NII] HST image. The Hα+[NII] emission is also seen in the GMOS data cube; the brightest side is seen in blueshift, revealing that the ionized structures are seen in outflow.

- There are two regions of turbulent gas, seen both in molecular and ionized phases, that are connected to the

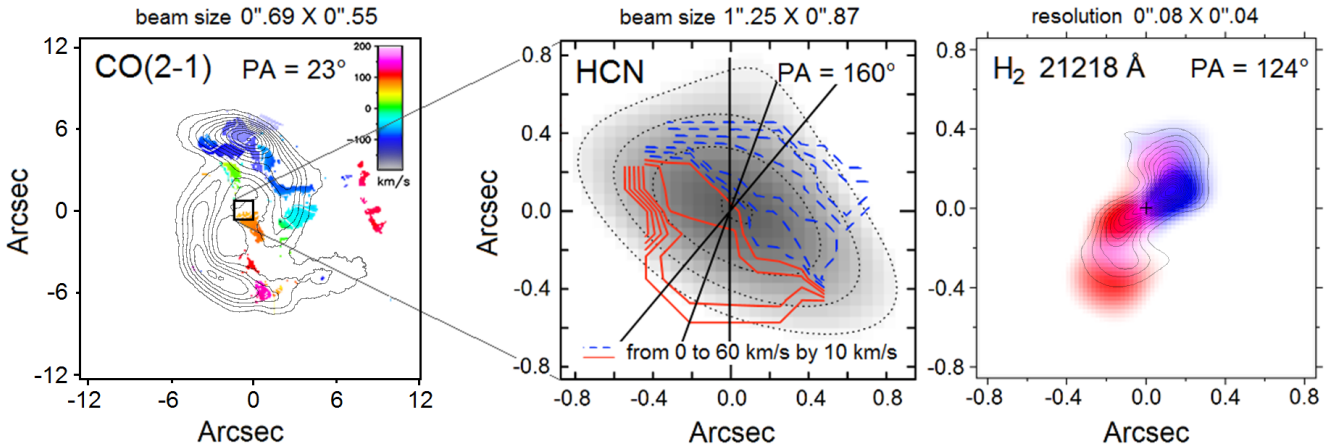

Figure 30. Left: velocity of the second Gaussian component fitted to the CO(2-1) line with the emission contours (van der Laan et al. 2011). The square in the centre shows the dimensions of our FOV. Middle: velocity map of HCN(1-0) (red and blue lines) overlaid to the integrated emission (gray scale) (Krips et al. 2007). Right: image of the $H_2\lambda 2.1218$ red and blue wings, with the contours of the average molecular emission; the velocity range is from -40 to +40 km s^{-1} in the disc.

edges of the molecular disc. These two turbulent spots have a PA similar to the radio jet and the ionization cones.

• The two turbulent spots coincides with high ratio of [NII]/Hα=5, suggesting that this region is excited by shocks.

• Our results, which show the correlation between the velocity dispersion of the [N II] with the [N II]/Hα line ratio, agree with the work of (Storchi-Bergmann et al. 2007), indicating that the [N II] excitation is related to its kinematics, although this correlation is well seen in the NW part of the cone.

• Based on the H_2 line ratios, we conclude the excitation mechanism is mainly due to shocks, which leads to an unpopulated first vibrational state, characterized by the cooling in the post-shock gas. We found a temperature of 1988±68 K for the molecular gas, excluding the transition to the fundamental state of the molecule.

• We explain the molecular structure as one rotating thick disc, connected to two turbulent regions, as a consequence of a //digging process// that the jet inflicts on the internal parts of the disc, ejecting some of the molecular gas. The molecules are exposed to the ionizing cones, with a calculated temperature of 6220 K, and probably they dissociate to form the ionized gas in the cones. As a consequence, the excavated molecular and ionized gas phases are both turbulent. This seems to be the most evident feedback activity in this object.

• The HST (V-I) image shows an irregular distribution of dust, not related to the molecular emission. This suggests that most of the gas may be too cold to be detected.

• The velocity curve along the molecular disc suggests that the mass within 17 pc is $M_{dyn}(< 17pc) = 8.7 \times 10^6 M_\odot$, giving an upper limit to the central BH mass.

• NGC 6951 has an active nucleus which can be classified as an intrinsic Seyfert 2, since we do not detected the presence of a BLR in the Brγ line or in Hα by PCA Tomography.

These findings were only possible because of the combined high resolution data and the accurate image processing techniques. Together, these observations set up a new consistent scenario for the inner 200 pc dynamics of NGC 6951. The molecular lines of H_2 are the best indicators of gas inflow so far, because it starts to emit at the region of the most relevant physical process inherent to the AGN, while the kinematics for the ionized gas is mostly described by the outflow feedback.

As NGC 6951 turned out to be a good case to study the shock morphology and physics, we intend to extend this analysis observing its nucleus in the J and H bands, which includes important forbidden Fe lines, known as a tracer of shocks in the ISM (Riffel et al. 2013; Mazzalay et al. 2013. Its location is also associated with partially ionized zones, which together with the molecular and high ionized gas distribution, can lead to useful constraints, as line ratios measured only in spatially resolved regions of interest.

With a broader wavelength interval, it will be possible to perform the stellar synthesis and estimate the stellar mass within the radius where the dynamical mass was calculated. This can give a new superior limit for the BH mass.

ACKNOWLEDGMENTS

This work is based on observations obtained at the Gemini Observatory, which is operated by the Association of Universities for Research in Astronomy, Ins., under a cooperative agreement with the NSF on behalf of the Gemini partnership: the National Science Foundation (United States), the Science and Technology Facilities Council (United Kingdom), the National Research Council (Canada), CONICYT (Chile), the Australian Research Council (Australia), Ministério da Ciência, Tecnologia e Inovação (Brazil) and CONICET (Argentina). This work is also based on observations with the NASA/ESA *Hubble Space Telescope* obtained at the Space Telescope Institute, which is operated by the As-

sociation of Universities for Research in Astronomy, Ins., under NASA contract NAS5-26555. We finally would like to thank FAPESP for support under grants 2011/19824-8 (DMN), 2008/06988-0 (TVR) and 2012/02268-8 (RBM).

REFERENCES

Abraham Z., Romero G. E., 1999, A&A, 344, 61
Antonucci R., 1993, ARA&A, 31, 473
Bardeen J. M., Petterson J. A., 1975, ApJ, 195, L65
Black J. H., van Dishoeck E. F., 1987, ApJ, 322, 412
Bower G. A., Wilson A. S., Mulchaey J. S., Miley G. K., Heckman T. M., Krolik J. H., 1993, in Bulletin of the American Astronomical Society, Vol. 25, American Astronomical Society Meeting Abstracts #182, p. 790
Brand P. W. J. L., Toner M. P., Geballe T. R., Webster A. S., 1989, MNRAS, 237, 1009
Bruzual G., Charlot S., 2003, MNRAS, 344, 1000
Cappellari M., Emsellem E., 2004, PASP, 116, 138
Carrara E. A., Abraham Z., Unwin S. C., Zensus J. A., 1993, A&A, 279, 83
Chen X.-Y., Hao C.-N., Wang J., 2008, Chinese J. Astron. Astrophys., 8, 25
Cid Fernandes R., Mateus A., Sodré L., Stasińska G., Gomes J. M., 2005, MNRAS, 358, 363
Costagliola F., Aalto S., Sakamoto K., Martín S., Beswick R., Muller S., Klöckner H.-R., 2013, A&A, 556, A66
Dale D. A., Sheth K., Helou G., Regan M. W., Hüttemeister S., 2005, AJ, 129, 2197
Davies R. I. et al., 2014, ArXiv e-prints
De Robertis M. M., Dufour R. J., Hunt R. W., 1987, JRASC, 81, 195
de Vaucouleurs G., de Vaucouleurs A., Corwin, Jr. H. G., Buta R. J., Paturel G., Fouqué P., 1991, Third Reference Catalogue of Bright Galaxies. Volume I: Explanations and references. Volume II: Data for galaxies between 0^h and 12^h. Volume III: Data for galaxies between 12^h and 24^h.
de Vaucouleurs G., Pence W. D., 1978, AJ, 83, 1163
Elitzur M., Shlosman I., 2006, ApJ, 648, L101
Erwin P., Pohlen M., Beckman J. E., Gutiérrez L., Aladro R., 2008, in Astronomical Society of the Pacific Conference Series, Vol. 390, Pathways Through an Eclectic Universe, Knapen J. H., Mahoney T. J., Vazdekis A., eds., p. 251
Ferrière K., 2012, A&A, 540, A50
Fischer T. C., Crenshaw D. M., Kraemer S. B., Schmitt H. R., 2013, ApJS, 209, 1
Fisher D. B., Drory N., 2008, AJ, 136, 773
García-Burillo S. et al., 2003a, in Astronomical Society of the Pacific Conference Series, Vol. 290, Active Galactic Nuclei: From Central Engine to Host Galaxy, Collin S., Combes F., Shlosman I., eds., p. 423
—, 2003b, A&A, 407, 485
García-Burillo S., Combes F., Schinnerer E., Boone F., Hunt L. K., 2005, A&A, 441, 1011
Genzel R., Eisenhauer F., Gillessen S., 2010, Reviews of Modern Physics, 82, 3121
Greene J. E., Ho L. C., Barth A. J., 2008, ApJ, 688, 159
Greenhill L. J. et al., 2003, ApJ, 590, 162
Gu Q., Huang J., 2002, ApJ, 579, 205
Guesten R., Genzel R., Wright M. C. H., Jaffe D. T., Stutzki J., Harris A. I., 1987, ApJ, 318, 124
Haan S., Schinnerer E., Emsellem E., García-Burillo S., Combes F., Mundell C. G., Rix H.-W., 2009, ApJ, 692, 1623
Halpern J. P., Steiner J. E., 1983, ApJ, 269, L37
Heckman T. M., 1980, A&A, 87, 152
Herrnstein J. R., Moran J. M., Greenhill L. J., Trotter A. S., 2005, ApJ, 629, 719
Hicks E. K. S., Davies R. I., Malkan M. A., Genzel R., Tacconi L. J., Müller Sánchez F., Sternberg A., 2009, ApJ, 696, 448
Ho L. C., 2008, ARA&A, 46, 475
Ho L. C., Filippenko A. V., Sargent W. L., 1995, ApJS, 98, 477
Ho L. C., Filippenko A. V., Sargent W. L. W., 1997, ApJS, 112, 315
Hollenbach D. J., Chernoff D. F., McKee C. F., 1989, in ESA Special Publication, Vol. 290, Infrared Spectroscopy in Astronomy, Böhm-Vitense E., ed., pp. 245–258
Jackson J. M., Heyer M. H., Paglione T. A. D., 1993, in Bulletin of the American Astronomical Society, Vol. 25, American Astronomical Society Meeting Abstracts, p. 116.07
Kormendy J., Bender R., Cornell M. E., 2011, Nature, 469, 374
Kormendy J., Ho L. C., 2013, ARA&A, 51, 511
Kormendy J., Kennicutt, Jr. R. C., 2004, ARA&A, 42, 603
Kotilainen J. K., Reunanen J., Laine S., Ryder S. D., 2001, A&A, 366, 439
Krajnović D., Cappellari M., de Zeeuw P. T., Copin Y., 2006, MNRAS, 366, 787
Krips M. et al., 2007, A&A, 468, L63
Kuno N., Nakai N., 1996, in Ground-Based Astronomy in Asia, Kaifu N., ed., p. 245
Kuo C. Y. et al., 2011, ApJ, 727, 20
Lawrence A., 2007, in IAU Symposium, Vol. 238, IAU Symposium, Karas V., Matt G., eds., pp. 117–122
Lawrence A., Elvis M., 2010, ArXiv e-prints
Lepp S., McCray R., 1983, ApJ, 269, 560
Maloney P. R., Hollenbach D. J., Tielens A. G. G. M., 1996, ApJ, 466, 561
Martin C. L., 2006, ApJ, 647, 222
Martini P., Pogge R. W., 1999, AJ, 118, 2646
Martini P., Regan M. W., Mulchaey J. S., Pogge R. W., 2003, ApJ, 589, 774
Matsushita S., Kohno K., Vila-Vilaro B., Tosaki T., Kawabe R., 1998, ApJ, 495, 267
Mazzalay X. et al., 2013, MNRAS, 428, 2389
McKinney J. C., Tchekhovskoy A., Blandford R. D., 2013, Science, 339, 49
Menezes R. B., Steiner J. E., Ricci T. V., 2013, ApJ, 762, L29
—, 2014, MNRAS, 438, 2597
Mezcua M., Prieto M. A., 2014, ApJ, 787, 62
Montero-Castaño M., Herrnstein R. M., Ho P. T. P., 2009, ApJ, 695, 1477
Mouri H., 1994, ApJ, 427, 777
Müller-Sánchez F., Prieto M. A., Mezcua M., Davies R. I., Malkan M. A., Elitzur M., 2013, ApJ, 763, L1
Pellegrini E. W. et al., 2013, ApJ, 779, L19
Pérez E., Márquez I., Marrero I., Durret F., González Del-

gado R. M., Masegosa J., Maza J., Moles M., 2000, A&A, 353, 893
Pringle J. E., 1992, MNRAS, 258, 811
—, 2003, in Astronomical Society of the Pacific Conference Series, Vol. 290, Active Galactic Nuclei: From Central Engine to Host Galaxy, Collin S., Combes F., Shlosman I., eds., p. 47
Ricci T. V., Steiner J. E., Menezes R. B., 2011, ApJ, 734, L10
—, 2014, MNRAS, 440, 2419
Riffel R., Rodríguez-Ardila A., Aleman I., Brotherton M. S., Pastoriza M. G., Bonatto C., Dors O. L., 2013, MNRAS, 430, 2002
Riffel R. A., Storchi-Bergmann T., Winge C., McGregor P. J., Beck T., Schmitt H., 2008, MNRAS, 385, 1129
Rodríguez-Ardila A., Pastoriza M. G., Viegas S., Sigut T. A. A., Pradhan A. K., 2004, A&A, 425, 457
Rodríguez-Ardila A., Riffel R., Pastoriza M. G., 2005, MNRAS, 364, 1041
Saikia D. J., Phookun B., Pedlar A., Kohno K., 2002, A&A, 383, 98
Scharwächter J., McGregor P. J., Dopita M. A., Beck T. L., 2013, MNRAS, 429, 2315
Schinnerer E., Scoville N. Z., 2002, in Astronomical Society of the Pacific Conference Series, Vol. 275, Disks of Galaxies: Kinematics, Dynamics and Peturbations, Athanassoula E., Bosma A., Mujica R., eds., pp. 379–382
Schnorr Müller A., Storchi-Bergmann T., Riffel R. A., Ferrari F., Steiner J. E., Axon D. J., Robinson A., 2011, MNRAS, 413, 149
Scoville N. Z., Hall D. N. B., Ridgway S. T., Kleinmann S. G., 1982, ApJ, 253, 136
Shaw R. A., Dufour R. J., 1995, PASP, 107, 896
Stauffer J., Schild R., Keel W., 1983, ApJ, 270, 465
Steiner J. E., Menezes R. B., Ricci T. V., Oliveira A. S., 2009, MNRAS, 395, 64
Sternberg A., Dalgarno A., 1989, ApJ, 338, 197
Storchi-Bergmann T., 2010, ArXiv e-prints
—, 2014, in IAU Symposium, Vol. 303, IAU Symposium, Sjouwerman L. O., Lang C. C., Ott J., eds., pp. 354–363
Storchi-Bergmann T., Dors, Jr. O. L., Riffel R. A., Fathi K., Axon D. J., Robinson A., Marconi A., Östlin G., 2007, ApJ, 670, 959
Tohline J. E., Durisen R. H., 1982, ApJ, 257, 94
Tully R. B., Fisher J. R., 1988, Catalog of Nearby Galaxies
Usero A., García-Burillo S., Fuente A., Martín-Pintado J., 2004, in Astronomical Society of the Pacific Conference Series, Vol. 320, The Neutral ISM in Starburst Galaxies, Aalto S., Huttemeister S., Pedlar A., eds., p. 273
van der Laan T. P. R. et al., 2011, A&A, 529, A45
van der Laan T. P. R., Schinnerer E., Emsellem E., Hunt L. K., McDermid R. M., Liu G., 2013, A&A, 551, A81
Wada K., Norman C. A., 2002, ApJ, 566, L21
Winge C., Riffel R. A., Storchi-Bergmann T., 2009, ApJS, 185, 186
Wolniewicz L., Simbotin I., Dalgarno A., 1998, ApJS, 115, 293
Yusef-Zadeh F., Stolovy S. R., Burton M., Wardle M., Ashley M. C. B., 2001, ApJ, 560, 749
Zhao J.-H., Blundell R., Moran J. M., Downes D., Schuster K. F., Marrone D. P., 2010, ApJ, 723, 1097
Zou S. F., Gong B. P., 2012, ArXiv e-prints